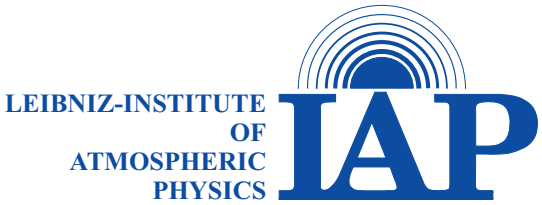

Resolving the horizontal structure of mesospheric echoes applying modern radar approaches

Kumulative Dissertation
zur
Erlangung des akademischen Grades
doctor rerum naturalium (Dr. rer. nat.)
der Mathematisch-Naturwissenschaftlichen Falkultät
der Universität Rostock

vorgelegt von
Svenja Lara Sommer
Rostock, 27. Mai 2016

urn:nbn:de:gbv:28-diss2017-0032-9

Betreuer:	Prof. Dr. Jorge L. Chau
	Leibniz-Institut für Atmosphärenphysik an der Universität Rostock
Gutachter:	Prof. Dr. Jorge L. Chau
	Leibniz-Institut für Atmosphärenphysik an der Universität Rostock
	Prof. Dr. Cesar La Hoz
	Universität Tromsø

eingereicht am:	27. Mai 2016
verteidigt am:	2. Dezember 2016

Abstract

Radar echoes from mesospheric altitudes have been observed at polar latitudes since the early 80's and are called, due to their occurrence, polar mesospheric summer echoes (PMSE). These echoes occur between 78 km to 90 km altitude and between May and August. At polar latitudes, the occurrence rate is $> 95\%$. The physical mechanism behind these echoes is mainly understood and involves the existence of charged ice particles, turbulence and free electrons. In this thesis, the structure of PMSE is investigated using the Middle Atmosphere Alomar Radar System (MAARSY). MAARSY allows multi beam, spaced antenna, narrow and wide beam as well as imaging experiments, which were used in this thesis. Observing PMSE on short time scales (2 ms) indicate random fluctuations. Such fluctuations are simulated in this thesis and their effects on measurement techniques and PMSE characteristics are discussed. The angular dependence of PMSE is investigated, taking the behavior of PMSE at short time scales into account. It was found that PMSE scattering is, in general, isotropic, while previous findings of an apparent high aspect sensitivity could be reproduced and explained by localized isotropic scattering. Furthermore, imaging is used to study the horizontal structure of PMSE on time scales of $\sim$30 s, revealing that PMSE appear to be patchy. The patch size varies between < 1 km and > 5 km. This observation is also discussed with regard to measurement techniques such as a spatial correlation analysis or Doppler beam swinging that assume a homogenously filled observation volume. In summary, this thesis shows a major improvement of the understanding of the angular dependence and horizontal structure of PMSE.

Zusammenfassung

Radarechos aus der Mesosphäre werden in polaren Breiten seit den frühen 80er Jahren beobachtet und werden aufgrund ihres Auftretens polare mesosphärische Sommerechos (PMSE) gennant. Diese Echoes kommen im Zeitraum von Mai bis August in einem Höhenbereich zwischen 78 km to 90 km vor. In polaren Breiten liegt die Auftrittshäufigkeit bei über 95%. Der zugrundeliegende physikalische Zusammenhang von diesen Echos ist größtenteils verstanden und beinhaltet geladende Eisteilchen, Turbulenz und

freie Elektronen. In dieser Arbeit wird die Struktur von PMSE mit Hilfe des Middle Atmosphere Alomar Radar System (MAARSY) untersucht. MAARSY erlaubt die Durchführung von Experimenten mit mehreren Radarstrahlen, räumlich getrennten Empfangsantennen, schmalen und breiten Radarstrahlen sowie bildgebenden Radarverfahren, die auch in dieser Arbeit eingesetzt wurden. Die Beobachtung von PMSE auf kurzen Zeitskalen (2 ms) deutet auf zufällige Fluktuationen hin, die in dieser Arbeit simuliert und deren Auswirkungen auf Messmethoden diskutiert werden. Die Winkelabhängigkeit von PMSE wird untersucht, wobei die Struktur von PMSE auf kurzen Zeitskalen berücksichtigt wird. Es wird gezeigt, dass PMSE als isotroper Rückstreuer betrachtet werden können, wobei die Ergebnisse vorhergehender Arbeiten, hindeutend auf eine scheinbar starke Winkelabhängigkeit, reproduziert werden können. Dies wird in dieser Arbeit mittels eines lokalisierten und isotropen Streuprozesses erklärt. Weiterhin werden bildgebende Radarverfahren eingesetzt, um die Struktur der PMSE auf Zeitskalen von $\sim$30 s zu untersuchen. Dabei treten PMSE ungleichförmig und in zusammenhängenden Gebieten auf. Die Gebietsgröße reicht von unter 1 km bis über 5 km. Die Auswirkungen dieser Unregelmäßigkeiten auf verschiedene Messmethoden, wie die räumliche Korrelationsanalyse oder das sogenannte Doppler beam swinging, bei denen von einem homogen gefüllten Beobachtungsvolumen ausgegangen wird, wird diskutiert. Zusammengefasst beschreibt diese Arbeit einen Fortschritt im Verständnis der Winkelabhängigkeit und horizontalen Struktur von PMSE.

Contents

List of Acronyms

ALWIN	Alomar wind radar
CRI	Coherent radar imaging
DBS	Doppler beam swinging
EISCAT	European Incoherent Scatter Scientific Association
FCA	Full correlation analysis
HPFW	Half power full width
HPLA	High power large aperture
IAP	Leibniz-Institute of Atmospheric Physics
NLC	Noctilucent clouds
MAARSY	Middle atmosphere Alomar radar system
MAOA	Mean angle of arrival
MSE	Mesospheric summer echoes
MST	Mesosphere Stratosphere Troposphere
PMSE	Polar mesospheric summer echoes
PMWE	Polar mesospheric winter echoes
PRF	Pulse repetition frequency
RTI	Range time intesity
SCA	Spatial correlation analysis
SNR	Signal to noise ratio
SOUSY	Sounding System for atmospheric structure and dynamics
UHF	Ultra high frequency
VAD	Velocity azimuth display
VHF	Very high frequency
VVP	Volume velocity processing

Chapter 1 Introduction

The (polar) mesosphere (50 km – 90 km) has come more and more into focus of scientific interest in the last couple of decades. The physical processes in this region of the atmosphere are not fully understood, although the mesosphere, which is coupled through the stratosphere to the troposphere, has an impact on tropospheric climate and hence, the weather (*Baldwin and Dunkerton*, 2001; *Matthias et al.*, 2012). Especially, measurements of atmospheric parameters from the mesosphere are rare, as it is quite hard to investigate the atmosphere above 50 km and below 90 km. These altitudes are difficult to observe with in situ techniques. It is too high to be reached with balloon borne instruments and too low for satellites. Rocket borne instruments are occasionally used, but are expensive and take only "snapshots" of the atmosphere. Ground based instruments such as lidar, optical imager or radar can be used to observe the mesosphere, but unlike radar, optical imager and lidar are limited by tropospheric clouds. Radar observations are therefore an excellent method to observe the mesosphere continuously.
The middle atmosphere is not only necessary to observe and understand because it is coupled to the layers above and below, but exhibits itself interesting dynamics, as gravity waves break, deposit momentum and create turbulence. Especially turbulence and wind estimations from the middle atmosphere are rare but crucial for climate models to reproduce the physical processes in the atmosphere. Additionally, the density of the atmosphere decreases exponentially with height, therefore trends should be easier to be observed in the mesosphere than in the troposphere.
The polar middle atmosphere shows several interesting features, for example, the mesopause region around ~ 85 km is the coldest region in the atmosphere. Unlike the troposphere, that it is warm in summer and cold in winter, the mesosphere is cold in summer and warm in winter. The temperatures in summer are extremely cold and can be as low as 130 K (e.g., *Witt et al.*, 1965; *Lübken et al.*, 1993; *Höffner and Lübken*, 2007) and deviate from the radiative equilibrium by more than 100 K. These cold temperatures are caused by breaking gravity waves, inducing a residual circulation from the summer to the winter pole and a resulting adiabatic cooling at the summer pole. These cold temperatures, below the frost point, lead to some phenomena at polar regions. Fig. 1.1 shows a sketch of the temperature profiles in summer and winter at polar latitudes (69°N) from the empirical MSIS (Mass-Spectrometer-Incoherent-Scatter) model (*Picone et al.*, 2002). In summer conditions, the temperature falls below the water vapor frostpoint.
The most prominent phenomenon is probably noctilucent clouds (NLC), the highest clouds in the atmosphere. These ice clouds at ~ 82 km altitude can be observed by the

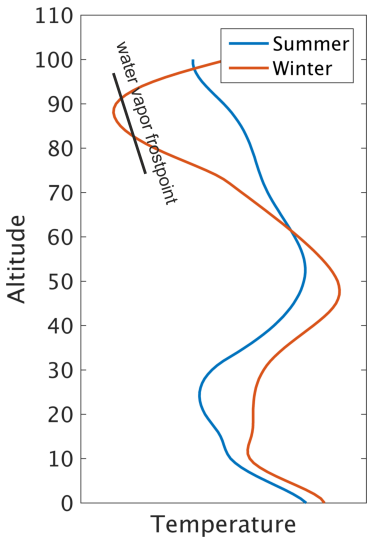

Figure 1.1 Sketch of temperature profiles of the atmosphere up to 100 km for summer and winter conditions derived from NRLMSISE-00. In summer, the polar mesosphere can reach temperatures below the water vapor frostpoint, indicated by a black line (after *Rapp and Lübken* (2004), Fig. 1, left panel).

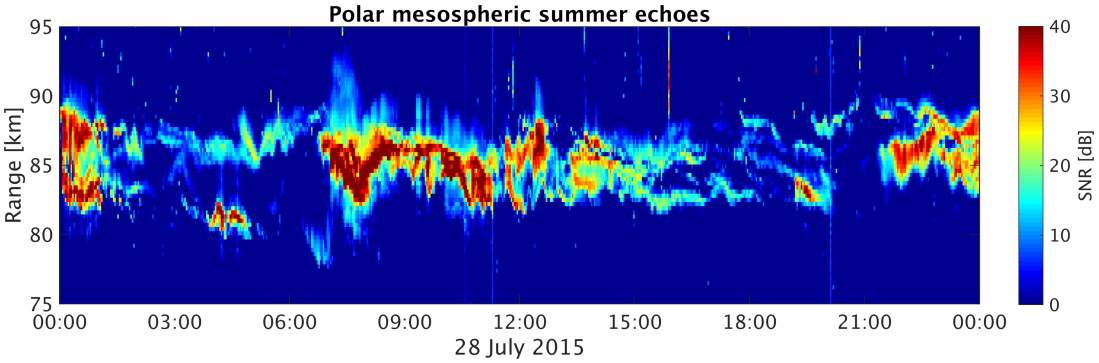

Figure 1.2 Range-time-intensity plot of PMSE. These echoes occur between 78 km to 90 km altitude during summer.

naked eye around Solstice. NLC are still illuminated by the setting sun when tropospheric clouds are already dark as the sun is already below the horizon. Such ice clouds are visible at mid latitudes but are also present at polar latitudes, although the sun does not set during the summer month, but the ice particles can be detected by lidars. Closely related to the optical phenomenon of NLC are polar mesospheric summer echoes (PMSE), which is radar scatter that can be observed from a few MHz up to a few hundred MHz. The PMSE occur, and hence the name, at polar latitudes during summer time in the mesosphere between 78 km to 90 km altitude. A range-time-intensity plot of PMSE occuring during 24 h is shown in Fig. 1.2. The microphysical processes leading to the occurrence of PMSE is closely related to the background conditions, as turbulence, ice particle and free electrons have to be present at the same time to observe

these echoes (*Rapp and Lübken*, 2004). PMSE provide information about the background condition of the atmosphere but can also be used as a tracer for wind and to derive dynamics, e.g., waves and turbulence.
As the general generating mechanisms for PMSE are understood, however, the small scale features of these echoes came into focus during the last couple of years. Such small scale structures might be generated by gravity waves or turbulence. To investigate the small scale features, the Middle Atmosphere Radar System (MAARSY) was build and become operational in 2011. MAARSY is one of the largest radar systems in polar regions for atmospheric research, with an observation volume of 5 km at 85 km. Standard measurement techniques, also applied at MAARSY, assume a homogenous filled beam volume. It is known from NLC observations, that small scale features exist at mesospheric altitudes (*Baumgarten and Fritts*, 2014), raising the question if features smaller than the beam volume can be observed by radar?
The resolution of a radar system can be improved by increasing the aperture but this solution is expensive. Another approach to increase the resolution of a radar system is imaging. Here, only sparse arrays are necessary to improve the resolution and the algorithms were first introduced in astrophysics but adapted to atmospheric radar in the early 1990's (*Kudeki and Sürücü*, 1991).
This thesis will analyze PMSE using imaging to investigate small scale structures in PMSE, as observed by radar. Therefore, an improved technique will be presented and the homogeneity assumption is reviewed. The implications on measurement techniques, especially of the angular dependency, of the found inhomogeneities will be discussed and concluded that PMSE are mostly caused by isotropic scattering. Additionally, maps of radial velocity and spectral width will be presented to show the improved radar resolution with imaging.
This thesis is structured as follows: the current understanding of PMSE with emphasis on the angular dependence and PMSE as a tracer for neutral dynamics is described in Ch. 2. The applied methods are briefly summarized in Ch. 3. The objective of this thesis is described in Ch. 4. The results are presented in Chs. 5 and 6. Ch. 5 summarizes the results regarding power fluctuations and apparent high velocities on short time scales. Ch. 6 deals with the horizontal structure of PMSE at different time scales, including an analysis of the angular dependence with different radar techniques and an estimate of the PMSE patch size. A summary of the thesis can be found in Ch. 7.

Chapter 2 Polar mesospheric summer echoes and their general characteristics

2.1 Current understanding of PMSE

Radar echoes have been used in atmospheric physics since the 1920's (see *Fukao and Hamazu*, 2014, Ch. 1.2, for a short summary), but it took another 50 years to discover backscatter from mesospheric altitudes. Coherent backscatter from mesospheric heights at polar latitudes were first reported by *Ecklund and Balsley* (1981). These echoes occur at polar latitudes, between 78 km to 90 km and only during summer time, hence the name polar mesospheric summer echoes (*Röttger et al.*, 1988; *Hoppe et al.*, 1988). The observation of these echoes were quite surprising, as only weak echoes from neutral turbulence (e.g. like the mesospheric echoes over Jicamarca (*Woodman and Guillén*, 1974)) or incoherent scatter was expected, but not the strong signal, which had to come from coherent scatter with changes in the radio reflective index at half the wavelength of the radar (3 m at 50 MHz). Over time, the properties of PMSE have been investigated to understand the physics behind the scatter. Since their discovery, PMSE have been analyzed regarding seasonal (*Balsley et al.*, 1983; *Hoffmann et al.*, 1999; *Bremer et al.*, 2003; *Latteck et al.*, 2007; *Latteck and Strelnikova*, 2015), diurnal (*Balsley et al.*, 1983; *Czechowsky et al.*, 1988; *Barabash et al.*, 1998; *Hoffmann et al.*, 1999; *Latteck et al.*, 2007), altitudinal variations (*Hoffmann et al.*, 2005; *Latteck and Bremer*, 2013) and interhemispheric differences (*Balsley et al.*, 1995; *Woodman et al.*, 1999; *Huaman and Balsley*, 1999; *Kirkwood et al.*, 2007; *Latteck et al.*, 2007; *Nilsson et al.*, 2008; *Latteck et al.*, 2008) as well as radar frequency dependence from MF to UHF (*Hoppe et al.*, 1988, 1990; *Bremer et al.*, 1996; *Karashtin et al.*, 1997; *Li and Rapp*, 2013).
This type of radar echo is not limited to polar latitudes but occurs also at mid-latitudes (*Czechowsky et al.*, 1979; *Reid et al.*, 1989; *Thomas et al.*, 1992), then called mesospheric summer echoes (MSE). The creating mechanism of MSE is the same as in PMSE (*Thomas and Astin*, 1994), although the occurrence rate of MSE is lower (*Latteck et al.*, 1999). The differences in the occurrence rate might be due to temperature and hence, fewer ice particles but also the presence of free electrons, as the sun sets, unlike as at polar latitudes, at mid-latitudes in summer (*Chilson et al.*, 1997; *Zecha et al.*, 2003).

The radar refractive index at mesospheric altitudes is mainly determined by the electron number density (*Woodman and Guillén*, 1974). The altitudes, where PMSE occur,

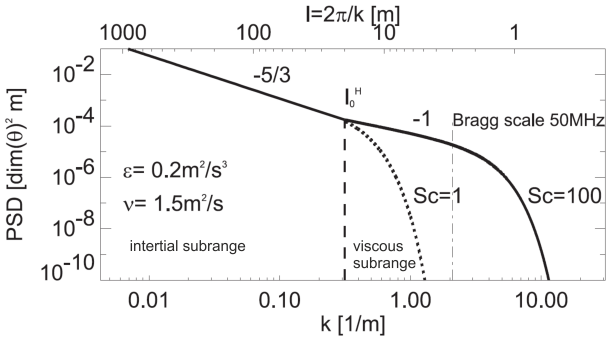

Figure 2.1 Power spectral density of neutral air turbulence as tracer θ in mesospheric altitudes. Figure taken and adapted from *Rapp and Lübken* (2004).

are part of the D-region of the ionosphere, so free electrons do exist at these altitudes. Still, the strong backscatter from PMSE cannot be explained by incoherent scatter and neutral turbulence, as the frequency spectra of PMSE and incoherent scatter are different (*Hoppe et al.*, 1988; *Röttger and LaHoz*, 1990). So, the longtime controversially discussed question was: what causes PMSE?
Several mechanism have been proposed, from non-turbulent theories with a steep electron density gradient (*Röttger et al.*, 1990) to scattering caused by turbulence (*Kelley et al.*, 1987; *Cho et al.*, 1992; *Rapp and Lübken*, 2004) (see also Sec. 2.2). The current understanding of the formation of PMSE includes turbulence, charged ice particles and hence very low temperatures and free electrons, and will be explained in the following paragraphs.

Earlier studies showed that neutral air turbulence can cause radar backscatter at the Bragg wave length. This was already noted in the early stages of investigation of PMSE (*Balsley et al.*, 1993). The turbulence is created by breaking gravity waves, which can, depending on the background conditions, reach mesospheric heights and break due to their growing amplitude as the pressure decreases (e.g., *Lindzen*, 1985).
The power spectrum of a tracer, shown in Fig. 2.1 in the middle atmosphere, e.g. neutral air turbulence, can be divided in two parts: the inertial subrange with a $k^{-5/3}$ wavenumber dependency and the viscous subrange with a k^{-7} dependency. In the first part, the dominating force is inertia, allowing fluctuation at these scales to sustain. The second part with the larger spectral power drop is dominated by molecular diffusion, destroying variations in the tracer (*Heisenberg*, 1948). Hence, no radar signal would be expected from the viscous subrange. The significant backscatter has to come at least from the minimum scale of the inertial subrange, called inner scale. Using the inner scale to calculate the turbulence strength necessary for significant PMSE backscatter at 3 m, just caused by neutral air turbulence, would cause extreme heating rates in mesospheric altitudes due to energy dissipation (*Lübken*, 1997). These heating rates have not been observed, hence, neutral air turbulence alone cannot be the cause for PMSE.

During the progression in understanding PMSE, the common observation of PMSE and NLC was noted (*Nussbaumer et al.*, 1996; *von Zahn and Bremer*, 1999; *Lübken et al.*, 2004). The presence of ice particles at mesopause altitudes alone is surprising, as very cold temperatures are necessary to form ice. The residual circulation, caused by momentum deposition of breaking gravity waves in the middle atmosphere at the summer and winter pole (e.g., *Holton and Alexander*, 2000), lead to an adiabatic heating at the winter pole and thus an adiabatic cooling at the summer pole. Temperatures around or even below 130 K can be reached (*Witt et al.*, 1965; *Lübken et al.*, 1990) and fall below the frost point of water vapor at these altitudes although the concentration is only a few part per million by volume (*Seele and Hartogh*, 1999). The nucleation process of these ice particles is still a current field of interest (*Rapp and Thomas*, 2006), but meteor smoke particles are the most probable nucleation source (*Hunten et al.*, 1980; *Plane*, 2000; *Strelnikova*, 2009; *Rapp et al.*, 2010; *Asmus et al.*, 2014). As ice particles are present in the D-region of the ionosphere, ice particles get charged (*Rapp and Lübken*, 2003).

The current explanation of the formation of PMSE is therefore as follows (*Rapp and Lübken*, 2004): The variations at the 3 m scale in the electron number density is caused by neutral air turbulence. As such, these wavenumbers are situated in the viscous subrange and would diffuse instantly due to the high viscosity. On the other hand, charged ice particles are present in the same volume as PMSE. These charged ice particles reduce the diffusivity of the free electrons due to ambipolar forces and longer lasting structures in the electron density can persist. Hence, small scale structures, induced by turbulence, can persist much longer than without ice particles. Summarized, free electrons, turbulence and charged ice particles are necessary for the formation of PMSE.
The Schmidt number $Sc = \frac{\nu}{D}$ can express that relationship between the kinematic viscosity ν and diffusivity D. Usually, $Sc \approx 1$ is assumed. By increasing the Schmidt number, fluctuations can persist at much smaller scales. The ice particles reduce the diffusivity of the free electrons, resulting in $Sc \gg 1$.
The influence of the free electrons and dust is discussed by *Varney et al.* (2011). Observing PMSE under different electron densities, they showed that the reflectivity of PMSE does not scale with electron density as suggested by *Rapp et al.* (2008), but dust densities and dust gradients and the relative densities of electrons and dust.

The microphysical processes leading to the formation of PMSE are generally understood and PMSE can also be used as a tracer for atmospheric conditions. In the literature, PMSE have been used to study long term temperature changes in mesospheric altitudes, although the results are controversial (*von Zahn*, 2003; *Thomas*, 2003). Energy dissipation rates measurement at mesospheric altitudes can contribute to understand the energy budget of the middle atmosphere (*Lübken et al.*, 1993). The derivation of energy dissipation rates with radar has several advantages: Radar can measure independent from tropospheric clouds, unlike Lidar, and continuously, unlike rocket borne measurements. Energy dissipation rates have been derived from PMSE observations, although several instrumental effects have to be considered (see Sec. 2.3.2 for further discussion). Solar precipitation is crucial for PMSE, as free electrons must

be present. At polar latitudes, the sun does not set during summer and hence, solar precipitation is always present. Trends can be found in PMSE depending on the strength of the solar A_p index or Lyman α (*Latteck and Bremer*, 2013).

2.2 Angular dependence

The dependence of returned power on the off-zenith angle is commonly called aspect sensitivity. Here, we refer to this effect as angular dependence, as aspect sensitivity implies a drop in power due to the scattering mechanism. The angular dependence increases when the received power decreases with increasing off-zenith angles. Isotropic scattering shows no drop in power, while a quasi-specular backscatter would only return power from the zenith or from tilted structures, if the incident beam is perpendicular to the reflective layer. Composites of both mechanisms would show also a drop in power, but not as large as for specular reflection. Hence, the angular dependence can be considered as an indicator for the scattering mechanism of PMSE (*Swarnalingam et al.*, 2011, and references therein).
Hocking et al. (1986) introduced the aspect sensitivity angle θ_s, which indicates the width of the polar backscatter diagram. Under the assumption, that the polar backscatter diagram can be described as a Gaussian function, small θ_s indicate a high angular dependence while large θ_s indicate a small angular dependence. The angular dependence of PMSE are investigated by several studies with different methods. The first method described here is the Doppler beam swinging (DBS) method (*Hocking et al.*, 1986, 1990). The angular dependence can be determined with two different beam pointing positions, again under the assumption, that the shape of the curve is predefined. Usually, a Gaussian shaped polar backscatter diagram is used. By comparing the returned power with a beam pointing off-vertical, the ratio is used to calculate angular dependence. The aspect sensitivity angle can be calculated by

$$\theta_s = \arcsin \sqrt{\frac{\sin^2 \theta_t}{\ln \left(P(0)/P(\theta_t) \right)} - \sin^2 \theta_0} \tag{2.1}$$

with $P(0)/P(\theta_t)$ as the ration of the returned power from the vertical beam and a beam pointing to an off-zenith angle θ_t and θ_0 represents the beam width (*Hocking et al.*, 1990). The aspect sensitivity angle θ_s can be derived with DBS under the assumption, that the scatter is homogeneous within the entire scan volume. *Czechowsky et al.* (1988) used DBS with the mobile SOUSY radar and reported θ_s values of 5°-6°. Following studies reported a range of values: 6.6° (*Hoppe et al.*, 1990), 10°-14° (*Huaman and Balsley*, 1998), 7°-10° (*Zecha et al.*, 2001), and 8°-15° (*Swarnalingam et al.*, 2011) at VHF. At UHF, *Nicolls et al.* (2007) reported no angular dependence of PMSE.
A disadvantage of the DBS technique is that each beam observes a different volume and localized changes in PMSE strength due to background conditions influence the measurement (*Chilson et al.*, 2002). Recently, *Latteck et al.* (2012) and *Stober et al.* (2013) showed that PMSE can vary in strength and appearance within a scanned volume and that temporal variations within minutes can occur.

To overcome the problem with the different observation volumes, other studies investigated the angular dependence with in-beam methods. Usually, the zenith beam is used in conjunction with spatially separated receivers. The spatial correlation analysis (SCA) or full correlation analysis (FCA) method take the spatial correlation between at least two antennas into account, where increased correlation values would indicate a more angular dependent backscatter. This method is limited as the beam width of the zenith beam determines the largest aspect sensitivity angle θ_s. Large θ_s can only be determined with a large uncertainty and, hence, the beam size limits θ_s estimations (*Smirnova et al.*, 2012). Following θ_s values, measured with FCA, have been reported: 3.5° (*Zecha et al.*, 2001) and 2°-3° by *Smirnova et al.* (2012).
Comparing the DBS and FCA method, the FCA method tends to result in smaller θ_s than the DBS method and hence, the scattering appears to be more angular dependent compared to the DBS results. This contradiction is noted in the literature (*Rapp and Lübken*, 2004) and is a still an ongoing topic of interest in PMSE research. The apparent large angular dependent nature of PMSE would suggest a rather specular reflection backscatter type, which is in contradiction to the common accepted theory of turbulence caused PMSE. In conjunction with turbulence, an isotropic backscatter would be expected, but have not been reported for PMSE at VHF before. Determining and understanding the angular dependency can help to understand the underlying backscatter type of PMSE.

2.3 Neutral dynamics from PMSE

Although PMSE themselves are a phenomenon worth exploring and understanding the microphysics, PMSE can also be used to derive dynamical parameters. This section describes shortly the main two dynamical parameters used in this thesis, wind and turbulence

2.3.1 Wind

An estimation of the wind in mesospheric regions by radar can be performed if a target scatters the radar signals. In mesospheric altitudes, clear air turbulence (*Ecklund et al.*, 1979), scatter from PMSE, polar mesospheric winter echoes (PMWE), changes in electron density or meteors can be used. Reviews of wind estimations in mesospheric altitudes can be found in *Balsley and Gage* (1980b) and *Rüster* (1994).
In the case of PMSE, two methods are usually used to derive the zonal, meridional and vertical wind components u, v and w: DBS and FCA (see also Ch. 3). Both methods have in common, that PMSE are assumed to be moved with the background wind. While DBS makes use of the Doppler shift from at least 3 different beam pointing directions, the FCA method analyzes the ground diffraction pattern of spatially separated antennas. Comparing results from both methods yields that FCA tends to underestimate the wind velocities compared to DBS (*Van Baelen et al.*, 1990; *Tsutsumi and Aso*, 2005).
The derived wind velocities can be analyzed to understand PMSE itself or find possible relationships between PMSE occurrence and strength to wave activity (e.g., *Czechowsky et al.*, 1989; *Röttger et al.*, 1990; *Barabash et al.*, 1998; *Chilson et al.*, 2000; *Yu et al.*,

2001; *Zecha et al.*, 2001). The derived winds can also be used to study the dynamics of the mesosphere region. By scanning the observation volume systematically and deriving the radial velocities for several beam pointing positions, the wind field can be resolved in space and time and, furthermore, the assumption of a homogenous wind velocity within the observation volume can be relaxed (*Browning and Wexler*, 1968; *Waldteufel and Corbin*, 1979). The deviation from the mean wind field u',v' and w' can be analyzed regarding wave activity at mesospheric altitudes.
A feature of MAARSY is fast beam steering which can be used to scan an observation volume of $\sim 100\,\mathrm{km}$ and to observe small changes in the background wind. *Stober et al.* (2013) found in a study of short scale monochromatic gravity waves, using PMSE as a tracer, gravity waves with horizontal wavelengths of $23\,\mathrm{km} < \lambda_h < 47\,\mathrm{km}$ and vertical wavelengths of $14\,\mathrm{km} < \lambda_z < 18\,\mathrm{km}$. Small scale waves with horizontal wavelength of 8 km to 20 km had already been observed with airglow imagers (*Hecht et al.*, 2007) and in numerical models (*Horinouchi et al.*, 2002), but airglow imagers do not resolve the vertical structure of waves in the mesosphere. The properties of these small scale waves, also called "ripples" have been studied very recently by *Stober et al.* (2016). The wind estimation using PMSE as a tracer is a good method to study not only large scale wave activity but also small scale waves and instabilities during summer time .

2.3.2 Turbulence

During the progress of understanding the formation of PMSE, the role of turbulence in this process was investigated. Neutral air turbulence is part of the formation process, hence, it was expected, that the backscatter become stronger if turbulence increases. Such correlation could not be found in PMSE observations (*Röttger and LaHoz*, 1990; *Hoppe and Fritts*, 1995) and was used as an argument against the turbulence-based theory. However, it was shown by *Rapp and Hoppe* (2006), that PMSE can even show an anti-correlation between signal strength and spectral width which can still be explained by turbulence-based PMSE. The signal strength does not depend only on turbulence, but also on charge number density $|Z_A|N_A$ (Z_A: dust charge, N_A: particle number density) and particle radius r_A. A proxy P was found by *Rapp et al.* (2003) as $P = |Z_A|N_A r_A^2$, which does not depend directly on the turbulence strength. An ongoing topic is whether turbulence strength has an impact on particle growth.
However, the turbulence strength can be seen as the random velocity fluctuations v_{rms} of the tracer, which can be used to derive the corresponding energy dissipation rates.
Turbulence strength and energy dissipation rates ϵ in the middle atmosphere are important, as turbulence transports constituents and heat and contributes to the thermal budget (*Lübken*, 1997). Hence, it is important for climate models to estimate the turbulence strength correctly, but measurements of the turbulence in mesospheric altitudes are rare. In situ measurements with rocket borne instruments have been performed, but can only measure snapshots as the sounding rocket flies through the mesosphere (*Lübken et al.*, 1993; *Lübken*, 1997; *Lübken et al.*, 2002; *Rapp et al.*, 2004; *Strelnikov et al.*, 2006).
Radars can contribute to energy dissipation rate measurements, as they are sensitive to turbulence (although only for a certain wavenumber) and can provide continuous

measurements independent on ground weather conditions. PMSE is an almost continuous tracer in mesospheric altitudes with occurrence frequencies $> 95\%$ with high power large aperture (HPLA) radar systems (*Latteck and Strelnikova*, 2015). To estimate the turbulence strength from the width of the spectrum of the radar signal ω_{turb}, several effects have to be considered as the beam is not infinitely small but illuminates a certain volume (*Hocking*, 1986). A review of turbulence estimations by radar is given by *Hocking* (1985). Usually, the beam broadening effect of the spectrum ω_{beam} due to the background wind is considered, as the tracer PMSE have a different Doppler shift in different parts of the beam volume, resulting in a broader spectrum than for turbulence alone. *Murphy et al.* (1994) and *Nastrom and Eaton* (1997) considered additional effects: shear broadening, ω_{shear} due to a vertical wind gradient and wave broadening, ω_{wave} due to short gravity waves. All these corrections have to be taken into account for deriving the energy dissipation rates:

$$\omega_{turb}^2 = \omega_{obs}^2 - \omega_{beam}^2 - \omega_{shear}^2 - \omega_{wave}^2. \tag{2.2}$$

Energy dissipation rate estimations by radar have been studied by several authors (*Hall et al.*, 2000; *Latteck et al.*, 2005), but only a few using PMSE as tracer (*Engler et al.*, 2005; *Li et al.*, 2010).
However, the authors of these studies estimate the corrections based on the main beam size of the radar, usually the half power full width (HPFW) beam size (3.6° for MAARSY, corresponding to a diameter of 5.4 km at 85 km). Side lobe suppression of HPLA radar systems is larger than for older systems (MAARSY: −17 dB, ALWIN: −13 dB), but PMSE backscatter power can reach over 35 dB, resulting in significant backscatter from side lobes. These side lobe contributions leads to an underestimation of the corrective terms introduced by *Hocking* (1985) and *Nastrom and Eaton* (1997). The derived energy dissipation rates by radar might therefore be overestimated.
In Ch. 6.3, we identify the side lobe contribution using a synthetic narrow beam and estimate the turbulence strength from such synthetic maps.

Chapter 3 Radar observation methods for PMSE

Range detection and ranging (radar) is based on pulsed electromagnetic waves with a wide frequency range, transmitted into the atmosphere. Electromagnetic waves can be scattered or reflected at changes of the electromagnetic refractive index. The traveled distance between radar and scatterer can be calculated by counting the time between pulse transmission and reception, as electromagnetic waves travel with the speed of light.
In atmospheric physics, first radar signals from the ionosphere had been found in 1925 (*Appleton and Barnett*, 1925). Following radar studies can be divided in mainly two parts: meteorological radar for precipitation detection at the GHz range and clear air radar at lower frequencies (*Fukao and Hamazu*, 2014). Nowadays, the term mesosphere-stratosphere-troposphere (MST) radars is common for systems at VHF frequencies due to their ability to detect echoes from the troposphere up to mesospheric heights and above.
The radar system MAARSY was built and optimized to study echoes from the MST. Free beam steering capabilities on a pulse-to-pulse basis, transceiver modules for each antenna and several receiving channels allows to investigate echoes from mesospheric altitudes with an unprecedented temporal and spatial resolution. This thesis focuses on PMSE detected by a MST radar, therefore the following part will describe radar scattering and measurement techniques that can be applied (but not limited) to MST radars and PMSE.

3.1 The Middle Atmosphere Alomar Radar System (MAARSY)

PMSE observations in this thesis were made with the Middle Atmosphere Alomar Radar System (MAARSY) on the island of Andøya in Northern Norway (69.30° N, 16.04° E), shown in Fig. 3.1. MAARSY is an active phased array antenna system at 53.5 MHz with 433 Yagi antennas, each with its own transceiver module. The peak power is 866 kW with 5% duty cycle. The HPFW beam size is 3.6° but can be influenced to phase and/or amplitude changes at each antenna, i.e. antenna compression techniques, similar to those applied by *Chau et al.* (2009). Additional to the beam broadening capabilities, the radar beam of MAARSY can be steered arbitrary by adding a linear

Figure 3.1 MAARSY is an active phased array with 433 antennas, located at Andenes, Norway, above the polar circle. Photo: Ralph Latteck.

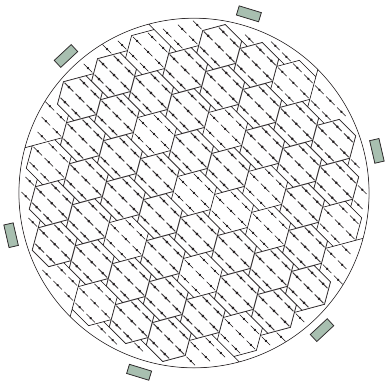

Figure 3.2 Positions of the smallest possible sub-arrays (sevens antennas), so called hexagons.

phase front while transmitting. That way, MAARSY is able to scan large areas in a short time without creating grating lobes up to $\theta > 30°$. Furthermore, the capability of 16 receiving channels allows to perform interferometry (*Schult et al.*, 2013) and imaging (*Sommer et al.*, 2013) as MAARSY can be divided in sub-arrays (Fig. 3.2). Further technical details can be found in *Latteck et al.* (2012). Combining the large area scans, wide and narrow beam and imaging/interferometric observations, MAARSY is a remarkable tool to investigate PMSE and to distinguish between instrumental and geophysical effects, e.g., for PMSE observations.

3.2 Scattering mechanisms for radar signals

Radar scattering in clear air is generally caused by changes in the radio refractive index $n = 7.76 \cdot 10^{-5} \frac{p}{T} + 0.373 \frac{e}{T^2}$ with the total pressure p, the partial pressure of water vapor e and the absolute temperature T (*Smith and Weintraub*, 1953). At PMSE altitudes, the atmosphere cannot be considered as neutral and free electrons are present, causing dispersion (*Balsley and Gage*, 1980a). Hence, the radio refractive index at these altitudes depends also on the refractive index of plasma:

$$n = 7.76 \cdot 10^{-5} \frac{p}{T} + 0.373 \frac{e}{T^2} - \frac{N_e}{N_c} \tag{3.1}$$

where N_e is the electron number density and N_c the critical electron number density. For typical mesospheric conditions in summer,

$$p = 0.05\,\mathrm{mbar} \quad (\textit{Taubenheim}, 1972), \tag{3.2}$$

$$\frac{e}{p} = 3\,\mathrm{ppmv} \quad (\textit{Grossmann et al.}, 1987), \tag{3.3}$$

$$T = 150\,\mathrm{K} \quad (\textit{Lübken et al.}, 1990), \tag{3.4}$$

$$N_e = 3000\,\mathrm{cm}^{-3} \quad (\textit{Taubenheim}, 1972), \tag{3.5}$$

$$N_c = 2\pi\frac{\epsilon_0 m_e}{e^2} f^2 \quad \text{with } \epsilon_0 \text{ as permittivity of free space,} \tag{3.6}$$

m_e electron mass, e electron charge and f as wave frequency,

the dominating term is the plasma term. Hence, radar backscatter at mesospheric heights is mainly caused by free electrons. Two types of scattering in these altitudes exist due to free electrons: incoherent scattering, caused by the motion of the free electrons itself (Thompson scattering) and coherent scattering at structured irregularities of the refractive index (Fresnel or Bragg scattering). Fresnel scattering is caused by layered changes in the electron density, while Bragg scattering, the most likely cause for PMSE, is caused by structures at half the wavelength of the radar system and constructive interference of the scattered signal occurs. Fresnel scattering is very aspect sensitive, while Bragg scattering is isotropic. See *Lübken* (2013) for more details on turbulent radar scattering.

3.3 Space-time ambiguity

Radars operate by emitting radio waves and measuring the time between transmission and reception of the radar pulse. The range information is thus gained from a time measurement and covers an altitude range depending on the beam size. Furthermore, the radar beam is not infinitely small, which would require a indefinitely large array, and hence, a certain area above the radar is illuminated. The received power is an integration of the whole beam volume. Additionally, radar is used to determine the Doppler velocity of the tracer, but radar measures only the radial velocity. As shown in Fig. 3.3, left, the radial velocity (red arrows, the length represents the magnitude) of a tracer with a continuous background wind (blue arrows) depend on the angles of arrival in one range gate. The received radial velocity information is, again, an integration of all the radial velocities. The different radial velocities widen the spectrum of the signal. If the antenna beam pattern is known, the background wind and spectral width due to turbulence can be derived from the spectrum. An exaggerated example with wind shear and two layers is shown in Fig. 3.3, right. Without resolving the space-time ambiguity, neither the different wind speeds nor the spectral width in both layers can be determined.

To solve the ambiguity of space and time, the angular dependence of scattered power, radial velocity and spectral width has to be eliminated. As small scale structures should be resolved, it is crucial to break up the space-time ambiguity. In this thesis, the space-

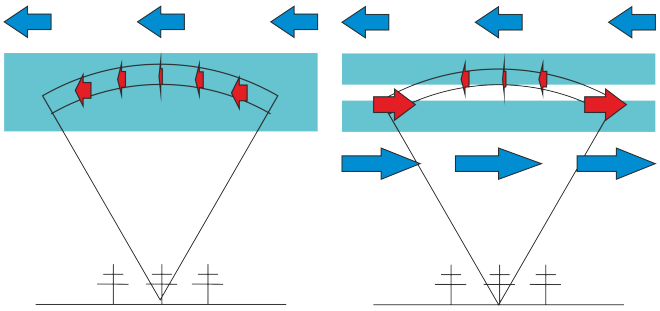

Figure 3.3 Left: Several radial velocities (red arrows) are received within a beam from a tracer on a continuous background wind (blue arrows). Right: Exaggerated example with two layers with different background winds covered by one range gate.

time ambiguity is resolved by using spatially separated receivers and applying imaging techniques.

3.4 Measurement techniques

Radar signals can be analyzed regarding power, or signal-to-noise ratio (SNR), and spectral shape. The spectral shape can be divided in two parts: the mean Doppler shift and the spectral width of the signal. Usually, MST radars are used to determine wind speed and direction as well as to estimate the energy dissipation rate from these signal properties. Different measurement techniques were developed to derive atmospheric parameters from radar signal.

Doppler beam swinging (DBS)

Doppler beam swinging is based on the property of radar measurements, that radars observe the radial velocity (see, e.g., *Fukao and Hamazu* (2014, Ch. 7.2.1) and for a brief historical overview *Van Zandt* (2000)). The spectrum of the time series $s(t)$ of a radar signal received from one range gate is analyzed and spectral parameters can be estimated by fitting a Gaussian function, assuming a Gaussian shaped beam and homogenous scattering. From the Gaussian function, the noise level N, signal strength S, the Doppler velocity v_r and spectral width σ can be derived. Radar beams pointing in different directions will receive different signals and therefore different radial velocities. The radial velocity v_r of a radar beam is determined by the meridional wind u, zonal wind v and vertical wind w. Vector decomposition along x-, y- and z-axis yields for a radar beam with zenith angle Θ and azimuth φ:

$$v_r = u \sin\Theta \cos\varphi + v \sin\Theta \sin\varphi + w \cos\Theta. \tag{3.7}$$

With at least 3 unique beam pointing directions, the wind vector can be determined under the assumption, that the wind field is homogeneous and does not change during the scan. More sophisticated approaches such as volume velocity processing (VVP) (*Waldteufel and Corbin*, 1979) or volume azimuth display (VAD) (*Browning and Wexler*, 1968) permit to access higher order kinetic properties in the wind field by introducing

also the first-order gradient terms, but require a larger amount of unique beam pointing directions:

$$u = u_0 + \frac{\partial u}{\partial x}x + \frac{\partial u}{\partial y}y \tag{3.8}$$

$$v = v_0 + \frac{\partial v}{\partial x}x + \frac{\partial v}{\partial y}y. \tag{3.9}$$

The difference between VAD and VVP is the way to solve for the wind field. VAD decomposes Eq. 3.7 into its Fourier components, while VVP fits the set of equations directly. As the beam is physically tilted, a larger amount of different directions require more time to scan the desired observation volume.
Additional to the wind estimation, DBS can be used to investigate the angular dependence of a scatterer. The angular dependence can be directly derived by comparing the backscattered power from beams pointing towards different zenith angles

$$\frac{S_i}{S_0} = \frac{(P_i - N_i)\,\gamma_i}{(P_0 - N_0)\,\gamma_0}, \tag{3.10}$$

where S_i is the signal, P_i the power, N_i the noise and γ_i the gain correction value from direction i. The subscript 0 represents the vertical direction.
This thesis presents an updated DBS method, taking changes in the scattering mechanism into account by integrating over long time periods and ranges. A further description of the improved DBS method for aspect sensitivity estimations can be found in *Sommer et al.* (2016b).

Spatial correlation analysis (SCA)

The problem of the comparison of different observation volumes, occurring with DBS, is not a problem of SCA, as it estimates the parameters within the beam volume. This is achieved by receiving the radar signal with spatially separated receivers. The SCA or FCA method (*Briggs*, 1968; *Doviak et al.*, 1996; *Holloway et al.*, 1997; *Holdsworth*, 1999; *Chau et al.*, 2000; *Hassenpflug et al.*, 2003) consider the correlation between two antennas and the autocorrelation of each receiver. The derivation of atmospheric parameters with a correlation analysis is done under the assumption that the scatter is statistically homogeneous distributed within the beam volume but can be relaxed to allow for vertical anisotropy (*Doviak et al.*, 1994) or additionally anisotropy in x- and y-direction (*Holloway et al.*, 1997).
The ground diffraction pattern of an antenna pair ij separated by Δx_{ij} (Δy_{ij}) in east-west (north-south) direction can be approximated by an ellipse. The parameters A, B and H described by *Holloway et al.* (1997, Eq. (30)) define the elliptical horizontal correlation function. The zero time-lag cross-correlation $|C_{ij}|$ between each antenna pair is

$$|C_{ij}| = \exp\left(-\frac{1}{4}\left(A\Delta x_{ij}^2 + B\Delta y_{ij}^2 + 2H\Delta x_{ij}\Delta y_{ij}\right)\right). \tag{3.11}$$

Using at least three different antennas, the three parameters A, B and H can be derived. Using a rotated, counterclockwise by Ψ, coordinate system, the pattern correlation

length ξ'_x and ξ'_y along the ellipse major and minor axis (x' and y') can be estimated. The antenna aperture contribution a_h can be written after *Doviak et al.* (1996) as

$$a_h = k_0\sqrt{2}\frac{\sigma_{\theta_T}\sigma_{\theta_R}}{\sqrt{\sigma_{\theta_T}+\sigma_{\theta_R}}}, \tag{3.12}$$

where σ_{θ_T} and σ_{θ_R} are Gaussian angular half beam widths of the transmitting and receiving beams, respectively, and k_0 is the radar wave number.
The aspect sensitivity angle Θ_s of an anisotropic scattering process can then be expressed as

$$\Theta'_x = \arcsin\left(\left(\sqrt{2}k_0\rho'_x\right)^{-1}\right) \tag{3.13}$$

$$\Theta'_y = \arcsin\left(\left(\sqrt{2}k_0\rho'_y\right)^{-1}\right). \tag{3.14}$$

Here, ρ'_x and ρ'_y denote the scatterer medium correlation length calculated from the diffraction pattern correlation length ξ'_x and ξ'_y. See *Sommer et al.* (2016b) for further description of the SCA method.

Mean angle of arrival (MAOA)

The angle of arrival of a radar signal is commonly used to derive the direction of the scatterer. Depending on the type of the scattering mechanism, reflective or isotropic, the angle of arrival is either the point of the reflection or a weighted (by the antenna gain) mean of all scatterers in the observation volume. Meteor radar systems use the angle of arrival to determine the specular reflection point of the plasma trail, generated by meteors entering the atmosphere. In the case of PMSE, the scattering type is probably more beam filling and, hence, a weighted mean of all scatter points in the beam volume. This theses refers therefore to the mean angle of arrival (MAOA) in conjunction with PMSE.
The MAOA in zenith angle α and azimuth angle β can be derived for a range gate with three spatially separated antennas. Based on the assumption, that the phase lines of scattered radio waves are parallel (the distance D between the scattering location and the radar is far larger than the antenna spacing d), the location of the scattering can be calculated by the phase received by the antennas. The MAOA can be found by solving the linear equation set (following *Lau et al.* (2006))

$$\underbrace{\begin{bmatrix}\varphi_{12}\\ \varphi_{13}\\ \varphi_{23}\\ \vdots\end{bmatrix}}_{\mathbf{p}} = -k_0 \underbrace{\begin{bmatrix}d_{x_{12}} & d_{y_{12}}\\ d_{x_{13}} & d_{y_{13}}\\ d_{x_{23}} & d_{y_{23}}\\ \vdots & \end{bmatrix}}_{\mathbf{D}} \cdot \underbrace{\begin{bmatrix}\sin(\alpha)\cos(\beta)\\ \sin(\alpha)\sin(\beta)\end{bmatrix}}_{\mathbf{r}}. \tag{3.15}$$

where α is the zenith angle and β the azimuthal angle of the scatterer, measured counter-clockwise from the x-axis. The phase differences are denoted by φ_{ij}, $d_{x_{ij}}$ and $d_{y_{ij}}$ denote the spacing in x- and y-direction between antennas i and j, respectively.

The radar wave number is $k_0 = \frac{2\pi}{\lambda}$ and λ is the radar wavelength.
Solving for the location vector $\mathbf{r}$, yields, using the least square method,

$$\mathbf{r} = \left(\mathbf{D}^\top \mathbf{D}\right)^{-1} \mathbf{D}^\top \mathbf{p}, \tag{3.16}$$

where $\mathbf{D}^\top$ denotes the transpose and $\mathbf{D}^{-1}$ the pseudoinverse of matrix $\mathbf{D}$. Eventually, it yields for α and β:

$$\alpha = \sin^{-1} \sqrt{(r_1^2 + r_2^2)} \tag{3.17}$$

$$\beta = \tan^{-1} \left(\frac{r_2}{r_1}\right). \tag{3.18}$$

The MAOA is determined by phase differences in the signals. Additionally to the phase differences due to the antenna positions, phases can alter by different wire length from the antenna to the acquisition or due to electronics. Although it should be the same for all antenna groups, minor differences due to imperfections in the constructions might lead to a phase set off. Hence, phase calibration is crucial for determining the MAOA. Results presented here for MAOA as well as imaging have been phase calibrated as described by *Chau et al.* (2014).
The measured phase differences φ_{ij} are ambiguous, as it cannot exceed 2π. Hence, it is possible that φ_{ij} was measured while the actual phase difference was $\varphi_{ij} + 2\pi n$, where n is an integer. It results for the MAOA method in ambiguity zones that depends on the baseline length between receivers i and j. The angular size α of the ambiguity zones can be calculated by

$$\alpha = \arcsin \frac{\lambda}{2d}. \tag{3.19}$$

Longer baselines result in a higher precision, while shorter baselines have larger unambiguous zones.

Coherent radar imaging (CRI)

Imaging in radar is used to map the received signal resolved in space. A rough image can be obtained by scanning the area above the radar by tilting the radar beam (*Latteck et al.*, 2012). *Stober et al.* (2013) used this rough kind of imaging to determine radial velocity maps. The resolution of this kind of imaging is limited to the beam size. To improve the resolution, in-beam estimation methods are necessary. With coherent radar imaging (CRI), the angular power, Doppler shift and spectral width distribution can be derived within the beam volume. It can be used to improve the radar resolution in both space, using several spatially separated antennas (*Palmer et al.*, 1998; *Yu et al.*, 2001; *Chilson et al.*, 2002; *Chen et al.*, 2004, 2008; *Sommer et al.*, 2013), and range, using different radar wavelengths (*Kudeki and Stitt*, 1987; *Palmer et al.*, 1999; *Chilson et al.*, 2000; *Yu and Palmer*, 2001; *Chen and Zecha*, 2009). The focus oo this thesis is the horizontal structure of PMSE and imaging was performed in space, using Capon's method (*Capon*, 1969; *Palmer et al.*, 1998) of imaging. Comparisons between radar images using Capon's method and Maximum Entropy for different parts of the spectrum, applied on PMSE data, showed that both methods yield similar results. However, Capon's method is, unlike Maximum Entropy, capable of yielding the

spectrum for a certain angle. Capon's method was found to be better than Fourier's method and faster than the Maximum Entropy (*Kudeki and Sürücü*, 1991; *Hysell and Chau*, 2006) method while yielding similar results for high SNR cases (*Yu et al.*, 2000).

Capon's method was developed for a phased array in general, but first used to detect seismic activity using the large aperture seismic array in Montana, USA. Later, it was adapted to astrophysics (e.g., *Ben-David and Leshem*, 2008) and also applied in atmospheric physics.

The angular power distribution, called brightness B, is calculated by weighting each receiver signal $s(t)$ with a linear filter $y(t) = \mathbf{w}^\dagger \mathbf{s}(t)$ to minimize possible interference by reducing side lobes. The weighting vector $\mathbf{w}(\mathbf{k})$ for a certain wavenumber vector $\mathbf{k} = [k_x\ k_y\ k_z]$ can be shown to be (*Palmer et al.*, 1998):

$$\mathbf{w}_C = \frac{\mathbf{V}^{-1}\mathbf{e}}{\mathbf{e}^\dagger \mathbf{V}^{-1}\mathbf{e}}. \tag{3.20}$$

The normalized cross-correlation matrix $\mathbf{V}$ with elements $V_{ij} = \frac{\langle S_i S_j^* \rangle}{\sqrt{\langle |S_i|^2 \rangle \langle |S_j|^2 \rangle}}$ for receivers i and j is defined as

$$\mathbf{V} = \begin{bmatrix} V_{11} & V_{12} & \dots & V_{1n} \\ V_{21} & V_{22} & \dots & V_{2n} \\ \vdots & & \vdots & \vdots \\ V_{n1} & V_{n2} & \dots & V_{nn} \end{bmatrix} \tag{3.21}$$

and

$$\mathbf{e} = \begin{bmatrix} e^{i\mathbf{k}\cdot\mathbf{D}_1} & e^{i\mathbf{k}\cdot\mathbf{D}_2} & \dots & e^{i\mathbf{k}\cdot\mathbf{D}_n} \end{bmatrix}, \tag{3.22}$$

where $\mathbf{D}_i$ represents the center of receiving array i.

The resulting brightness distribution is

$$B_C(\mathbf{k}, f) = \frac{1}{\mathbf{e}^\dagger \mathbf{V}^{-1}\mathbf{e}}. \tag{3.23}$$

The radial velocity and spectral width distributions can be derived, assuming quasi-stationarity during the observation period, by obtaining the spectrum for each desired $\mathbf{k}$. Hence, we apply the weighting vector, obtained with the average of the time series, on the time series signals $\mathbf{s}$ of the n receivers:

$$y(t) = \mathbf{w}_C^\dagger \mathbf{s}(t) \tag{3.24}$$

That way, CRI allows to scan a beam volume in software, reducing the time for a scan, necessary for, e.g., DBS wind measurements. If the beam volume illuminates a large area, the beam steering and parameter estimation can be performed in software and not by physically tilting the radar beam. That way, the number of beam pointing directions for the physical scan is reduced and, hence, the time necessary for a complete scan. Using the receiving configuration used in *Sommer et al. 2016b* and *Sommer and Chau, 2016*, the typical angular resolution is $\sim 1°$ HPFW.

Narrow and wide beam experiment

Determined by the antenna aperture, MST radars employ usually a certain beam size. A larger aperture leads to a more focused beam (*Fenn*, 2007) and instrumental effects, e.g., beam broadening in spectral width estimations, are reduced. On the other hand, the effect of the beam size can be estimated by employing different beam sizes while observing the same target. As PMSE can change quickly over time, the observation with different beam sizes has to be done in a very short time. As stated before, the beam size is determined by the antenna aperture. To widen the beam, the antenna aperture could be decreased which results in a less powerful beam, as less antennas transmit. Another possibility is to use different phasing for each antenna and widen the beam by interference (e.g. *Chau et al.*, 2009). That way, all antennas transmit and the power is retained, although spread over a larger area. For this thesis, a narrow and wide beam experiment was performed with MAARSY for the first time. Two beam sizes, 3.6° HPFW without phasing, and 12.6° with phasing[1], have been transmitted interleaved, changing the pulse size every 2 ms and allowing to observe the same PMSE with two different beam sizes.

[1] Phasing and beam size estimation courtesy of Toralf Renkwitz

Chapter 4 Open questions and objectives of this thesis

The microphysics of PMSE is well understood, although some open question still remain (*Rapp and Lübken*, 2004). For example, the simultaneous observation of mesospheric turbulence strength and aerosol particle size, the microphysics behind the origin of the ice particles or active heater experiments are still under investigation. Among the open questions, the question of the small scale structure of PMSE is still unanswered, and *Rapp and Lübken* (2004) suggested sounding rocket observations with several "daughter" payloads. Such a payload is currently being developed at IAP, called Turb3D (*Strelnikov et al.*, 2015). By ejecting several small payloads from a rocket, the structure of turbulence and aerosols will be investigated in situ.

Small scale structures are currently not only under investigation in PMSE but also in NLC. With Lidar, the structure of NLC are analyzed as they move trough the Lidar beam and change altitude due to small scale gravity waves (*Kaifler et al.*, 2013; *Ridder*, 2014). Additionally, the structure of NLC are observed with high resolution cameras. From these images, gravity waves with wavelength smaller than 10 km are observed (*Baumgarten and Fritts*, 2014).
As PMSE and NLC are closely related, small scale structures should also be present in PMSE. It has been shown that PMSE are not uniform on large scales (observation volume $> 50\,\mathrm{km}$ (*Latteck et al.*, 2012; *Stober et al.*, 2013)), but observations for small scale fluctuation are rare. *Röttger and LaHoz* (1990) concluded, from spectrum measurements using the EISCAT VHF radar, that PMSE consist of patches smaller than their observation volume ($\sim 1\,\mathrm{km} \times 2\,\mathrm{km}$). *Nicolls et al.* (2007) found PMSE patches with sizes of few kilometers at UHF.
Direct small scale measurement of PMSE at VHF have not been reported yet. Measuring the patch size of PMSE will help to investigate both geophysics, i.e., short gravity waves, turbulence distribution or aspect sensitivity, and methodological effects on the measurement, i.e., beam filling effect or the assumption of statistical homogeneity.
Additionally, the aspect sensitivity of PMSE is still under investigation. As mentioned in *Rapp and Lübken* (2004), the measured aspect sensitivity, at least in the lower part of PMSE, is too large to be explained with current theory (*Swarnalingam et al.*, 2011; *Smirnova et al.*, 2012). Furthermore, different measurement techniques leads to different degrees of aspect sensitivity. While in-beam estimation methods (SCA, FCA) yield very high aspect sensitive scattering, DBS results have reported lower, but still aspect sensitive, values. This contradiction between theory and measurement has not been resolved yet. Wind estimates derived from FCA, DBS and meteor observation do

also not agree. FCA tends to underestimate the wind velocity compared to the DBS or meteor wind estimations (*Tsutsumi and Aso*, 2005). This indicates also, that the assumptions of at least one of the measurement techniques is not fulfilled.

In this thesis, the structure of PMSE, observed by radar, will be investigated with radar imaging. Using the high flexibility of MAARSY, the scattering mechanism at a millisecond scale, as observed by radar will be explained and simulated and the aspect sensitivity of PMSE measured with different radar techniques. The DBS method will be improved to overcome the problem of different observation volumes. Measurement techniques such as FCA can only be applied correctly, if the assumptions made in the derivations of these techniques, are fulfilled. This thesis will investigate PMSE also regarding the applicability of wind measurement techniques. Furthermore, in-beam estimation techniques for Doppler velocity and spectral width will be implemented to show a way how radar systems can be improved to measure spectral parameters.

Chapter 5 PMSE on very short time scales

Summary of:

Sommer et al. (2016a): *On high time-range resolution observations of PMSE: statistical characteristics*

Understanding the radar scattering mechanism on a statistical basis, that can be provided by highly temporal resolved PMSE, will help to distinguish between instrumental effects like beam size, PRF or range resolution, and geophysical effects, such as ambient wind, aspect sensitivity or turbulence. As long as the effects are not carefully separated, the derived geophysical parameters are compromised by instrumental effects.
Sommer et al. (2016a) studied PMSE with an effective sampling period of 2 ms. A RTI of such a highly resolved data set of a 32 s observation period is shown in Fig. 5.1. Surprisingly, the returned SNR shows a strong fluctuation in time for each range gate. The received SNR varies between values at the noise level and strong SNR values of over 25 dB in periods below 2 s. These fluctuations are in the frequency range of infrasonic waves. These fluctuations have not been reported before, as previously used longer integration periods averaged these fluctuations. Previous studies with high temporal resolution (*Rüster*, 1997; *Lee et al.*, 2014) did not investigate the SNR but only derived parameters, although these fluctuations should also be visible in these data sets. Furthermore, a spatial correlation, evolving over time, can be seen in the data set by analyzing the MAOA with interferometry (Fig. 5.2). Tracking these motions, the MAOA show velocities $> 500\,\mathrm{m\,s^{-1}}$ and hence, apparently supersonic velocities.
We interpreted the fluctuations not as an actual oscillation in time but as correlation time of the scattering mechanism. The spectral width is the Fourier inverse of the correlation time, which is the width of the auto correlation function.
We used this interpretation also to simulate backscattering of PMSE. The occurrence of the fluctuations are relatively random but modulated by the coherence time. Therefore, our simulation is based on a spatial model of a random density fluctuation field modulated with a Gaussian function. In our observations, we have correlation not only in time, but also in range. According to those observations, the density fluctuation field in space $\mathbf{k} = [k_x,\ k_y,\ k_z]$ and frequency ω can then be written as

$$F(\mathbf{k}, \omega) \propto \exp\left(-\frac{1}{2}\left(\frac{(\omega - uk_x)^2}{\sigma_\omega^2} + \frac{k_z^2}{\sigma_\zeta^2}\right)\right), \tag{5.1}$$

with geophysical parameter u and σ_ω as wind speed and spectral width, S and N as signal and noise, and σ_ζ as range correlation, respectively. The radar does not

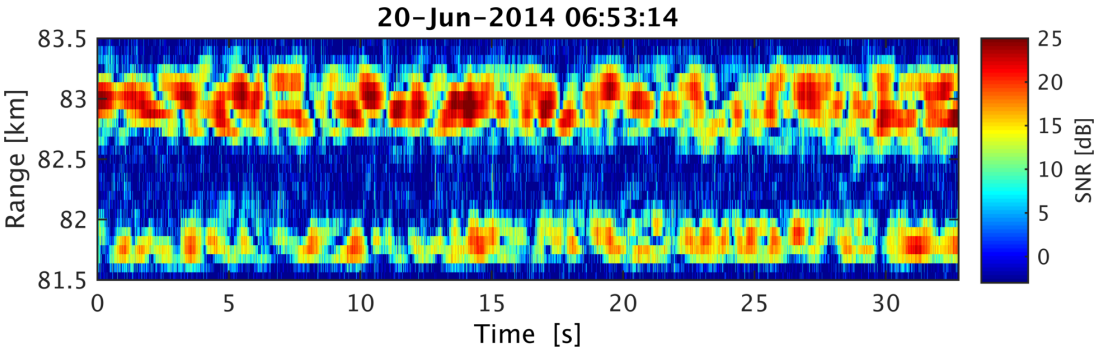

Figure 5.1 RTI of two layers of PMSE with a high temporal resolution of 2 ms and a range resolution of 75 m. The power appears to be fluctuating in the order of 2 s. Figure taken from *Sommer et al.* (2016a), Fig. 1.

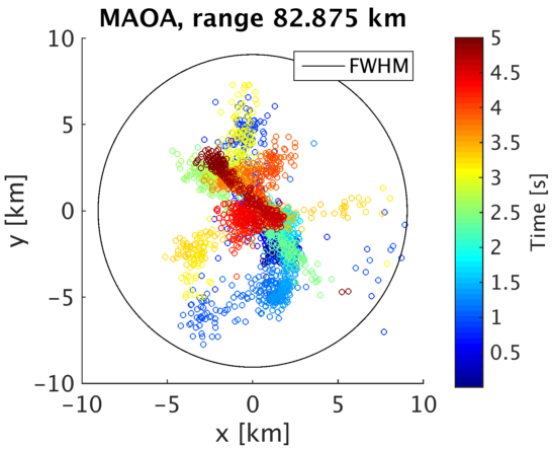

Figure 5.2 Track of the MAOA of one range gate of the first 5 s of range 82.875 km of the data set presented in Fig. 5.1. The location for each point in time is indicated by a dot, while the color indicates the temporal progression. The black line indicates the 3 dB beam width. The MAOA appears to be coming from larger angles than the beam width and show a correlation in time. Figure taken form *Sommer et al.* (2016a), Fig. 2, right.

observe the whole PMSE volume but illuminates only a certain area. Hence, the density fluctuation field F has to be multiplied by the antenna gain G, which we assume to be Gaussian shaped. The resulting simulated brigthness B, obsereved by the radar, is

$$B \propto \exp\left(-\frac{1}{2}\left(\frac{\lambda^2}{4\pi^2}\left(\frac{k_x^2+k_y^2}{\sigma_\theta^2}\right)+\frac{(\omega-uk_x)^2}{\sigma_\omega^2}+\frac{k_z^2}{\sigma_\zeta^2}\right)\right), \tag{5.2}$$

adding a correlation in space due to the antenna beam width σ_θ as an instrumental effect.
We adapted the parameters to represent the observations and compared them to an experiment, where the same PMSE was observed with a narrow (3.6° HPFW) and wide (12.6° HPFW) beam.

Based on the simulations, we concluded that apparent oscillations in power are caused by the correlation time of the scattering process and not by infrasonic waves. The correlation in space is dominated by the antenna beam pattern and the motion of the MAOA is only an apparent motion. This fact and the underlying assumption of randomly fluctuating density fields let us conclude, that the underlying physical process is influenced by turbulence, which is in agreement with the current understanding of PMSE (*Rapp and Lübken*, 2004). Furthermore, as the correlation in space is dominated by the antenna beam pattern, the underlying scattering process is horizontally isotropic.
We also like to stress that the random fluctuation have implications on wind measurements if short integration periods are chosen. If the integration time for wind estimation with FCA is below $\sim 16\,\mathrm{s}$, the apparent motion of the MAOA is dominant, resulting in high apparent wind speeds. This should be considered in future observations of wind using PMSE as a tracer.
Our simulation can be used in the future to derive geophysical parameter, such as turbulence, without the contamination of instrumental effects such as beam broadening in conjunction with a nested beam experiment. Here, the PMSE observations should be fitted to the 4D model to derive the geophysical parameters.

Chapter 6 Horizontal structures of PMSE and their influence on measurements

Summary of:

Sommer et al. (2014b): *Geometric considerations of polar mesospheric summer echoes in tilted beams using coherent radar imaging*

Sommer et al. (2016b): *On the angular dependence and scattering model of polar mesospheric summer echoes at VHF*

Sommer and Chau (2016): *Patches of polar mesospheric summer echoes characterized from radar imaging observations with MAARSY*, unpublished manuscript

This chapter summarizes the three papers mentioned above with regard to the angular dependency of PMSE, taking the beam filling effect into account and investigating the small scale structure of PMSE with imaging. Finally, wind and spectral width maps, derived with imaging, are presented.

6.1 Beam filling effect and angular dependency

The DBS method is used to derive the 3D wind out of the Doppler shift from at least 3 different beam pointing positions under the assumption, that the wind speed is constant within the observed volume. More sophisticated approaches such as VVP relax that assumption, but require several different beam pointing directions (see also Sec. 3.4). All methods have in common, that they assume that the nominal beam pointing direction is the same as the actual beam pointing direction.
Sommer et al. (2014b) studied the deviation from the nominal beam pointing directions in tilted beams. We found that the sharp gradient of SNR at the upper and lower boundary of PMSE affects the actual beam pointing direction. Applying CRI, we showed that a systematic deviation $\Delta\alpha = \alpha - \theta$ of the mean beam pointing α direction from the nominal beam pointing direction θ occur. Moreover, the magnitude of the deviations become larger with increasing off-zenith angle, and does not depend on the azimuth angle. The deviations at the lower boundary of PMSE were shifted towards zenith, while the deviations at the top of PMSE were shifted away from zenith (*Sommer et al.*, 2014b, Figs. 5 and 6). This feature starts to become visible at off-zenith

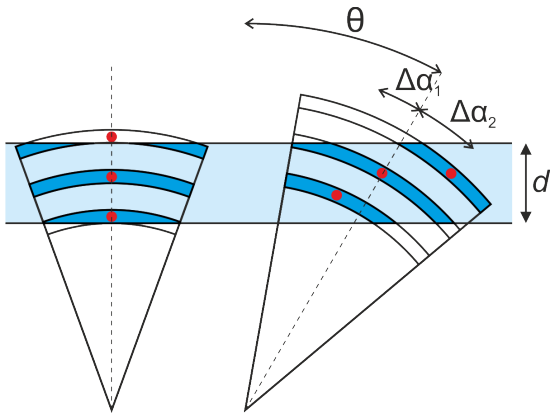

Figure 6.1 Sketch of the deviation from the nominal beam pointing direction at the upper and lower boundary. The left illustration shows the vertical beam, the right a tilted beam where systematic deviations occur. At the upper edge, the deviation (red dot) is towards larger off-zenith angles and towards smaller off-zenith angles at the lower boundary. d is the width of the layer, θ the nominal beam pointing angle and $\Delta\alpha_i$ the deviation of the MAOA for range gate i.

angles of 5° and larger. We interpreted the result as follows: due to the strong decrease in backscatter at the upper and lower boundary, the beam volume is not completely or homogeneously filled. This effect is sketched in Fig. 6.1, where the effect of the partially filled beam volume of a tilted beam is illustrated. The blue layer demonstrate the horizontally layered PMSE with sharp gradients in SNR at the upper and lower boundary. The red dots show the actual beam pointing direction. Here, the width of the layer d, the nominal beam pointing direction θ and the deviation $\Delta\alpha$ is also shown.

The deviation of the nominal beam pointing direction has implications on measurements with tilted beams such as wind estimations with DBS or VVP. The effective beam pointing position can be estimated by using the MAOA or estimating the deviation with CRI. The effective beam pointing position estimation is already implemented in wind estimation algorithms developed at IAP (*Stober et al.*, 2016). Such estimations should be implemented routinely in future developments, as it is relatively simple to estimate the MAOA, when at least 3 spatially separated receivers are available.

The incomplete filling of the beam volume does not only have implications on wind estimations, but also in scattered power estimation. Comparing the returned power from an isotropic scattering mechanism of a beam, which is completely filled by isotropic scattering, with a beam that is only partially filled, due to tilting, result in a decreased received power from the oblique beam. This effect was modeled for different off-zenith angles by *Sommer et al.* (2016b), where different widths for the PMSE layer were considered. The power drop due to the geometry of the measurement varies depending on the size of the layer. This implies, that the thickness of the layer has an impact on measured reduced power.

As pointed out in *Sommer et al.* (2014b) and calculated in *Sommer et al.* (2016b), the drop in power due to the layered phenomenon of PMSE has to be considered as it can reach up to −8 dB for thin PMSE. Therefore, we reviewed the angular dependency of

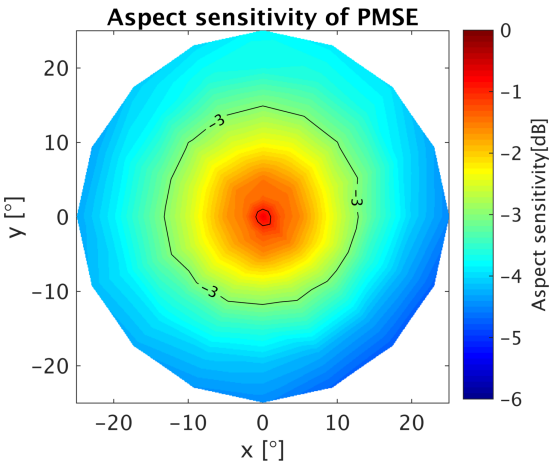

Figure 6.2 Aspect sensitivity map of PMSE with off-zenith angles up to 25°. The received power is nominated to the zenith and the drop in power from 80 unique off-zenith angles is color coded. The azimuthal mean drop at 25° is −3.5°, indicating isotropic scattering. Figure similar to Fig. 4, right, from *Sommer et al.* (2016b).

PMSE with an enhanced DBS analysis. Instead of comparing the returned backscatter directly, we separated the PMSE in core and edge region due to the beam filling effect. Still, the problem with different observation volumes remain (*Chilson et al.*, 2002). Assuming that the mechanisms responsible for the formation are not dominated by spatial influences, the occurrence frequency of PMSE should be the same for the different observation volumes. We suggested to integrate the power over a long period of time (> 10 s) to compensate for short time scale differences in PMSE strength due to geophysical influences. Thus, *Sommer et al.* (2016b) calculated the angular dependency separated into core or edge region due to the beam filling effect. Furthermore, due to the high flexibility of MAARSY, no assumptions regarding the shape of the polar backscatter diagram was necessary, as several different off-zenith angles have been considered. The resulting aspect sensitivity map is shown in Fig. 6.2. The nominated drop in power is symmetrical around zenith and shows a mean drop in power at 25° of −3.5 dB. The small drop in power might be due to an insufficient separation between core and edge region but is significantly smaller than values reported before and in the range of the modeled drop in power (see *Sommer et al.* (2016b), Fig. 6).
We found almost no decrease in power with increasing off-zenith angle, indicating isotropic scattering. The values correspond to $\theta_s > 30°$, but the usage of θ_s is not meaningful here, as it is definded for a Gaussian shaped polar backscatter diagram. However, for comparison purposes to previous studies, θ_s was estimated. Such large values of $\theta_s > 30°$ have not been reported in the literature before. On the other hand, previous studies did not consider the effects described in *Sommer et al.* (2016b). Furthermore, isotropic scattering of PMSE is in accordance with the current accepted theory of non-stratified turbulence. Further discussion can be found in *Sommer et al.* (2016b).

6.2 Horizontal structure at small scales

Sommer et al. (2016b) also investigated the angular dependency of PMSE with SCA. Contrary to the DBS method described above, this method uses only a vertical beam and makes use of spatially separated receivers. The aspect sensitivity angles θ_s can be derived under the assumption, that the scatter fills the beam volume homogeneously on a statistical basis, based on the cross-correlation of the receivers. Enhanced correlation is usually interpreted as strong angular dependency. Previous studies derived θ_s using SCA or FCA, deriving extremely low values for θ_s, i.e., suggesting a strong angular dependence (large aspect sensitivity). We applied SCA on the same data set as the DBS method described above, but on a 32 s basis instead of averaging over one day or month. This study confirmed extremely low values, with a median of 5.6°. This is in contradiction to the findings described in Sec. 6.1, where large values of θ_s have been found and pointed towards isotropic scattering. The small values of θ_s found with SCA would suggest that weak or no backscatter of PMSE at large off-zenith angles would be expected. But as already shown by *Latteck et al.* (2012) and *Stober et al.* (2013), significant backscatter of PMSE can be received from large off-zenith angles. Additionally to the short integration time of 32 s, we used also long integration times of 10 min. Comparing the short and long integration time results, the correlation values for the 10 min data set is significantly decreased, resulting in larger values for θ_s. The median value was found to be $\theta_s = 8.5°$ which was interpreted in the literature as less angular depending scattering.

This contradiction between low (or no) angular dependency observed with DBS and very strong angular dependency measured with SCA, is already described in the literature. Increased correlation values not only can be explained by strong angular dependency but also by a partially filled beam volume. Putting the results from DBS and SCA together, we concluded, that the increased correlation values indicate a non-beam volume filling scattering process. On short time scales, the beam volume is not homogeneously filled with isotropic scattering, resulting in an increased correlation. Applying longer integration periods, the scatter mechanism is statistically more homogeneous, as patches of PMSE drift through the beam volume. Hence, the correlation values decrease, resulting in larger values of θ_s even with SCA, indicating a more isotropic scattering. From the observations of PMSE with DBS and SCA, PMSE might consist of isotropic scattering but do not fill the beam volume homogenously on time scales of ~ 30 s.

These small patches of PMSE were investigated further by *Sommer and Chau* (2016). Applying CRI with Capon's method, we showed that PMSE, observed by radar, are patchy. Capon's method of imaging minimizes side lobe detection by weighting each receiver according to the data. To estimate the patch size, we fitted N Gaussian shaped patches after converting the brightness from range to altitude. The patch size varies, depending on the integration period, beam size and geophysics. A statistic of ~ 9 h measurement time is shown in Fig. 6.3. Different beam sizes and integration periods are considered. Longer integration periods lead to larger patches, as the isotropic scattering mechanism will be more homogeneously present at the whole beam volume. The beam size has also an influence on the patch size, as a larger beam would lead to the detection of larger patches. On the other hand, antenna side lobe contributions and

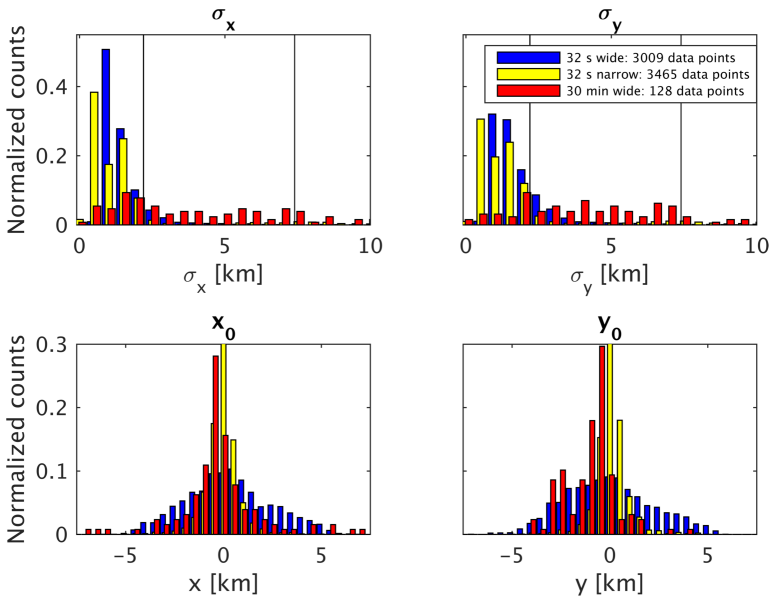

Figure 6.3 Patch size estimations of the brightness distributions. Shown are histograms of fitted widths in x- and y-direction (top row) and center locations (bottom row) of 2D-Gaussian function for all data sets and altitudes containing PMSE. Parameters described in *Sommer and Chau* (2016). For each figure, 3 histograms for two beam width and integration periods are shown. Blue: 32 s, 3.6° narrow beam, yellow: 32 s, 12.6° wide beam, red: 32 min,3.6° wide beam. Figure taken from *Sommer and Chau* (2016), Fig. 6.

non-Gaussian antenna beam pattern lead to the detection of smaller patches of PMSE than the antenna beam volume would suggest. The geophysical component of the small patches is more interesting. Small scale gravity wave activity can change the altitude of PMSE within the beam volume, leading to a not homogenously filled beam volume or patches of fossil or active turbulence can drift through the beam volume (*Cho et al.*, 1996).
Sommer et al. (2016b) and *Sommer and Chau* (2016) discussed the implication of the patchy PMSE observations on different measurement techniques. One finding was, that on short time scales, the assumption of SCA and FCA of a statistically homogeneously filled beam volume is not fulfilled. Another important result is that the aspect sensitivity of PMSE is strongly overestimated.

6.3 In-beam spectral parameter estimation

As presented above, small scale fluctuation in PMSE backscatter exist. These small changes in brightness can be estimated with imaging. Furthermore, imaging can be used to estimate Doppler shift and spectral width as well. A method to estimate SNR, Doppler velocity and spectral width within the beam volume, using PMSE as a tracer, is demonstrated by *Sommer and Chau* (2016). This is especially important with regard to the inhomogeneous nature of PMSE. Without imaging, parts of the beam not

illuminating PMSE would equally weighted as parts filled with PMSE. We showed that imaging can be used to derive maps of all spectral parameters with a higher spatial resolution than conventional DBS scans. An example of the maps are shown in Fig. 6.4, obtained by a wide beam experiment. Using the Doppler velocity maps, we applied a simple DBS approach to derive the horizontal wind component. So imaging can be used do derive maps of all three spectral components. Illuminating a large area and decompose the data regarding space in software, the necessary time for a scanning experiment can be significantly reduced. An example can be found in *Sommer et al.* (2014a), where wide beam scan experiments have been used in conjunction with imaging to improve the temporal resolution compared to a standard scanning experiment by a factor of 4.

Combining the wide beam experiment to derive the winds with a narrow beam experiment to derive the spectral width, *Sommer and Chau* (2016) showed that energy dissipation rate estimations can be improved with imaging. Since *Hocking et al.* (1986) described the energy dissipation derivation based on spectral width estimations by radar, the antenna beam pattern is approximated by the main beam described as a Gaussian function. On the other hand, even HPLA radar systems have a significant side lobe contribution on the spectral width estimation, which was ignored by the approach of *Hocking et al.* (1986). These side lobe contribution widen the spectra and the corrective terms underestimate the beam broadening effect (*Hocking et al.*, 1986; *Nastrom and Eaton*, 1997). This leads to systematically larger derived energy dissipation rates.

In *Sommer and Chau* (2016), we used imaging by composing a synthetic beam, corresponding to the width of the main beam of MAARSY. By identifying and removing side lobe contributions in the spectrum, the spectral width decreases as beam broadening due to side lobes is removed. The correction terms for energy dissipation rates without and with effective narrow beam are the same, as only the main beam is con-

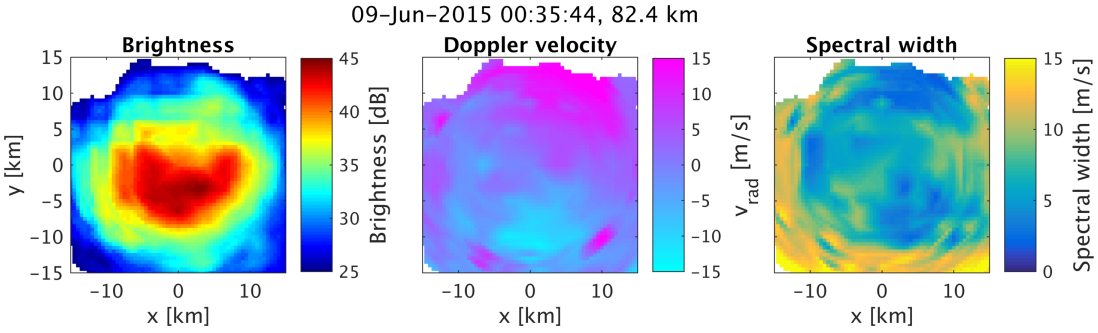

Figure 6.4 Spectral parameter maps of PMSE after converting the image to cartesian coordinates. The brightness distribution is shown in the left panel. It can be used to estimate the patch size of PMSE. The middle panel shows the corresponding radial velocity, derived with imaging. Using a DBS approach, the horizontal wind field could be derived. The right panel shows the spectral width, which can be used to derive energy dissipation rates. Figures similar to *Sommer and Chau* (2016), Figs. 4 and 5.

sidered here. Hence, the derived energy dissipation rates show a decrease of strong events before removing side lobe contribution, leading to a more reliable estimation of the turbulence strength.

Chapter 7 Summary & outlook

Highly resolved observations of PMSE have been made with MAARSY. Combining the different capabilities of a high time and range resolution, fast beam steering and several receiving channels permit to investigate the small scale structure of PMSE as seen by radar. This thesis investigated PMSE on short time scales and their horizontal structure.
PMSE were observed with unrepresented temporal resolution of 2 ms. On these time scales, PMSE showed a surprising behavior of appearing and disappearing power. Further, the observed MAOA showed an apparent rapid motion. All the effects could be observed with two different beam widths, a narrow and a wide beam, which observed quasi-simultaneously the same PMSE. These observations could be explained by an underlying random process, which is modulated by both geophysical and instrumental effects. That was verified with a statistical simulation, which represented the observed data very well. That way, one could distinguish between instrumental influences and geophysical parameters such as turbulence strength.

Furthermore, the angular dependence of PMSE has been investigated. It was shown, considering the beam filling effect and short changes in PMSE strength, that PMSE are caused by mainly isotropic scattering. In addition, the former contradictions of different measurement techniques with isotropic scattering on one side and specular reflection on the other, was resolved. The cause for that is the inhomogeneous nature of PMSE, which was shown. Using in-beam imaging techniques, this thesis demonstrated that PMSE consist generally of patches with sizes of few kilometers, sometimes even smaller than 1 km.
It was shown in this thesis, that different integration times have an impact on the analysis due to the scattering process and patchy nature of PMSE. Very short integration times (< 1 s) show an apparent oscillation in power and apparent high wind velocities. For short integration times (~ 10 s – 40 s), a high correlation in space would suggest a strong angular dependence but is probably due to localized scattering processes. Long integration times (> 10 min) suggest an isotropic scattering process for PMSE.

In addition, in-beam measurement techniques have been used to create maps of SNR, Doppler velocity and spectral width. With such techniques, the amount of time to scan large areas decreases, since the radar beam does not have to be tilted electronically, the tilting is done instead in software. This leads to a shorter scanning time. The spatial information was not only used to derive maps but also to identify side lobe contributions on spectral width estimation. It was shown, that identifying and removing side lobe contribution improves energy dissipation rate estimations by radar and the

estimates are in agreement with in situ measurements and models (*Sommer and Chau*, 2016).

In future, the simulation presented in *Sommer et al.* (2016a) can be used to improve energy dissipation rate estimations by radar. The simulation considers the beam broadening as well as a not completely filled beam volume at the lower edge of PMSE, as radar observes in range and not altitude. By fitting the whole spectrum over all range gates, the background wind, the resulting beam broadening as well es the antenna side lobes are identified, resulting in the turbulence intensity as a fitting parameter. That model should be enhanced by introducing a non-homogenously filled beam volume, in order to consider the findings of *Sommer et al.* (2016b) and *Sommer and Chau* (2016). The wind estimation can be improved also in another way as shown in *Sommer and Chau* (2016) by using virtual beam pointing positions. The scanning time can be reduced significantly (e.g., *Sommer et al.*, 2014a), so this technique, in conjunction with wide beam experiments and very recently installed technical improvements at MAARSY, should be used to derive complete spectral parameters (radial velocity, spectral width), that can then be used to identify short period gravity waves and derive the energy dissipation rates with radar in a continuous way with a better resolution than before. The high resolution of radar imaging might also be used to investigate different turbulence strength in the upper and lower part further. Additionally, more antennas and other techniques could further improve the imaging resolution.
Since this thesis claims, that PMSE is patchy in radar observations, comparison with rocket borne observations should be used to investigate the cause for these small scale fluctuations and highly resolved NLC observations compared to the small scale structures seen in radar observations.
The approaches described here, especially the high range and temporal observations, might also be utilized to investigate polar mesospheric winter echoes further, as their formation is yet not completely understood (*Latteck and Strelnikova*, 2015).

Bibliography

Appleton, E. V., and M. A. F. Barnett, On some direct evidence for downward reflection of electric rays, *Proc. Roy. Soc. London*, *109*(752), 621–641, 1925.

Asmus, H., H. Wilms, B. Strelnikov, and M. Rapp, On the heterogeneous nucleation of mesospheric ice on meteor smoke particles: microphysical modeling, *J. Atmos. Sol. Terr. Phys.*, *118*, 180–189, doi:10.1016/j.jastp.2014.03.009, 2014.

Baldwin, M. P., and T. J. Dunkerton, Stratospheric Harbingers of Anomalous Weather Regimes, *Science*, *294*(5542), 581 – 584, doi:10.1126/science.1063315, 2001.

Balsley, B., and K. Gage, The MST radar technique: Potential for middle atmospheric studies, *Pure Appl. Geophys.*, *118*, 452–493, 1980a.

Balsley, B. B., and K. S. Gage, The MST radar technique: Potential for middle atmospheric studies, *Pageoph*, *118*(1), 452–493, doi:10.1007/BF01586464, 1980b.

Balsley, B. B., W. L. Ecklund, and D. C. Fritts, VHF echoes from the high-latitude mesosphere and lower thermosphere: Observations and interpretations, *J. Atmos. Sci.*, *40*(10), 2451–2466, doi:http://dx.doi.org/10.1175/1520-0469(1983)040<2451:VEFTHL>2.0.CO;2, 1983.

Balsley, B. B., R. F. Woodman, M. Sarango, R. Urbina, J., E. R., Ragaini, and J. Carey, Southern-hemisphere PMSE: where are they?, *Geophys. Res. Lett.*, *20*, 198–1985, 1993.

Balsley, B. B., R. Woodman, M. Sarango, R. Rodriguez, J. Urbina, E. Ragaini, J. Carey, M. Huaman, and A. Giraldez, On the lack of southern hemisphere polar mesosphere summer echoes, *J. Geophys. Res.*, *100*(D6), 11,685–11,693, doi:10.1029/95JD00510, 1995.

Barabash, V., P. Chilson, S. Kirkwood, A. R. K., and Stebel, Investigations of the possible relationship between PMSE and tides using a VHF MST radar, *Geophys. Res. Lett.*, *25*(17), 3297–3300, doi:10.1029/98GL02557, 1998.

Baumgarten, G., and D. C. Fritts, Quantifying Kelvin-Helmholtz instability dynamics observed in noctilucent clouds: 1. Methods and observations, *J. Geophys. Res.*, *119*, 9324–9337, doi:10.1002/2014JD021832, 2014.

Ben-David, C., and A. Leshem, Parametric high resolution techniques for radio astronomical imaging, *IEEE Journal of Selected Topics in Signal Processing*, pp. 670–684, doi:10.1109/JSTSP.2008.2005318, 2008.

Bremer, J., P. Hoffmann, A. Manson, C. E. Meek, R. Rüster, and W. Singer, PMSE observations at three different frequencies in Northern Europe during summer 1994, *Ann. Geophys.*, *14*, 1317–1327, 1996.

Bremer, J., P. Hoffmann, R. Latteck, and W. Singer, Seasonal and long-term variations of PMSE from VHF radar observations at Andenes, Norway, *J. Geophys. Res.*, *108*(D8), 8438, doi:10.1029/2002JD002369, 2003.

Briggs, B. H., On the analysis of moving patterns in geophysics– I. Correlation analysis, *J. Atmos. Terr. Phys.*, *30*(10), 1777–1788, 1968.

Browning, K., and R. Wexler, A determination of kinematic properties of a wind field using doppler radar, *J. Appl. Meteorol.*, *7*, 105–113, 1968.

Capon, J., High-Resolution Frequency-Wavenumber Spectrum Analysis, *Proc. IEEE*, *57*, 1408–1418, 1969.

Chau, J. L., R. J. Doviak, A. Muschinski, and C. L. Holloway, Tropospheric measurements of turbulence and characteristics of Bragg scatterers using the Jicamarca VHF radar, *Radio Sci.*, *35*, 179–193, 2000.

Chau, J. L., F. R. Galindo, C. J. Heinselman, and M. J. Nicolls, Meteor-head echo observations using an antenna compression approach with the 450 MHz Poker Flat Incoherent Scatter Radar, *J. Atmos. Sol. Terr. Phys.*, *71*, 636–643, doi:10.1016/j.jastp.2008.08.007, 2009.

Chau, J. L., T. Renkwitz, G. Stober, and R. Latteck, MAARSY multiple receiver phase calibration using radio sources, *J. Atmos. Sol. Terr. Phys.*, doi:10.1016/j.jastp.2013.04.004, 2014.

Chen, J.-S., and M. Zecha, Multiple-frequency range imaging using the OSWIN VHF Radar: Phase calibration and first results, *Radio Science*, *44*, doi:10.1029/2008RS003916, 2009.

Chen, J.-S., P. Hoffmann, M. Zecha, and J. Röttger, On the relationship between aspect sensitivity, wave activity, and multiple scattering centers of mesosphere summer echoes: a case study using coherent radar imaging, *Ann. Geophys.*, *22*, 807–817, 2004.

Chen, J.-S., P. Hoffmann, M. Zecha, and C.-H. Hsieh, Coherent radar imaging of mesosphere summer echoes: Influence of radar beam pattern and tilted structures on atmospheric echo center, *Radio Sci.*, *43*(1), RS1002, doi:10.1029/2006RS003593, 2008.

Chilson, P. B., P. Czechowsky, J. Klostermeyer, R. Rüster, and G. Schmidt, An investigation of measured temperature profiles and VI-IF mesosphere summer echoes at midlatitudes, *Journal of Geophys*, *102*(D20), 23,819–23,828, 1997.

Chilson, P. B., S. Kirkwood, and L. Häggström, Frequency domain interferometry mode observations of PMSE using the EISCAT VHF radar, *Annales Geophysicae*, *18*(12), 1599–1612, 2000.

Chilson, P. B., T.-Y. Yu, R. D. Palmer, and S. Kirkwood, Aspect sensitivity measurements of polar mesosphere summer echoes using coherent radar imaging, *Ann. Geophys.*, *20*, 213–223, 2002.

Cho, J. Y. N., T. M. Hall, and M. C. Kelley, on the role of charges aerosols in polar mesosphere summer echoes, *J. Geophys. Res*, *97*(D1), 875–886, 1992.

Cho, J. Y. N., C. M. Alcala, M. C. Kelley, and W. E. Swartz, Further effects of charged aerosols on summer mesospheric radar scatter, *Journal of Atmospheric and Terrestrial Physics*, *58*, 661–672, 1996.

Czechowsky, P., R. Ruster, and G. Schmidt, Variations of mesospheric structures in different seasons, *Geophys. Res. Lett.*, *6*(6), 459–462, 1979.

Czechowsky, P., I. M. Reid, and R. Rüster, VHF radar measurements of the aspect sensitivity of the summer polar mesopause echoes over Andenes (69°N, 16°E), Norway, *Geophys. Res. Lett*, *15*, 1259–1262, 1988.

Czechowsky, P., I. M. Reid, R. Rüster, and G. Schmidt, VHF Radar Echoes Observed in the Siummer and Winter Polar Mesosphere Over Andøya, Norway, *J. Geophys. Res.*, *94*, 5199–5217, 1989.

Doviak, R. J., R. J. Lataitis, C. L. Holloway, and J. V. Baelen, A generalized theoretical analysis of cross-correlation and cross-spectra for spaced-antenna wind profilers, *Tech. rep.*, Natl. Cent. for Atmos. Res., Boulder, Colo., 1994.

Doviak, R. J., R. J. Lataitis, and C. L. Holloway, Cross correlations and cross spectra for spaced antenna wind profilers: 1. Theoretical analysis, *Radio Sci.*, *31*, 157–180, 1996.

Ecklund, W., D. Carter, and B. Balsley, Continuous measurement of upper atmospheric winds and turbulence using a VHF Doppler radar: preliminary results, *Journal of Atmospheric and Terrestrial Physics*, *41*(9), 983–994, doi:10.1016/0021-9169(79)90099-0, 1979.

Ecklund, W. L., and B. B. Balsley, Long-term observations of the Arctic mesosphere with the MST radar at Poker Flat, Alaska, *J. Geophys. Res.*, *86*(A9), 7775–7780, doi:10.1029/JA086iA09p07775, 1981.

Engler, N., R. Latteck, B. Strelnikov, W. Singer, and M. Rapp, Turbulent energy dissipation rates observed by Doppler MST Radar and by rocket-borne instruments during the MIDAS/MaCWAVE campaign 2002, *Ann. Geophys.*, *23*, 1147–1156, doi:1432-0576/ag/2005-23-1147, 2005.

Fenn, A. J., *Adaptive antenna and phased arrays for radar and communication*, Artech House, 2007.

Fukao, S., and K. Hamazu, *Radar for Meteorological and Atmospheric Observations*, Springer Japan, doi:10.1007/978-4-431-54334-3, 2014.

Grossmann, K. U., H. G. Brückelmann, D. Offermann, P. Schwabbauer, R. Gyger, K. Künzi, G. K. Hartmann, C. A. Barth, R. Thomas, A. F. Chijov, S. P. Perov, V. A. Yushov, P. Glöde, and K. H. Grasnick, Middle atmosphere abundances of water vapor and ozone during MAP/WINE, *J. Atmos. Terr. Phys.*, *49*, 827–841, 1987.

Hall, C. M., S. Nozawa, A. H. Manson, and C. E. Meek, Determination of turbulent energy dissipation rate directly from MF-radar determined velocity, *Earth Planets Space*, *52*, 137–141, 2000.

Hassenpflug, G., P. B. Rao, M. Yamamoto, and S. Fukao, MU radar spaced antenna observations with varying apertures: Scatterer and antenna contributions to the ground diffraction pattern, *Radio Sci.*, *38*(3), 1043, doi:10.1029/2002RS002751, 2003.

Hecht, J. H., A. Z. Liu, R. L. Walterscheid, S. J. Franke, R. J. Rudy, M. J. Taylor, and P.-D. Pautet, Characteristics of short-period wavelike features near 87 km altitude from airglow and lidar observations over Maui, *Journal of Geophysical Research: Atmospheres*, *112*(D16), D16101, doi:10.1029/2006JD008148, 2007.

Heisenberg, W., Zur statistischen Theorie der Turbulenz, *Z. Physik*, *124*, 628–657, 1948.

Hocking, Observation and measurement of turbulence in the middle atmosphere with a VHF radar, *Journal of Atmospheric and Terrestrial Physics*, *48*(7), 655–670, 1986.

Hocking, W. K., Measurement of turbulent energy dissipation rates in the middle atmosphere by radar techniques: A review, *Radio Sci.*, *20*(6), 1403–1422, 1985.

Hocking, W. K., R. Ruster, and P. Czechowsky, Absolute reflectivities and aspect sensitivities of VHF radiowave scatterers measured with the SOUSY radar, *J. Atmos. Terr. Phys.*, *48*(2), 131–144, 1986.

Hocking, W. K., S. Fukao, T. Tsuda, M. Yamamoto, T. Sato, and S. Kato, Aspect sensitivity of stratospheric VHF radio-wave scatterers, particularly above 15-km altitude, *Radio Sci.*, *25*(4), 613–627, 1990.

Hoffmann, P., W. Singer, and J. Bremer, Mean seasonal and diurnal variations of PMSE and winds from 4 years of radar observations at ALOMAR, *Geophys. Res. Lett.*, *26*(11), 1525–1528, doi:10.1029/1999GL900279, 1999.

Hoffmann, P., M. Rapp, A. Serafimovich, and R. Latteck, On the occurrence and formation of multiple layers of polar mesosphere summer echoes, *Geophys. Res. Lett.*, *32*(5), L05812, doi:10.1029/2004GL021409, 2005.

Höffner, J., and F.-J. Lübken, Potassium lidar temperatures and densities in the mesopause region at Spitsbergen (78°N), *Journal of Geophysical Research*, D20114, doi:10.1029/2007JD008612, 2007.

Holdsworth, D. A., Spatial correlation analysis revisited: Theory, and application to "radar backscatter model" data, *Radio Sci.*, *34*(3), 629–641, 1999.

Holloway, R. J. Christopher L., Doviak, and S. A. Cohn, Cross correlations of fields scattered by horizontally anisotropic refractive index irregularities, *Radio Sci.*, *32*(5), 1911–1920, doi:10.1029/97RS00715, 1997.

Holton, J. R., and M. J. Alexander, The role of waves in the transport circulation of the middle atmosphere, *Washington DC American Geophysical Union Geophysical Monograph Series*, *123*, 21–35, doi:10.1029/GM123p0021, 2000.

Hoppe, U.-P., and D. C. Fritts, High-resolution measurements of vertical velocity with the European incoherent scatter VHF radar 1. Motion field characteristics and measurement biases, *J. Geophys. Res.*, *100*, 16,813–16,825, 1995.

Hoppe, U. P., C. Hall, and J. Röttger, 1st observations of summer polar mesospheric backscatter with a 224 MHZ radar, *Geophys. Res. Lett.*, *15*(1), 28–31, 1988.

Hoppe, U.-P., D. C. Fritts, I. M. Reid, P. Czechowsky, C. M. Hall, and T. L. Hansen, Multiple-frequency studies of the high-latitude summer mesosphere: implications for scattering processes, *J. Atmos. Terr. Phys.*, *52*, 907–926, doi:10.1016/0021-9169(90)90024-H, 1990.

Horinouchi, T., T. Nakamura, and J.-i. Kosaka, Convectively generated mesoscale gravity waves simulated throughout the middle atmosphere, *Geophysical Research Letters*, *29*(21), 3–1–3–4, 2002.

Huaman, M. M., and B. B. Balsley, Long-term-mean aspect sensitivity of PMSE determined from Poker Flat MST radar data, *Geophys. Res. Lett.*, *25*, 947–950, 1998.

Huaman, M. M., and B. B. Balsley, Differences in near-mesopause summer winds, temperatures, and water vapor at northern and southern latitudes as possible causal factors for inter-hemispheric PMSE differences, *Geophys. Res. Lett.*, *26*(11), 1529–1532, doi:10.1029/1999GL900294, 1999.

Hunten, D. M., R. P. Turco, and O. B. Toon, Smoke and dust particles of meteoric origin in the mesosphere and stratosphere, *J. Atmos. Sci.*, *37*(6), 1342–1357, doi:10.1175/1520-0469(1980)037<1342:SADPOM>2.0.CO;2, 1980.

Hysell, D. L., and J. L. Chau, Optimal aperture synthesis radar imaging, *Radio Sci.*, *41*(December 2005), 1–12, doi:10.1029/2005RS003383, 2006.

Kaifler, N., G. Baumgarten, J. Fiedler, and F.-J. Lübken, Quantification of waves in lidar observations of noctilucent clouds at scales from seconds to minutes, *Atmos. Chem. Phys.*, *13*, 11,757–11,768, doi:10.5194/acp-13-11757-2013, 2013.

Karashtin, A. N., Y. V. Shlyugaev, V. I. Abramov, I. F. Belov, I. V. Berezin, V. V. Bychkov, E. B. Eryshev, and G. P. Komrakov, First HF radar measurements of summer mesopause echoes at SURA, *Ann. Geophys.*, *15*(7), 935–941, 1997.

Kelley, M. C., D. T. Farley, and J. Röttger, The effect of cluster ions on anomalous VHF backscatter from the summer polar mesosphere, *Geophysical Research Letters*, *14*(10), 1031–1034, doi:10.1029/GL014i010p01031, 1987.

Kirkwood, S., I. Wolf, H. Nilsson, P. Dalin, D. Mikhaylova, and E. Belova, Polar mesosphere summer echoes at Wasa, Antarctica (73° S): First observations and comparison with 68° N, *Geophys. Res. Lett.*, *34*(15), L15803, doi:10.1029/2007GL030516, 2007.

Kudeki, E., and G. R. Stitt, Frequency domain interferometry: A high resolution radar technique for studies of atmospheric turbulence, *Geophys. Res. Lett.*, *14*(3), 198–201, 1987.

Kudeki, E., and F. Sürücü, Radar interferometric imaging of field-aligned plasma irregularities in the equatorial electrojet, *Geophys. Res. Lett*, *18(1)*, 41–44, doi:doi:10.1029/90GL02603, 1991.

Latteck, R., and J. Bremer, Long-term changes of polar mesosphere summer echoes at 69°N, *J. Geophys. Res.*, *118*, 10,441–10,448, doi:10.1002/jgrd.50787, 2013.

Latteck, R., and I. Strelnikova, Extended observations of polar mesosphere winter echoes over Andøya (69°N) using MAARSY, *Journal of Geophysical Research*, *120*, 8216–8226, doi:10.1002/2015JD023291, 2015.

Latteck, R., W. Singer, and H. Bardey, The ALWIN MST Radar: Technical Design and Performance, *European Rocket and Balloon Programs and Related Research,* Proceedings of the 14th ESA Symposium held 31 May-3 June, 1999 in Potsdam. Edited by B. Schürmann. European Space Agency, ESA-SP., *437*, 179–184, 1999.

Latteck, R., W. Singer, and W. K. Hocking, Measurement of turbulent kinetic energy dissipation rates in the mesosphere by a 3 MHz Doppler radar, *Adv. Space Res.*, *35*(11), 1905–1910, 2005.

Latteck, R., W. Singer, R. J. Morris, D. A. Holdsworth, and D. J. Murphy, Observation of polar mesosphere summer echoes with calibrated VHF radars at (69°N) in the Northern and Southern Hemispheres, *Geophys. Res. Lett.*, L14805, doi:10.1029/2007GL030032, 2007.

Latteck, R., W. Singer, R. J. Morris, W. K. Hocking, D. J. Murphy, D. A. Holdsworth, and N. Swarnalingam, Similarities and differences in polar mesosphere summer echoes observed in the Arctic and Antarctica, *Ann. Geophys.*, *26*, 2795–2806, 2008.

Latteck, R., W. Singer, M. Rapp, B. Vandepeer, T. Renkwitz, M. Zecha, and G. Stober, MAARSY: The new MST radar on Andøya-System description and first results, *Radio Sci.*, *47*, RS1006, doi:10.1029/2011RS004775, 2012.

Lau, E. M., S. K. Avery, J. P. Avery, D. Janches, S. E. Palo, R. Schafer, and N. A. Makarov, Statistical characterization of the meteor trail distribution at the South Pole as seen by a VHF interferometric meteor radar, *Radio Sci.*, *41*(4), RS4007, doi:10.1029/2005RS003247, 2006.

Lee, Y.-S., S. Kirkwood, Y.-S. Kwak, K.-C. Kim, and G. G. Shepherd, Polar summer mesospheric extreme horizontal drift speeds during interplanetary corotating interaction regions (CIRs) and high-speed solar wind streams: Coupling between the solar wind and the mesosphere, *J. Geophys. Res.*, *119*, 3883–3894, doi:10.1002/2014JA019790, 2014.

Li, Q., and M. Rapp, PMSE-observations with the EISCAT VHF and UHF-radars: Ice particles and their effect on ambient electron densities, *Journal of Atmospheric and Solar-Terrestrial Physics*, *104*, 270–276, doi:10.1016/j.jastp.2012.10.015, 2013.

Li, Q., M. Rapp, J. Röttger, R. Latteck, M. Zecha, I. Strelnikova, G. Baumgarten, M. Hervig, C. Hall, and M. Tsutsumi, Microphysical parameters of mesospheric ice clouds derived from calibrated observations of polar mesosphere summer echoes at Bragg wavelengths of 2.8 m and 30 cm, *J. Geophys. Res.*, *115*, doi:10.1029/2009JD012271, 2010.

Lindzen, R., Multiple gravity-wave breaking levels, *J. Atmos. Sci.*, *42*, 301–305, doi:10.1175/1520-0469(1985)042<0301:MGWBL>2.0.CO;2, 1985.

Lübken, F.-J., Seasonal variation of turbulent energy dissipation rates at high latitudes as determined by in situ measurements of neutral density fluctuations, *J. Geophys. Res.*, *102*, 13,413–441,456, 1997.

Lübken, F.-J., Turbulent scattering for radars: A summary, *J. Atmos. Sol. Terr. Phys.*, *107*, 1–7, doi:10.1016/j.jastp.2013.10.015, 2013.

Lübken, F.-J., U. von Zahn, A. Manson, C. Meek, U.-P. Hoppe, F. J. Schmidlin, J. Stegman, D. P. Murtagh, R. Rüster, G. Schmidt, H.-U. Widdel, and P. Espy, Mean state densities, temperatures and winds during the MAC/SINE and MAC/EPSILON campaigns, *J. Atmos. Terr. Phys.*, *52*, 955–970, 1990.

Lübken, F.-J., W. Hillert, G. Lehmacher, and U. von Zahn, Experiments revealing small impact of turbulence on the energy budget of the mesosphere and lower thermosphere, *J. Geophys. Res.*, *98*, 20,369–20,384, 1993.

Lübken, F.-J., M. Rapp, and P. Hoffmann, Neutral air turbulence and temperatures in the vicinity of polar mesosphere summer echoes, *J. Geophys. Res.*, *107*(D15), 4273, doi:10.1029/2001JD000915, 2002.

Lübken, F.-J., M. Zecha, J. Höffner, and J. Röttger, Temperatures, polar mesosphere summer echoes, and noctilucent clouds over Spitsbergen (78° N), *J. Geophys. Res*, *109*(D11), doi:10.1029/2003JD004247, 2004.

Matthias, V., P. Hoffmann, M. Rapp, and G. Baumgarten, Composite analysis of the temporal development of waves in the polar MLT region during stratospheric warmings, *Journal of Atmospheric and Solar-Terrestrial Physics*, *90–91*, 86–96, doi:10.1016/j.jastp.2012.04.004, 2012.

Murphy, D., W. Hocking, and D. Fritts, An assessment of the effect of gravity waves on the width of radar Doppler spectra, *Journal of Atmospheric and Terrestrial Physics*, *56*(1), 17–29, doi:http://dx.doi.org/10.1016/0021-9169(94)90172-4, 1994.

Nastrom, G. D., and F. D. Eaton, Turbulence eddy dissipation rates from radar observations at 5-20 km at White Sands Missile Range, New Mexico, *J. Geophys. Res.*, *102*, 19,495–19,505, 1997.

Nicolls, M. J., C. J. Heinselman, E. A. Hope, S. Ranjan, M. C. Kelley, and J. D. Kelly, Imaging of Polar Mesosphere Summer Echoes with the 450 MHz Poker Flat Advanced Modular Incoherent Scatter Radar, *Geophys. Res. Lett.*, *34*(L20102), doi:10.1029/2007GL031476, 2007.

Nilsson, H., S. Kirkwood, R. J. Morris, R. Latteck, A. Klekociuk, D. J. Murphy, M. Zecha, and E. Belova, Simultaneous observations of polar mesosphere summer echoes at two different latitudes in Antarctica, *Ann. Geophys.*, *26*, 3783–792, 2008.

Nussbaumer, V., K.-H. Fricke, M. Langer, W. Singer, and U. von Zahn, First simultaneous and common-volume observations of NLC and PMSE by lidar and radar, *J. Geophys. Res.*, *101*, 19,161–19,167, 1996.

Palmer, R. D., S. Gopalam, T. Y. Yu, and S. Fukao, Coherent radar imaging using Capon's method, *Radio Sci.*, *33*(6), 1585–1598, 1998.

Palmer, R. D., T.-Y. Yu, and P. B. Chilson, Range imaging using frequency diversity, *Radio Science*, *34*(6), 1485–1496, doi:10.1029/1999RS900089, 1999.

Picone, J. M., A. E. Hedin, D. P. Drob, and A. C. Aikin, NRL-MSISE-00 Empirical Model of the Atmosphere: Statistical Comparisons and Scientific Issues, *J. Geophys. Res*, *107*(A12), SIA 15–1–SIA 15–16, doi:10.1029/2002JA009430, 2002.

Plane, J. M. C., The role of sodium bicarbonate in the nucleation of noctilucent clouds, *Ann. Geophys.*, *18*(7), 807–814, 2000.

Rapp, M., and U.-P. Hoppe, A reconsideration of spectral width measurements in PMSE with EISCAT, *Adv. Space Res.*, *38*, 2408–2412, 2006.

Rapp, M., and F.-J. Lübken, On the nature of PMSE: Electron diffusion in the vicinity of charged pairarticles revisited, *J. Geophys. Res.*, *108*(D8), 8437, doi:10.1029/2002JD002857, 2003.

Rapp, M., and F.-J. Lübken, Polar mesosphere summer echoes (PMSE): review of observations and current understanding, *Atmos. Chem. Phys.*, *4*, 2601–2633, 2004.

Rapp, M., and G. E. Thomas, Modeling the microphysics of mesospheric ice particles: Assessment of current capabilities and basic sensitivities, *J. Atmos. Sol. Terr. Phys.*, *68*, 715–744, 2006.

Rapp, M., F.-J. Lübken, P. Hoffmann, R. Latteck, G. Baumgarten, and T. Blix, PMSE dependence on aerosol charge number density and aerosol size, *J. Geophys. Res.*, *108*(D8), doi:10.1029/2002JD002650, 2003.

Rapp, M., B. Strelnikov, A. Müllemann, F.-J. Lübken, and D. C. Fritts, Turbulence measurements and implications for gravity wave dissipation during the MaCWAVE/MIDAS rocket program, *Geophys. Res. Lett.*, *31*, L24S07, doi:0.1029/2003GL019325, 2004.

Rapp, M., I. Strelnikova, R. Latteck, P. H. andUlf Peter Hoppe, I. Häggström, and M. T. Rietveld, Polar mesosphere summer echoes (PMSE) studied at Bragg wavelengths of 2.8 m, 67 cm, and 16 cm, *Journal of Atmospheric and Solar-Terrestrial Physics*, *70*(7), 947–961, doi:doi:10.1016/j.jastp.2007.11.005, 2008.

Rapp, M., I. Strelnikova, B. Strelnikov, P. Hoffmann, M. Friedrich, J. Gumbel, L. Megner, U.-P. Hoppe, S. Robertson, S. Knappmiller, M. Wolff, and D. R. Marsh, Rocket-borne in situ measurements of meteor smoke: Charging properties and implications for seasonal variation, *J. Geophys. Res.*, *115*, D00I16, doi:10.1029/2009JD012725, 2010.

Reid, I. M., P. Czechowsky, R. Rüster, and G. Schmidt, First VHF radar measurements of mesopause summer echoes at mid-latitudes, *Geophys. Res. Lett*, *16*(2), 135–138, doi:10.1029/GL016i002p00135, 1989.

Ridder, C., Relationship of gravity waves and small scale variations in noctilucent clouds, Master's thesis, Universität Rostock, 2014.

Röttger, J., and C. LaHoz, Characteristics of polar mesosphere summer echoes (PMSE) observed with the EISCAT 224 MHz radar and possible explanations of their origin, *J. Atmos. Terr. Phys.*, *52*, 93–906, 1990.

Röttger, J., C. La Hoz, M. C. Kelley, U.-P. Hoppe, and C. Hall, The structure and dynamics of polar mesosphere summer echoes observed with the EISCAT 224 MHz radar, *Geophys. Res. Lett.*, *15*, 1353–1356, 1988.

Röttger, J., C. La Hoz, S. Franke, and C. Liu, Steepening of re ectivity structures detected in high-resolution Doppler spectra of polar mesosphere summer echoes (PMSE) observed with the EISCAT 224-MHz radar, *J. Atmos. Terr. Phys.*, *52*, 939–954, 1990.

Röttger, J., M. T. Rietveld, C. La Hoz, T. Hall, M. C. Kelley, and W. E. Swartz, Polar mesosphere summer echoes observed with the EISCAT 933-MHz radar and the CUPRI 46.9-MHz radar, their similarity to 224-MHz radar echoes, and their relation to turbulence and electron density profiles, *Radio Sci.*, *25*(4), 671–687, doi:10.1029/RS025i004p00671, 1990.

Rüster, R., Analysis and Interpretation of VHF-radar data, *Ann. Geophys.*, *12*(8), 725–732, 1994.

Rüster, R., High resolution measurements in the summer polar mesosphere, *Geophys. Res. Lett*, *24*(9), 1115–1118, 1997.

Schult, C., G. Stober, J. L. Chau, and R. Latteck, Determination of meteor-head echo trajectories using the interferometric capabilities of MAARSY, *Ann. Geophys.*, *31*, 1843–1851, doi:10.5194/angeo-31-1843-2013, 2013.

Seele, C., and P. Hartogh, Water vapor of the polar middle atmosphere: annual variation and summer mesosphere conditions as observed by ground-based microwave spectroscopy, *Geophys. Res. Lett.*, *26*, 1517–1520, 1999.

Smirnova, M., E. Belova, and S. Kirkwood, Aspect sensitivity of polar mesosphere summer echoes based on ESRAD MST radar measurements in Kiruna, Sweden in 1997-2010, *Ann. Geophys.*, *30*, 457–465, 2012.

Smith, E. K., and S. Weintraub, The Constants in the Equation for Atmospheric Refractive Index at Radio Frequencies, *J. Res. Nat. Bur. Stand.*, *50*(1), 39–41, 1953.

Sommer, S., and J. L. Chau, Patches of polar mesospheric summer echoes characterized from radar imaging observations with MAARSY, unpublished manuscript, 2016.

Sommer, S., G. Stober, C. Schult, M. Zecha, and R. Latteck, Investigation of horizontal structures at mesospheric altitudes using coherent radar imaging, *Adv. Radio Sci.*, *11*, 319–325, doi:10.5194/ars-11-319-2013, 2013.

Sommer, S., J. Chau, and G. Stober, Wind and spectral width estimations in PMSE with coherent radar imaging, in *General Assembly and Scientific Symposium (URSI GASS), 2014 XXXIth URSI*, doi:10.1109/URSIGASS.2014.6929775, 2014a.

Sommer, S., G. Stober, and J. L. Chau, Geometric considerations of polar mesospheric summer echoes in tilted beams using coherent radar imaging, *Adv. Radio Sci.*, *12*, 197–203, doi:10.5194/ars-12-197-2014, 2014b.

Sommer, S., J. L. Chau, and C. Schult, On high time-range resolution observations of PMSE: statistical characteristics, *J. Geophys. Res.*, accepted, 2016a.

Sommer, S., G. Stober, and J. L. Chau, On the angular dependence and scattering model of Polar Mesospheric Summer Echoes at VHF, *J. Geophys. Res.*, *121*, 278–288, doi:10.1002/2015JD023518, 2016b.

Stober, G., S. Sommer, M. Rapp, and R. Latteck, Investigation of gravity waves using horizontally resolved radial velocity measurements, *Atmos. Meas. Tech.*, *6*, 2893–2905, doi:10.5194/amt-6-2893-2013, 2013.

Stober, G., S. Sommer, C. Schult, and R. Latteck, Observation of Kelvin-Helmholtz instabilities and short period gravity waves above Andenes in Northern Norway, *Journal of Geophysical Research*, submitted, 2016.

Strelnikov, B., M. Rapp, T. A. Blix, N. Engler, J. Höffner, J. Lautenbach, F.-J. Lübken, B. Smiley, and M. Friedrich, In situ observations of small scale neutral and plasma dynamics in the mesosphere/lower thermosphere at 79°N, *Adv. Space Res.*, *38*, 2388–2393, 2006.

Strelnikov, B., F.-J. Lübken, M. Rapp, H. Henkel, and H.-J. Heckl, TURB3D: New rocket-borne multi-sensor system to study three-dimensional structures of mesospheric turbulence, in *ESA15*, pp. 101–105, 2015.

Strelnikova, I., Mesospheric aerosol particles: Evidence from rocket and radar techniques, Ph.D. thesis, Rostock University, 2009.

Swarnalingam, N., W. K. Hocking, and J. R. Drummond, Long-term aspect-sensitivity measurements of polar mesosphere summer echoes (PMSE) at Resolute Bay using a 51.5 MHz VHF radar, *J. Atmos. Sol. Terr. Phys.*, *73*, 957–964, 2011.

Taubenheim, J., The role of atmospheric pressure variations above the mesopause in the phenomena of winter anomaly and variability of the lower ionosphere, *Gerlands Beitr. Geophysik*, *81*, 396–402, 1972.

Thomas, G. E., Are noctilucent clouds harbingers of global change in the middle atmosphere ?, *Adv. Space Res.*, *32*(9), 1737–1746, doi:10.1016/S0273-1177(03)90470-4, 2003.

Thomas, L., and I. Astin, The form of metre-scale turbulence at mesopause heights in summer, *Journal of Atmospheric and Terrestrial Physics*, *56*(4), 467–478, doi:doi:10.1016/0021-9169(94)90195-3, 1994.

Thomas, L., I. Astin, and I. Prichard, The characteristics of VHF echoes from the summer mesopause region at mid-latitudes, *J. Atmos. Terr. Phys.*, *54*, 969–977, doi:10.1016/0021-9169(92)90063-Q, 1992.

Tsutsumi, M., and T. Aso, MF radar observations of meteors and meteor-derived winds at Syowa (69°S, 39°E), Antarctica: A comparison with simultaneous spaced antenna winds, *J. Geophys. Res.*, *110*, D24111, doi:10.1029/2005JD005849, 2005.

Van Baelen, J. S., T. Tsuda, A. D. Richmond, S. K. Avery, S. Kato, S. Fukao, and M. Yamamoto, Comparison of VHF Doppler beam swinging and spaced antenna observations with the MU radar: First results, *Radio Science*, *25*(4), 629–640, doi:10.1029/RS025i004p00629, 1990.

Van Zandt, T. E., A brief history of the development of wind-profiling or MST radars, *Annales Geophysicae*, *18*, 740–749, 2000.

Varney, R. H., M. C. Kelley, M. J. Nicolls, C. J. Heinselman, and R. L. Collins, The electron density dependence of polar mesospheric summer echoes, *Journal of Atmospheric and Solar-Terrestrial Physics*, *73*(14–15), 2153–2165, doi:doi:10.1016/j.jastp.2010.07.020, 2011.

von Zahn, U., Are Noctilucent Clouds Truly a „Miner's Canary" for Global Change?, *EOS*, *84*(28), 261–264, 2003.

von Zahn, U., and J. Bremer, Simultaneous and common-volume observations of noctilucent clouds and polar mesosphere summer echoes, *Geophys. Res. Lett.*, *26*, 1521–1524, 1999.

Waldteufel, P., and H. Corbin, On the analysis of single Doppler data, *J. Appl. Meteorol.*, *18*, 53–542, 1979.

Witt, G., J. Martin-Löf, N. Wilhelm, and W. Smith, High latitude summer mesospheric temperatures and winds with particular regard to noctilucent clouds, *Space Research V*, pp. 820–821, 1965.

Woodman, R., and A. Guillén, Radar observations of winds and turbulence in the stratosphere and mesosphere, *J. Atmos. Sci.*, *31*, 493ÃćâĆňâĂIJ505, 1974.

Woodman, R. F., B. B. Balsley, F. Aquino, L. Flores, E. Vazquez, M. Sarango, M. M. Huamann, and H. Soldi, First observations of polar mesosphere summer echoes in Antarctica, *J. Geophys. Res.*, *104*(A10), 22,577–22,590, doi:10.1029/1999JA900226, 1999.

Yu, T.-Y., and R. D. Palmer, Atmospheric radar imaging using multiple-receiver and multiple-frequency techniques, *Radio Science*, *36*(6), 1493, 2001.

Yu, T. Y., R. D. Palmer, and D. L. Hysell, A simulation study of coherent radar imaging, *Radio Sci.*, *35*(5), 1129–1141, 2000.

Yu, T.-Y., R. D. Palmer, and P. B. Chilson, An investigation of scattering mechanisms and dynamics on PMSE using coherent radar imaging, *J. Atmos. Sol. Terr. Phys.*, *63*, 1797–1810, 2001.

Zecha, M., J. Röttger, W. Singer, P. Hoffmann, and D. Keuer, Scattering properties of PMSE irregularities and refinement of velocity estimates, *J. Atmos. Sol. Terr. Phys.*, *63*, 201–214, 2001.

Zecha, M., J. Bremer, R. Latteck, W. Singer, and P. Hoffmann, Properties of midlatitude mesosphere summer echoes after three seasons of VHF radar observations at 54◦N, *J. Geophys. Res.*, *108*(D8), 8439, doi:10.1029/2002JD002442, 2003.

Appendix A Sommer et al. (2014)

Adv. Radio Sci., 12, 1–7, 2014
www.adv-radio-sci.net/12/1/2014/
doi:10.5194/ars-12-1-2014

Advances in Radio Science
Open Access Proceedings

Geometric considerations of polar mesospheric summer echoes in tilted beams using coherent radar imaging

S. Sommer, G. Stober, J. L. Chau, and R. Latteck

Leibniz Institute of Atmospheric Physics at the University of Rostock, Schlossstr. 6, 18225 Kühlungsborn, Germany

Correspondence to: S. Sommer (sommer@iap-kborn.de)

Abstract. We present observations of polar mesospheric summer echoes (PMSE) using the Middle Atmosphere Alomar Radar System in Northern Norway (69.30° N, 16.04° E). The radar is able to resolve PMSE at high spatial and temporal resolution and to perform pulse-to-pulse beam steering. In this experiment, 81 oblique beam directions were used with off-zenith angles up to 25°. For each beam pointing direction and range gate, coherent radar imaging was applied to determine the mean backscatter location. The location of the mean scatterer in the beam volume was calculated by the deviation from the nominal off-zenith angle of the brightest pixel. It shows that in tilted beams with an off-zenith angle greater than 5°, structures appear at the altitudinal edges of the PMSE layer. Our results indicate that the mean influence of the location of the maximum depends on the tilt of the beam and on the observed area of the PMSE layer. At the upper/lower edge of the PMSE layer, the mean backscatter has a greater/smaller off-zenith angle than the nominal off-zenith angle. This effect intensifies with greater off-zenith beam pointing direction, so the beam filling factor plays an important role in the observation of PMSE layers for oblique beams.

1 Introduction

Strong VHF backscatter at mesospheric heights in polar regions were described by Ecklund and Balsley (1981) for the first time. As these echoes occur only during the summer months, they were named polar mesospheric summer echoes (PMSE). PMSE are caused by inhomogeneities in the electron density of a size comparable to the radar Bragg wave length (3 m at 50 MHz radar frequency) in the presence of negatively charged aerosol particles. Different aspects of PMSE have been studied with radars around 50 MHz since their first observation, in particular the spectral width (Czechowsky and Rüster, 1997; Blix, 1999) or aspect sensitivity (Röttger and Vincent, 1978; Hocking et al., 1986) to understand the formation of these echoes. A review of the understanding of PMSE was done by Rapp and Lübken (2004), where the formation was explained by the presence of heavy charged ice particles. These ice particles lead to a significantly reduced electron diffusivity and explain the existence of PMSE in the presence of neutral air turbulence. This widely accepted theory explains the overall formation, but still the inner structure of the PMSE is mostly unknown. The limiting factor of the observation of the small scale structures is the relatively wide beam width, so interferometric techniques has been applied to gain insight into finer structures of PMSE.

In the last two decades, imaging methods developed for astronomical applications have been applied to atmospheric studies (Kudeki and Sürücü, 1991; Hysell and Chau, 2006). Together with flexible radar systems with interferometric capabilities, in-beam estimates have been done with different radars (Yu et al., 2001; Chilson et al., 2002; Chen et al., 2004; Sommer et al., 2013) to investigate PMSE. Coherent Radar Imaging (CRI) of PMSE has been usually applied with a vertical radar beam and method called Capon (e.g., Palmer et al., 1998). CRI weights the signal of several spatially separated receivers to resolve different backscatter locations within the beam volume. In the last few years, multiple beam experiments were combined with CRI to understand PMSE (Chen et al., 2008), to improve wind measurements (Sureshbabu et al., 2013) and to measure aspect sensitivity in the troposphere (Chen and Furumoto, 2013). The combination of multiple beam experiments with CRI allows to cover a large area at a high angular resolution.

In this study we present results obtained with the Middle Atmosphere Alomar Radar System (MAARSY) at Andøya in Northern Norway (69.30° N, 16.04° E). The purpose of MAARSY is to investigate the dynamics of the mesosphere

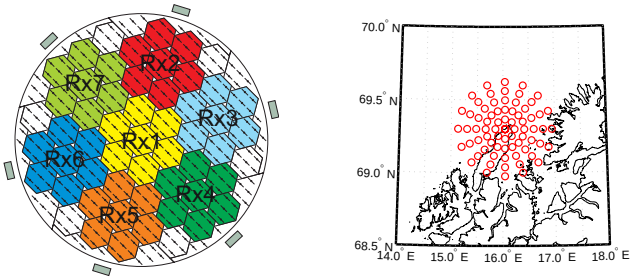

Figure 1. Left: Sketch of the antenna array. The 7 anemones indicated by different colors were used for reception. Right: Beam pointing directions of the CRI experiment setup. The black lines indicate the coast of Northern Norway, the red circles indicate the areas illuminated by the radar beams at about 85 km altitude.

by studying wind and waves on a high spatial and temporal resolution and also the inner structure of PMSE, such as thin layers, that cannot be resolved by standard measurement techniques. For example, PMSE can be used as a tracer for wind measurements. In order to improve the derivation of gravity wave parameter out of wind measurements (Stober et al., 2012), the experiment should have a better spatial resolution. We have used MAARSY with a vertical and several oblique beams and applied CRI for different range gates and beam pointing directions. This allows us to determine the fine structure of PMSE in the vertical as well as in the oblique beams and estimate the deviation of the mean scatterer from the beam pointing direction.

2 Experimental configuration

MAARSY is a powerful tool to observe the troposphere up to the mesosphere at polar latitudes. It employs an active phased array antenna system at 53.5 MHz consisting of 433 linear polarized Yagi antennas arranged in a circular shape with a diameter of 90 m. The system reaches a half power beam width of 3.6° and yields a peak power of about 800 kW. It has pulse-to-pulse beam steering capabilities with 16 receiving channels allowing the observations of PMSE at high spatial and temporal resolutions. For further system descriptions, see Latteck et al. (2012).

The flexible setup of MAARSY can be used to assign receiving channels to different antenna sub-arrays allowing different baseline lengths and directions. The smallest subarray consists of seven antennas in the shape of a hexagon. Seven adjacent hexagons can be combined to an antenna substructure consisting of 49 single antennas called anemone. A sketch of the locations of the seven possible anemones is shown in Fig. 1 (left panel). MAARSY can be used for interferometry and imaging experiments by selecting up to 16 receiving channels out of the 55 hexagons or 7 anomenes, revealing information within the beam volume. In this experiment, MAARSY transmitted with the whole array and 7 anemones were used for reception. These seven receiving channels have been phase calibrated using radio sources as described in Chau et al. (2013).

Table 1. Experiment parameters

Parameter	Value
PRF	1250 Hz
Pulse length	1 µs
Code	16-bit complementary code
Sampling range	75–111 km
Range resolution	150 m
Data points	256
Nyquist frequency	34.72 Hz

During the PMSE season in summer 2012, MAARSY was operated in a multi-beam mode using 81 different beam directions. In this experiment, 16 azimuth angles from 0 to 360° with an azimuthal step width of 22.5° and an off-zenith step width of 5° from 0 to 25° were used. The experiment was divided into sub-experiments, each consisting of 9 beam pointing directions and including the vertical beam. During a sub-experiment, the beam pointing position was changed along a straight line on a pulse-to-pulse basis. The coherent integration time for each sub-experiment was 7.3 s and the whole sequence took 2.4 min (including sub-experiments probing the troposphere and therefore not used here). The beam pointing directions are visualized in Fig. 1 (right panel) where the red circles indicate the areas illuminated by the radar beams at about 85 km altitude. The sampling range was from 75 to 111 km with a range resolution of 150 m. Additional experiment parameters are summarized in Table 1.

3 Coherent radar imaging (CRI)

Radar systems with multiple receiver channels attached to different spatially separated antennas can be used to perform interferometric experiments. The first basic interferometric experiments were performed by Farley et al. (1981) and Kudeki et al. (1981). This was later generalized for more receivers and baselines (Kudeki and Sürücü, 1991). Since the seminal paper by Woodman (1997), the technique is called coherent radar imaging. CRI allows to process the data in a way to derive a finer angular resolution within the illuminated beam volume. Several inversion algorithms can be used, such as Capon (Palmer et al., 1998), Maximum Entropy (MaxEnt) (Hysell and Chau, 2006) or Compressed Sensing (Harding and Milla, 2013). Yu et al. (2000) showed that the results with Capon are comparable to MaxEnt in high signal-to-noise-ratio (SNR) cases, and are computational faster. However, for lower SNR, MaxEnt gives better results at the expense of significantly higher processing time. Another possible algorithm is the Fourier-based algorithm (Palmer et al., 1998), but it results in a much broader

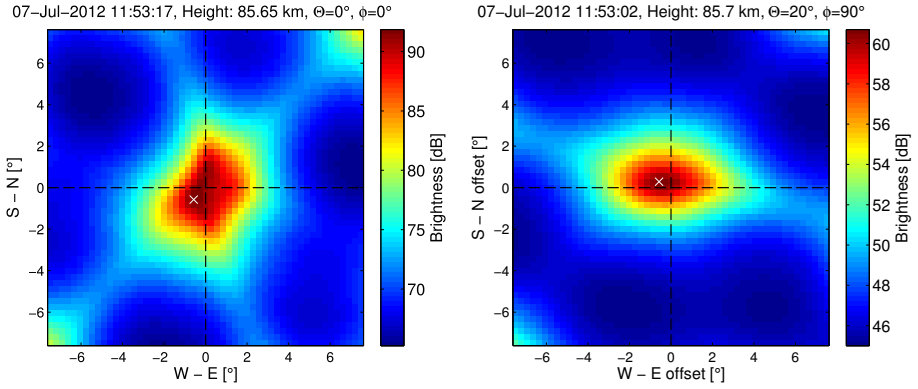

Figure 2. Brightness distribution of the zenith beam and a beam tilted 20° off-zenith and $\phi = 90°$ using Capon's method in one range gate. The color coded brightness shows a superposition of the echo and the hexagonal receiving structure due to the alignment of the sub arrays. Furthermore, aliasing due to phase ambiguity can be seen at the outer edges of figures.

brightness distributions than Capon's algorithm. In this work we present results using Capon's method.

This method makes use of visibility data R_{ij} of n spatially separated antennas i and j. The visibility data is obtained from the normalized cross-correlation estimation:

$$R_{ij}(t) = \frac{\langle v_i(t) v_j^{\star}(t) \rangle}{\sqrt{\langle |v_i(t)|^2 \rangle \langle |v_j(t)|^2 \rangle}}, \tag{1}$$

where v are the complex voltage samples, $|\ldots|$ is the absolute value of the complex data and $\langle \ldots \rangle$ denotes the time average. This can be done for all receiver pairs and R_{ij} can be arranged in a matrix, containing the visibility data

$$\mathbf{R}(t) = \begin{bmatrix} R_{11}(t) & \ldots & R_{1n}(t) \\ R_{21}(t) & \ldots & R_{2n}(t) \\ \vdots & & \vdots \\ R_{n1}(t) & \ldots & R_{nn}(t) \end{bmatrix}. \tag{2}$$

The resulting brightness distribution is

$$\mathbf{B}_c(t, \boldsymbol{k}) = \frac{1}{\boldsymbol{e}^{\dagger} \mathbf{R}^{-1} \boldsymbol{e}} \tag{3}$$

with

$$\boldsymbol{e} = \begin{bmatrix} e^{j\boldsymbol{k}\cdot\boldsymbol{D_1}} \\ e^{j\boldsymbol{k}\cdot\boldsymbol{D_2}} \\ e^{j\boldsymbol{k}\cdot\boldsymbol{D_3}} \\ \vdots \\ e^{j\boldsymbol{k}\cdot\boldsymbol{D_n}} \end{bmatrix}, \tag{4}$$

where $\boldsymbol{k}$ represents the wavenumber vector and $\boldsymbol{D}_i$ the distance vector in meters of the receiver i with respect to the origin, t is the time, $\boldsymbol{e}^{\dagger}$ denotes the conjugate transpose of $\boldsymbol{e}$, and $\mathbf{R}^{-1}$ is the inverse of the matrix $\mathbf{R}$.

Capon's algorithm does not consider the beam pattern, neither during transmission nor reception. As Capon's algorithm cannot contain a priori information, the beam weighting effects cannot be removed easily (Hysell and Chau, 2006). An example of the beam weighting effect on data is shown in Fig. 2 for the brightness in a vertical and in a 20° off-zenith beam. Due to aliasing, the pattern is repeated which can be seen at the corners of Fig. 2 (left panel). The effect of the antenna pattern of the transmitting and receiving beams are qualitatively in good agreement with the theoretical antenna pattern. Differences are attributed to the integration time used. Trying to remove the beam pattern afterwards may lead to an overestimation at the image periphery. This happens because it implies dividing by small numbers at the outer edges of the beam pattern.

However, the resulting brightness, i.e. the antenna pattern plus PMSE brightness, can be measured. From this brightness we can estimate the deviations of echo center from the beam pointing direction. For our analysis below, we selected the brightest pixel to be the mean echo center.

4 Results

To avoid the analysis of low SNR data, we set the threshold for the detection of PMSE to a SNR of 8 dB. When the signal becomes noisy outside a PMSE layer due to the cosmic background, the mean scatter location is randomly distributed. Most of the time, more than one center of brightness appear in these noisy images.

The range-time-intensity (RTI) plots of the SNR for one day using the zenith and a 25° off-zenith beam pointing northward ($\phi = 90°$) are shown in Fig. 3. PMSE occur in the altitudinal interval of 80–90 km, viz. for oblique beams, these altitudes corresponds to ranges of 88–100 km in a 25° off-zenith beam. Comparing both RTI plots, it can be seen that the PMSE layer occurs in the tilted beam (right panel) at a longer and wider range than in the zenith beam (left panel), as expected. Besides, the two layers observed around

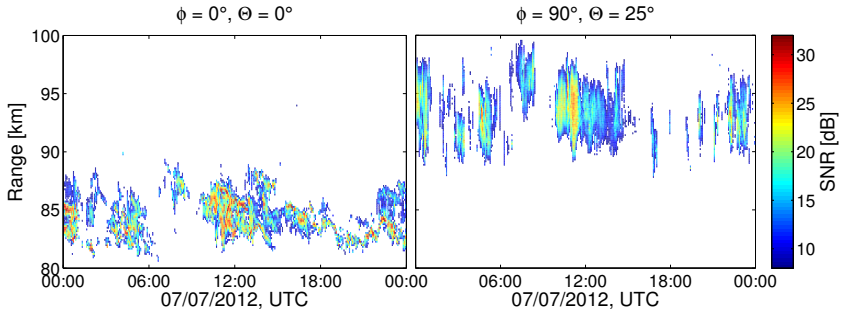

Figure 3. Range-time-intensity plot of PMSE occurring on 07 July 2012 in the zenith beam (left) and a beam tilted 25° off-zenith (right). Color coded is the SNR, whereas only a SNR greater than 8 dB is displayed. The PMSE observed by the zenith beam occur in altitudes between about 80 and 90 km, but appear at longer ranges in the tilted beam.

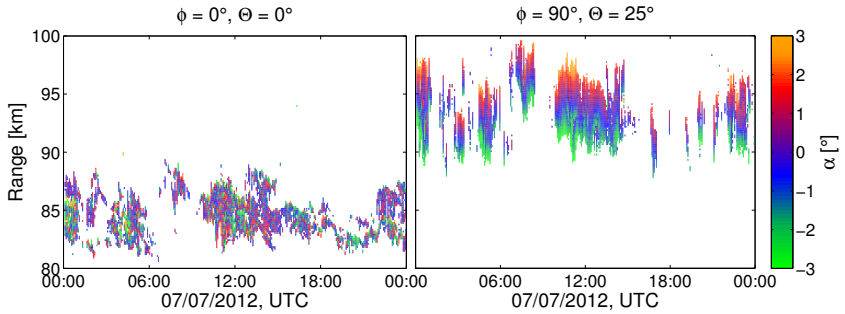

Figure 4. Deviation of the brightness peak from the beam pointing directions. Zenith (left) and 25° off-zenith (right). The echo center is determined from brightest pixel. In the tilted beam the mean center deviates significantly from the pointing directions.

12:00 UTC in the vertical beam were not detected by the tilted beams.

The brightness for each range gate and pointing direction was gridded with a meridional and zonal step width of 0.01 rad. Next, the off-zenith angles α for the brightest pixel was calculated. The results for the zenith beam and the off-zenith beam using the brightest pixel are shown for one day in Fig. 4. For a vertical beam, shown in the left panel of Fig. 4, the deviation is calculated with respect to the swivel direction. Deviations up to $\pm 3°$ occur, but no pattern with the same direction of the deviation can be identified. Therefore we do not see evidence of tilted layers during the time of our observation.

In the right panel of Fig. 4, the deviation of the mean backscatter from the nominal beam pointing angle 25° off-zenith is shown. It can be seen that deviations away from/towards the zenith (positive/negative values) occur in the upper/lower part of the PMSE layer. In between, the off-zenith angle of the mean backscatter location is almost the same as the nominal beam pointing angle. Comparing this with the SNR of the range gate, especially for the large off-zenith angles, the large deviations belong to low SNR values resulting from a low beam filling factor. Higher SNR values occur mostly in the middle of the PMSE layer, where the deviations from the nominal pointing directions are small and the beam volume appears to be homogeneously filled.

In Figs. 5 and 6 a swivel from North to South and East to West, respectively, is shown for the same date. Greater off-zenith pointing beams show deviations of echo centers from the beam directions and such deviations emerge at the outer parts of the PMSE layer. Moreover, sub-structures indicated by the deviations of echo centers appear in some beams with $\Theta \geq 10°$. More than one layer can be seen in tilted beams in contrast to the RTI plots. An example for this occurs at about 12:00 UTC in the beam pointing towards $\phi = 90°$ with $\Theta \geq 10°$. From the SNR plot in Fig. 3 (right panel), the PMSE appears to consist of one thick layer, however two layers are visible after the CRI analysis (see Fig. 5). Using CRI, the two layers observed in the vertical beam (left panel of Fig. 3) can now be observed in the tilted beams.

MAARSY's half power beam width of 3.6° corresponds to a horizontal extension of 5 km at 80 km altitude, a titled beam pointing 25° off-zenith spans a height of 2.4 km. If the beam volume is inhomogeneously filled with PMSE, the mean backscatter location shifts toward the filled part of the beam volume. Due to the larger height coverage at great off-zenith angles, the beam volume is only partly filled at the outer areas of the PMSE layer. Therefore in the upper/lower part of the PMSE layer the mean backscatter location shifts downwards/upwards, indicated by positive/negative α. The small deviations in the middle part of the PMSE region indicate that such regions are homogenously filled. No large

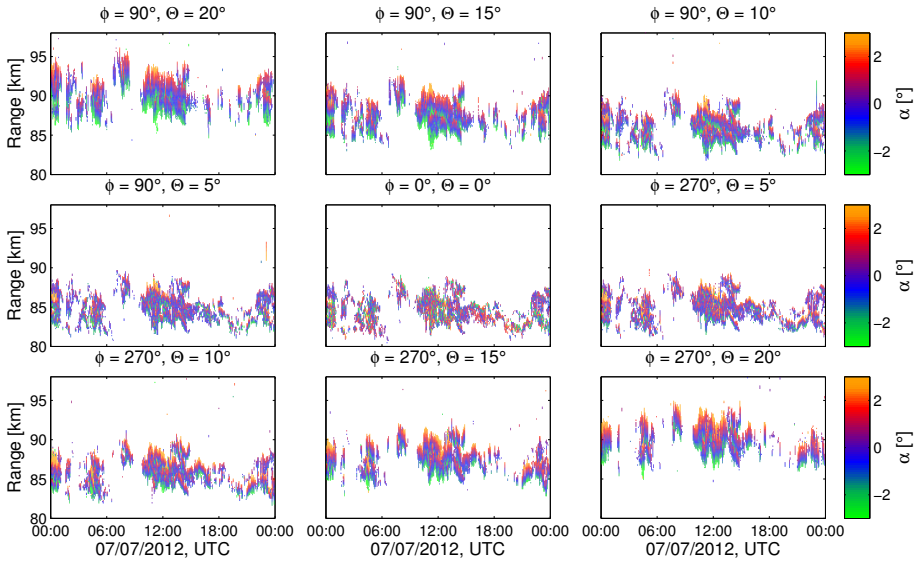

Figure 5. Similar to Fig. 4, but showing nine beams from North to South with different off-zenith angles.

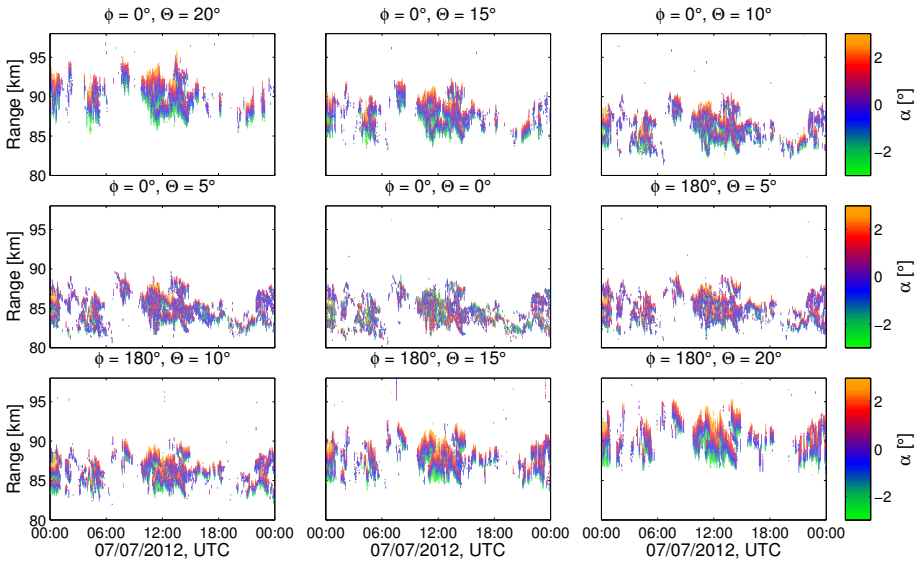

Figure 6. Same as Fig. 5, but with a scan from East to West.

deviation of the mean scatterer location from the nominal beam pointing direction.

5 Conclusions

Our PMSE observations applying CRI in tilted beams show a deviation of the mean scatter location depending on the tilt angle of the beam. To determine the mean backscatter location, we assumed a single center distribution and used the brightest pixel as a proxy of the mean backscatter location. Using tilted beams, sub-structures like small layers appear sometimes in oblique beams that cannot be seen in the SNR. This analysis might be used in the future to investigate the inner structures such as sub-layers on a higher spatial resolution.

Taking into account the smearing effect over height and also the fact, that the mean scattering center in the upper/lower part is less/greater than the beam pointing direction, we conclude that the radar volume of the tilted beam at the edge regions of PMSE is not homogenously filled. Only if the beam volume is homogenously filled, the deviation from the nominal off-zenith angle of the beam is around zero. As the beam volume is not totally filled at large off-zenith angles at the edges of the PMSE, the backscattered power is smaller compared to the vertical beam. Woodman and Chu (1989)

suggest a scattering mechanism for turbulent atmospheric layers which are discrete over height. The sharp boundaries described in their layer model are consistent with our measurements, although they investigated echoes in the lower latitudes.

So far, we can not distinguish between a homogeneous filled beam volume and several thin layers. But in some cases, our method reveals sub-layers in tilted beams which are hard to detect using only the power as an indicator.

The deviation of the mean scatterer from the beam pointing direction should also be considered in wind calculations using PMSE as a tracer as already indicated by Stober et al. (2013). Using CRI to locate the scattering center can lead to better results since we showed that significant deviations of echo centers from the beam direction occur systematically at the PMSE edges. As Huaman and Balsley (1998) pointed out, the aspect sensitivity of PMSE has also to be taken into account for measuring the wind velocities, but our results indicate that this is only true at the lower and upper regions of the PMSE. The necessary corrections are more complicated and depend on the probed part of the PMSE layer and therefore alter with altitude and time.

Acknowledgements. The authors would like to thank Marius Zecha for MAARSY data handling and the Andøya Rocket Range for the support while building and operating the MAARSY radar and an anonymous reviewer for his/her helpful comments. The radar was built under grant 01 LP 0802A of Bundesmisterium für Bildung und Forschung.

References

Blix, T. A.: Small scale plasma and charged aerosol variations and their importance for polar mesosphere summer echoes, Adv. Space Res., 24, 537–546, 1999.

Chau, J. L., Renkwitz, T., Stober, G., and Latteck, R.: MAARSY multiple receiver phase calibration using radio sources, J. Atmos. Sol.-Terr. Phy., doi:10.1016/j.jastp.2013.04.004, 2013.

Chen, J.-S. and Furumoto, J.: Measurement of atmospheric aspect sensitivity using coherent radar imaging after mitigation of radar beam weighting effect, J. Atmos. Ocean. Tech., 30, 245–259, 2013.

Chen, J.-S., Hoffmann, P., Zecha, M., and Röttger, J.: On the relationship between aspect sensitivity, wave activity, andmultiple scattering centers of mesosphere summer echoes: a case study using coherent radar imaging, Ann. Geophys., 22, 807–817, doi:10.5194/angeo-22-807-2004, 2004.

Chen, J.-S., Hoffmann, P., Zecha, M., and Hsieh, C.-H.: Coherent radar imaging of mesosphere summer echoes: Influence of radar beam pattern and tilted structures on atmospheric echo center, Radio Sci., 43, RS1002, doi:10.1029/2006RS003593, 2008.

Chilson, P. B., Yu, T.-Y., Palmer, R. D., and Kirkwood, S.: Aspect sensitivity measurements of polar mesosphere summer echoes using coherent radar imaging, Ann. Geophys., 20, 213–223, doi:10.5194/angeo-20-213-2002, 2002.

Czechowsky, P. and Rüster, R.: VHF radar observations of turbulent structures in the polar mesopause region, Ann. Geophys., 15, 1028–1036, doi:10.1007/s00585-997-1028-8, 1997.

Ecklund, W. L. and Balsley, B. B.: Long-term observations of the Arctic mesosphere with the MST radar at Poker Flat, Alaska, J. Geophys. Res.-Space, 86, 7775–7780, doi:10.1029/JA086iA09p07775, 1981.

Farley, D. T., Ierkic, H. M., and Fejer, B. G.: Radar interferometry: A new technique for studying plasma turbulence in the ionosphere, J. Geophys. Res.-Space, 86, 1467–1472, doi:10.1029/JA086iA03p01467, 1981.

Harding, B. J. and Milla, M.: Radar imaging with compressed sensing, Radio Sci., 48, 582–588, doi:10.1002/rds.20063, 2013.

Hocking, W. K., Ruster, R., and Czechowsky, P.: Absolute reflectivities and aspect sensitivities of VHF radiowave scatterers measured with the SOUSY radar, J. Atmos. Terr. Phys., 48, 131–144, 1986.

Huaman, M. M. and Balsley, B. B.: Long-term-mean aspect sensitivity of PMSE determined from Poker Flat MST radar data, Geophys. Res. Lett., 25, 947–950, 1998.

Hysell, D. L. and Chau, J. L.: Optimal aperture synthesis radar imaging, Radio Sci., 41, 1–12, doi:10.1029/2005RS003383, 2006.

Kudeki, E. and Sürücü, F.: Radar interferometric imaging of field-aligned plasma irregularities in the equatorial electrojet, Geophys. Res. Lett, 18, 41–44, doi:10.1029/GL008i004p00377, 1991.

Kudeki, E., Fejer, B., Farley, D., and Ierkic, H.: Interferometer studies of equatorial F region irregularities and drifts, Geophys. Res. Lett., 8, 377–380, doi:10.1029/0GPRLA000008000004000377000001, 1981.

Latteck, R., Singer, W., Rapp, M., Vandepeer, B., Renkwitz, T., Zecha, M., and Stober, G.: MAARSY: The new MST radar on Andøya-System description and first results, Radio Sci., 47, RS1006, doi:10.1029/2011RS004775, 2012.

Palmer, R. D., Gopalam, S., Yu, T. Y., and Fukao, S.: Coherent radar imaging using Capon's method, Radio Sci., 33, 1585–1598, 1998.

Rapp, M. and Lübken, F.-J.: Polar mesosphere summer echoes (PMSE): Review of observations and current understanding, Atmos. Chem. Phys., 4, 2601–2633, doi:10.5194/acp-4-2601-2004, 2004.

Röttger, J. and Vincent, R. A.: VHF radar studies of tropospheric velocities and irregularities using spaced antenna techniques, Geophys. Res. Lett., 5, 917–920, 1978.

Sommer, S., Stober, G., Schult, C., Zecha, M., and Latteck, R.: Investigation of horizontal structures at mesospheric altitudes using coherent radar imaging, Advances in Radio Science, 11, 319–325, doi:10.5194/ars-11-319-2013, 2013.

Stober, G., Latteck, R., Rapp, M., Singer, W., and Zecha, M.: MAARSY-The new MST radar on Andøya: First results of spaced antenna and Doppler measurements of atmospheric winds in the troposphere and mesosphere using a partial array, Advances in Radio Science, 10, 291–298, doi:10.5194/ars-10-291-2012, 2012.

Stober, G., Sommer, S., Rapp, M., and Latteck, R.: Investigation of gravity waves using horizontally resolved radial velocity measurements, Atmos. Meas. Tech., 6, 2893–2905, doi:10.5194/amt-6-2893-2013, 2013.

Sureshbabu, V. N., Anandan, V. K., Tsuda, T., Furumoto, J., and Rao, S.: Performance Analysis of Optimum Tilt Angle and Beam Configuration to Derive Horizontal Wind Velocities by Postset Beam Steering Technique, Geoscience and Remote Sensing, IEEE Transactions, 51, 520–526, doi:10.1109/TGRS.2012.2200256, 2013.

Woodman, R. F.: Coherent radar imaging: Signal processing and statistical properties, Radio Sci., 32, 2373–2391, 1997.

Woodman, R. F. and Chu, Y.-H.: Aspect sensitivity measurements of VHF backscatter made with the Chung-Li radar: Plausible mechanisms, Radio Sci., 24, 113–125, 1989.

Yu, T. Y., Palmer, R. D., and Hysell, D. L.: A simulation study of coherent radar imaging, Radio Sci., 35, 1129–1141, 2000.

Yu, T.-Y., Palmer, R. D., and Chilson, P. B.: An investigation of scattering mechanisms and dynamics on PMSE using coherent radar imaging, J. Atmos. Sol.-Terr. Phy., 63, 1797–1810, 2001.

Appendix B Sommer et al. (2016a)

Sommer, S., G. Stober, and J. L. Chau, On the angular dependence and scattering model of Polar Mesospheric Summer Echoes at VHF, *J. Geophys. Res.*, *121*, 278–288, doi:10.1002/2015JD023518, 2016.

Appendix C Sommer et al. (2016b)

Sommer, S., J. L. Chau, and C. Schult, On high time-range resolution observations of PMSE: statistical characteristics, *J. Geophys. Res.*, *121*, 6713–6722, doi:10.1002/2015JD024531, 2016.

Appendix D Sommer and Chau (2016)

Unpublished manuscript

Patches of polar mesospheric summer echoes characterized from radar imaging observations with MAARSY

Svenja Sommer[1] **and Jorge L. Chau**[1]

[1]Leibniz Institute of Atmospheric Physics at the University of Rostock, Kühlungsborn, Germany

Correspondence to: S. Sommer (sommer@iap-kborn.de)

Abstract. A recent study has hypothesized that PMSE might consist mainly of localized isotropic scattering. These results have been inferred from indirect measurements. Using radar imaging with the Middle Atmosphere Alomar Radar System (MAARSY), we observed horizontal structures that support our previous findings. We find that patches of PMSE, as observed by the radar, are usually smaller than 1 km. These patches occur throughout the illuminated volume, supporting that PMSE are caused by localized isotropic or inhomogeneous scattering. Furthermore, we show that imaging can be used to identify side lobe detections, which have a significant influence even for narrow beam observations. Improved spectra estimations are obtained by selecting the desired volume to study parameters such as spectral width and to estimate the derived energy dissipation rates. In addition, a combined wide beam experiment and radar imaging is used to resolve the radial velocity and spectral width at different volumes within the illuminated volume.

1 Introduction

Polar mesospheric summer echoes (PMSE) are nowadays a well understood phenomenon in the mesopause region where turbulence plays a major role for the existence of these echoes in conjunction with charged ice particles and free electrons (Rapp and Lübken, 2004). These echoes are commonly used as tracers for wind in polar regions in the middle atmosphere (e.g., Czechowsky et al., 1989; Stober et al., 2013) and are used to estimate the energy dissipation rate at mesospheric heights (Kelley et al., 1990).

Although these echoes are known since the late 70's, some aspects of their existence, such as their aspect sensitivity (Hocking et al., 1986; Zecha et al., 2001; Chilson et al., 2002), have been explained only recently with modern, flexible radar systems. As the contradicting preceding studies regarding aspect sensitivity came to different conclusions, Sommer et al. (2016b) hypothesized that instrumental effects have to be considered together with a localized isotropic scattering mechanism. The existence of small scale waves in the polar mesosphere is well known in noctilucent clouds (NLC) (Baumgarten and Fritts, 2014). As NLC and PMSE are closely related, small scale structures might also exist in PMSE which might be resolved using radar imaging. Röttger et al. (1990) already concluded that PMSE are unlikely to fill the observed volume homogenously at 224 MHz. If these small scale structures exist, that finding might also have impact on wind measurement techniques such as the full correlation analysis (FCA). This technique assumes a statistically homogenous scatter (Briggs, 1968; Doviak et al., 1996; Holloway et al., 1997). Here, we show that the horizontal homogeneity is not always satisfied since PMSE are either localized or not homogenous in power the beam volume, similar to NLC observations. On the other hand, the observation of PMSE on short time scales is limited by statistical effects of the scattering process. The statistical scattering properties of PMSE on short time scales were investigated by Sommer et al. (2016a), also showing the instrumental influences on PMSE measurements. In this paper, we resolve the horizontal structure of PMSE directly, and discuss the observations in relation to Sommer et al. (2016a) findings.

The observation of PMSE depends on the antenna beam pattern and hence, the transmitting and receiving antenna. Large aperture radars such as MAARSY have a strong side lobe suppression of -17 dB (Latteck et al., 2012) but PMSE can be stronger than that, and hence, they can also be detected by side lobes (Chen et al., 2008). On the other hand, wind and turbulence estimation algorithms usually assume, that the received signals come from the main beam (Hocking et al., 1986), which is not necessarily the case, especially if

PMSE are not equally distributed in the observation volume and/or they are stronger than the peak-to-side lobe level. Imaging techniques such as Capon (Palmer et al., 1998; Yu et al., 2001) or Maximum Entropy (Hysell and Chau, 2006) are capable to resolve the scatter location within the beam volume and are able to determine spectral parameters with their dependence on incident angle (Kudeki and Sürücü, 1991). This allow us to use the information: either to identify what is really coming from the main beam or to lose the side lobe information to determine neutral dynamics.

In this paper, we present studies of PMSE with radar imaging using Capon's method. First, we show that PMSE are observed as isotropic patches that are usually smaller than the beam volume and in the second part, we show how imaging can be used to identify side lobe detections and apply an synthetic narrow beam for spectral analysis and energy dissipation rate determination.

2 Experimental setup and methods

The Middle Atmosphere Alomar Radar System (MAARSY) is the only VHF (53.5 MHz) high power-large aperture (866 kW) radar in northern polar regions capable of radar imaging. Its 433 Yagi antennas, each with its own transceiver module, are combined in groups of seven in a hexagonal structure. The whole array and 15 sub-arrays (or 16 sub-arrays) can be sampled at once. To optimize the receiver configuration for radar imaging, a maximum of non-redundant baselines between all receivers is desirable. On 9 June 2015, MAARSY ran in the receiver configuration shown in Fig. 1, left side, with 145 unique baselines. The visibility of the configuration is shown on the middle panel of Fig. 1. The right panel of Fig. 1 shows the antenna beam pattern of the combined 15 sub-arrays used for reception, i.e., the instrument function. For further MAARSY description, see Latteck et al. (2012).
Our radar imaging experiment was complemented with a narrow-wide beam configuration, meaning that two beam sizes of 3.6° and 12.6° (half power full width (HPFW)) were transmitted almost simultaneously. The beam direction was vertical with a range resolution of 150 m. The experiment had an interpulse period of 2 ms for each beam. Data was recorded after 4 coherent integration, resulting in an effective time resolution of 8 ms. Continuous 32 s data blocks were recorded. Spectra estimation was done with additional 2 coherent and 4 incoherent integrations. For further experiment details and parameters of the narrow-wide beam experiment, see Sommer et al. (2016a).
For this study, the data was analyzed using Capon's method (Capon, 1969; Palmer et al., 1998), as Capon's method allows to directly access the angular resolved spectral information. The angular power distribution, called brightness B, can be achieved by weighting each receiver signal with a linear filter to minimize side lobes adaptively and therefore possible interference. The resulting weighting vector $\mathbf{w}(\mathbf{k})$ for a certain wavenumber vector $\mathbf{k} = \begin{bmatrix}\theta_x & \theta_y & \theta_z\end{bmatrix}$, where θ_i is the direction cosine in x-,y-, and z-direction, respectively, can be shown to be (Palmer et al., 1998):

$$\mathbf{w}_C = \frac{\mathbf{V}^{-1}\mathbf{e}}{\mathbf{e}^\dagger \mathbf{V}(0)^{-1}\mathbf{e}}. \tag{1}$$

$$\mathbf{V} = \begin{bmatrix} V_{11} & V_{12} & \dots & V_{1n} \\ V_{21} & V_{22} & \dots & V_{2n} \\ \vdots & & \vdots & \vdots \\ V_{n1} & V_{n2} & \dots & V_{nn} \end{bmatrix} \tag{2}$$

is the normalized cross-correlation matrix with the elements $V_{ij} = \frac{\langle S_i S_j^* \rangle}{\sqrt{\langle |S_i|^2 \rangle \langle |S_j|^2 \rangle}}$ as the normalized cross correlation between the signals S_i for receivers i and j, and

$$\mathbf{e} = \begin{bmatrix} e^{i\mathbf{k}\cdot\mathbf{D}_1} & e^{i\mathbf{k}\cdot\mathbf{D}_2} & \dots & e^{i\mathbf{k}\cdot\mathbf{D}_n} \end{bmatrix}, \tag{3}$$

where $\mathbf{D}_i$ represents the center of receiving array i.
The resulting brightness distribution is

$$B_C(\mathbf{k}) = \frac{1}{\mathbf{e}^\dagger \mathbf{V}^{-1}\mathbf{e}}. \tag{4}$$

Capon's method can be used not only for the angular power distribution but also to obtain radial velocities and spectral widths inside the beam volume, assuming quasi-stationarity during the observation period. For PMSE, we obtain the spectrum for a certain $\mathbf{k}$. Hence, we apply the weighting vector, obtained with the average of the time series, on the time series signals $\mathbf{s}$ of the n receivers:

$$y(t) = \mathbf{w_C}^\dagger \mathbf{s}(t) \tag{5}$$

The power spectral density for the parameter analysis is calculated by Fourier transforming each weighted time series for each pointing direction $\mathbf{k}$ and fitting a truncated Gaussian function, yielding in maps for the signal, Doppler velocity shift and spectral width.
The resulting radial velocities can be used to map the wind field. A simple approach such as a Doppler beam swinging (DBS) analysis could be applied, as well as more sophisticated approaches such as volume velocity processing, allowing for inhomogeneities in the wind field (Waldteufel and Corbin, 1979).

2.1 Results

The signal-to-noise ratio (SNR) obtained from the narrow-wide beam experiment on 9 June 2015 is shown in Fig. 2. The top panel of Fig. 2 shows the SNR of the narrow beam with a beam width of 3.6° HPFW. The lower panel of the same figure shows the SNR of the wide beam (12.6° HPFW) experiment. During the observation time, PMSE occurrence

was almost continuous at least in the narrow beam. Comparing the results from both beams, the main features of the stronger PMSE are observed in both beams but the SNR of the wide beam is weaker than the SNR of the narrow beam. The most important reason is the geometry of the observations: in the wide beam experiment, the power is spread over a larger solid angle, leading to less gain at zenith. If the beam is wider, more energy will be transmitted to large off-zenith angles and scattered by PMSE, but PMSE appear in larger range gates at large off-zenith angles compared to a narrow beam. Decreasing the gain at zenith decreases therefore the SNR.

Due to the decreased SNR, some PMSE cannot be detected (e.g., 07:30-08:30 UTC, 78 km - 82 km) by the wide beam but can be seen in the narrow beam. On the other hand, signal can be detected at larger ranges in the wide beam observations than in the narrow beam observations (e.g., 00:30-01:00 UTC, 88 km - 89.5 km).

The spectral parameters of the narrow beam experiment are shown in Fig. 3: (a) SNR, (b) radial Doppler velocity, (c) spectral width, (d) expected uncertainties for the Doppler velocity and (e) uncertainties for the spectral width, respectively. All the parameters are obtained from a truncated Gaussian fit like that used by Sheth et al. (2006). The red lines indicate two time intervals that are analysed later in detail with imaging. The Doppler velocity of the narrow beam varies mainly between $\pm 15\mathrm{m\,s^{-1}}$ and are quite large compared to the expected vertical wind component of only a few meters per second (Hoppe and Fritts, 1995). Particularly large values ($> 15\mathrm{m\,s^{-1}}$) can be observed around 01:00 UTC above 88 km. The spectral width is sometimes enhanced during certain periods of time, e.g., 08:30-09:00 UTC, 83 km to 85 km and 00:30-01:00 UTC, 85 km and above. The enhanced spectral width at the top of PMSE together with the increased corresponding radial velocity are likely due to echoes coming from antenna side lobes, as we show below.

2.2 PMSE patch sizes

Side lobe detection can influence the observations of PMSE and the illuminated volume cannot be assumed to be the expected main beam (e.g., Hocking et al., 1986). Hence, side lobe contributions have an influence on wind analysis methods, like DBS or FCA, but these side lobe contributions could be estimated if the antenna beam pattern is known.

The remaining problem might be, that the illuminated area is large and changes in PMSE within the observed volume can occur. Therefore, using radar imaging, we analyze the sizes of PMSE patches for different beam sizes and integration times. Such patches have been hypothesized by Sommer et al. (2016b).

Fig. 4 shows the obtained brightness (first row), radial velocity (second row) and spectral width (bottom row) for three adjunct altitudes after converting the image from angular space and range into cartesian coordinates and altitude with MAARSY at (0,0,0) for a 32 s wide beam data set. The white lines indicate fitted 2D Gaussian ellipsoids. The point in time 00:33:58 UTC is marked by the first vertcial red line in Fig. 3. The PMSE were strong at the time and the observation volume was filled with PMSE which can be seen in the brightness distribution. Although PMSE occur in the whole beam volume, the strength varies. If PMSE would homogeneously fill the beam volume, the antenna beam pattern could be seen, which is not the case. In the lowest altitude, PMSE fill almost homogeneously the beam volume while at the highest altitude displayed here, PMSE are strongest in the upper left quadrant. In order to quantify the inhomogeneity, we fitted the peaks with N 2D Gaussian ellipsoids (following Chau and Woodman (2001)) of the form

$$f(x,y) = \sum_{i=1}^{N} A_i \exp\left(- \begin{bmatrix} x-x_0 \\ y-y_0 \end{bmatrix}^{\top} \mathbf{T}_i^{\top} \Sigma_i^{-1} \mathbf{T}_i \begin{bmatrix} x-x_0 \\ y-y_0 \end{bmatrix} \right) + A_{N+1} \tag{6}$$

with

$$\Sigma_i = \begin{bmatrix} 2\sigma_x & 0 \\ 0 & 2\sigma_y \end{bmatrix} \tag{7}$$

$$\mathbf{T}_i = \begin{bmatrix} \cos\theta & \sin\theta \\ -\sin\theta & \cos\theta \end{bmatrix} \tag{8}$$

where A_i is the amplitude, x_0 and y_0 are the center coordinates, θ the anti-clockwise rotation angle and σ_x and σ_y the width along major and minor axis. The fitted ellipses are summed up and indicated by white lines. A_{N+1} is the background brightness. The number N is determined by the number of peaks above a certain threshold.

The Doppler velocity is shown in the middle row of Fig. 4. The radial velocity becomes larger with increasing distance from the origin along the wind direction. This is reasonable with a horizontal wind component, given that the projected radial velocity depends on the off-zenith angle. The increase in radial velocity is not steady, indicating wind variability within the observed area.

The spectral width is also not uniform (Fig. 4, bottom). Areas with with increased brightness show a small spectral width while areas with increased spectral width occur mostly at larger distances from zenith, leading to an apparent larger spectral width.

A second example of PMSE images is shown in Fig. 5. It is similar to Fig. 4 but at 04:29:55 UTC. In contrast to Fig. 4, PMSE are weaker and the beam volume is not completely filled. The radial velocities also indicate a horizontal wind field but show less variations as the wind field shown in Fig. 5. The spectral width maps do not show increased spectral width.

Furthermore, as in Fig. 4, the brightness distribution in Fig. 5 is neither homogeneous nor similar to the antenna beam pattern. Again, the fitted brightness peaks are indicated by white lines and several peaks can be identified at one

altitudes. Although the brightness distribution is influenced by the antenna beam pattern, the patches of brightness allow us to determine the observed patch size by radar. To compare the different observation volumes, the fitted width σ_x, σ_y and centers x_0, y_0 of all Gaussian ellipsoids are shown in Fig. 6. Although a similar approach was shown by Chilson et al. (2002) and Chen et al. (2008), our imaging configuration, i.e., longer and higher number of unique baselines than previously used, allows to detect several patches and we interpret our results as patches and not as aspect sensitivity as Chen et al. (2008) had done. Furthermore, we use different beam sizes and integration times given that Sommer et al. (2016b) showed that longer integration times lead to a more homogeneously filled beam volume. The width is shown in the first row for x (left) and y (right) and the count number for each bin is normalized to the total count number. Color coded are the different beam sizes and integration times. Yellow indicates the 3.6° narrow beam with 32 s integration time. The 12.6° wide beam is shown in blue for 32 s and in red for 30 min integration time. The two black vertical lines indicate the 3 dB beam sizes at 85 km for the narrow (2.2 km) and wide beam (7.4 km), respectively. The bottom row shows the center locations in x- and y-direction.

The patch sizes of the 32 s narrow and wide beams are rather similar with the peak of the size distribution under 2 km and therefore smaller than the narrow main beam in x- as well y-direction. The wide beam patch distribution shows a shift to slightly larger values than the narrow beam patch distribution in both directions. This is probably due to the antenna beam pattern influence. The 30 min wide beam distribution does not show a distinct peak, but a rather wide distribution of patch sizes. This wider distribution might result from a non-homogeneous antenna beam pattern. The second row shows the center locations. All distributions are almost centered around the zenith but show different widths. The 32 s narrow beam center distributions in x- and y-direction have the smallest width as the center location is limited by the antenna beam pattern. The 32 s wide beam center distributions have the broadest width, as patches of PMSE can occur in a larger beam volume and hence, the spread is larger than in the narrow beam center distribution. On the other hand, the 30 min wide beam center distributions are narrower than the 32 s distribution. With longer integration time, the antenna beam pattern should become more dominant and reduces the patchiness of PMSE, resulting in a more centered distribution for the narrow beam.

2.3 Enhanced spectral width

The distinction between main beam and side lobe detection is crucial. Even with a strong side lobe attenuation of -17 dB of the first side lobe for its standard narrow beam, MAARSY is able to receive signals from the side lobes when strong PMSE occur. Therefore, we show a way to identify the side lobe signals and therefore improve the estimates of radial velocity and spectral width.

To identify main beam and side lobe detections, we apply radar imaging as described above, resulting in a spectrum for each virtual beam pointing direction $\mathbf{k}$. Each spectrum was analyzed regarding Doppler velocity and spectral width.

In order to avoid large angle contributions, we use imaging and compare the results to the standard narrow beam, for which we assume that all echoes come from the main beam. We imaged the spectra for certain area only, namely between -1.8° and 1.8°, hereafter called synthetic narrow beam. This area corresponds to the HPFW main beam of MAARSY. Fig. 7 shows RTIs of the SNR and spectral width for the standard narrow beam (left column) and the synthetic narrow beam (right column). It can be seen that the spectral width of the standard narrow beam shows sometimes an increase at the upper edge of PMSE. These features vanishes when the spectrum is only obtained from the synthesized narrow beam. This can be clearly seen around 01:00 UTC above 85 km. However, there are periods with increased spectral width in the synthetic narrow beam, possibly related to increased turbulence, e.g., around 08:00 UTC.

We used the approach of Hocking (1985) to estimate the turbulence strength in a simple approach by neglecting shear and wave broadening (Murphy et al., 1994; Nastrom and Eaton, 1997). We estimated the horizontal wind velocity using the derived radial velocity maps presented above using a DBS approach. The resulting wind magnitude of the horizontal wind is presented in Fig. 8, top. Throughout the observation period, increased periods of wind can be detected, leading to an increased spectral width due to beam broadening. Following Hocking (1985), the turbulence strength ϵ can be derived from the half power half width of the spectrum by

$$f_{turb}^2 = f_{obs}^2 - f_{bb}^2, \tag{9}$$

where f_{turb} is the increase in spectral width due to turbulence, f_{obs} is the measured half power half width of the spectrum and $f_{bb} = \frac{2}{\lambda} f_{3\text{dB}} V$ the increase in spectral width due to a horizontal wind V (i.e., so called beam broadening effect), calculated by using the 3 dB half power half width beam size. The two-way beam width for the narrow beam of MAARSY is $f_{3\text{dB}} = 1.3°$. Theoretically, the two-way beam width for the narrow beam, and therefore the beam broadening effect, would increase if the side lobe contributions are significant. We calculated $f_{3\text{dB}} = 0.95°$ for the synthetic narrow beam with the second moment and assuming the standard narrow beam shape, but which is zero outside the MAARSY main beam(i.e., $> 1.8°$).

The mean square fluctuation velocity v_{rms}^2 is given by

$$v_{rms}^2 = \frac{\lambda^2}{4} \frac{f_{turb}^2}{2 \ln 2} \tag{10}$$

yielding for ϵ:

$$\epsilon = CNv_{rms}^2 \tag{11}$$

where C is a numerical constant and N the Brunt-Väisälä-frequency. Here, we use typical values for the polar mesosphere, i.e., $C = 0.47$ and $N = 0.0134\,\mathrm{rad\,s^{-1}}$ (Gibson-Wilde et al., 2000). The results for ϵ are presented in Fig. 8, middle, for the standard narrow beam, including side lobe contributions, and in bottom panel for the synthetic narrow beam after removing the side lobe contributions. The observed spectral widths for the standard narrow beam are usually larger than for the synthetic narrow beam and, hence, the energy dissipation rates for the synthetic narrow beam are smaller. The turbulence strength varies in both, the narrow beam with side lobe contribution and the synthetic narrow beam without side lobe contribution, with increased turbulence strength at some parts of PMSE, especially around 00:00-01:00, 03:00-07:00 for some parts and 08:30-09:00, with $\epsilon > 500\,\mathrm{mW\,kg^{-1}}$. Identifying the side lobes leads to a decrease in energy dissipation rate. This can be seen in Fig. 9, where the energy dissipation rate is plotted as a 2D histogram (upper left panel), especially for small ϵ, where the 2D correlation deviates from the line of equality. The upper right and lower panel shows the cumulative histograms in blue for the synthetic narrow and red for the standard narrow beam. For better comparison, the other histogram is shown with a dashed line. For low energy dissipation rates, comparing the standard narrow beam and the synthetic narrow beam, a shift towards lower energy dissipations rates can be seen here also. That means, that correcting for side lobe contribution affects mainly low turbulence cases.

2.3.1 Discussion

The horizontal variation on larger scales have been investigated by multi-beam experiments (Latteck et al., 2012; Stober et al., 2013). They showed that PMSE can vary within observation volumes of 80 km diameter by 40 dB in SNR. Multi-beam experiments take time and the resolution is limited by the beam size. Röttger et al. (1990) concluded from spectral observations, that PMSE at 224 MHz must be smaller than their observation volume, i.e., 1 km in vertical and horizontal extend. To investigate the horizontal structure of PMSE further and quantify the localized scattering, we applied Capon's method of imaging. As shown in the results section above, PMSE vary in altitude, horizontal location and extend. Sometimes, the beam volume is filled completely with PMSE, but the angular power distribution is not homogeneous (Fig. 4). In other cases, PMSE appear in patches that are asymmetric and can be smaller than 1 km. Even with the narrow beam experiment with a beam width of 3.6°, the brightness distribution within the observation volume is not homogeneously. It can be seen in Fig. 6, that the narrow and wide beam patches for 32 s integration time are in the same order of magnitude, although one would expect that the antenna beam pattern would have a major influence. This might be due to the receiving antenna pattern, which is limited by the receiver configuration (compare to Fig. 1). Furthermore, a the center location of, especially for the wide beam patches, is slightly shifted towards negative y_0. This is probably due to a small phase calibration offset but the main features of PMSE a preserved.

The hypothesis that PMSE are non-homogenous and sometimes localized are already stated in Röttger et al. (1990) at 224 MHz or Sommer et al. (2016b) at 53.5 MHz but without imaging. Here, we can support that statement and furthermore, also show that PMSE composed of localized structures of few kilometers. If PMSE would be highly aspect sensitive, imaging of wide beam experiments would show an increased brightness around zenith and almost no scatter at larger off-zenith angles. In our images, we do not see this, the images are only weighted by the antenna gain and therefore the scattering process should be isotropic. This is similar to Chen et al. (2008) who studied mesospheric echoes using imaging with the OSWIN radar and find also sometimes several backscatter locations. They interpreted their results as several reflection points from wave structures and not as isotropic scattering. Still, the structure of the isotropic scattering can be influenced by gravity waves as suggested by Chen et al. (2008) for the reflection type of scattering.

The inhomogeneous structure is due to the nature of PMSE. As Rapp and Lübken (2004) pointed out, three major components must be present for PMSE to exist: negatively charged ice particles, free electrons and turbulence. Baumgarten and Fritts (2014, Fig. 2) showed on NLC observations, that ice particles in mesospheric altitudes also show wave structures with small wave lengths (< 20 km) when ice particles are moved to different altitudes. Hence, it is not surprising that PMSE, bound to the existence of these ice particles, display also wave structures on the small scale.

Additionally to the patchy structure, we observe enhanced brightness within the observation volume, when PMSE fill the complete beam volume. This might be caused by localized enhanced turbulence or electron density but needs further investigation.

The non-homogenous PMSE distribution in space have effects on measurement techniques for wind and/ or turbulence estimations such as DBS or FCA. FCA is as an in-beam estimation method especially influenced by small scale wave activity, as the ground diffraction pattern is used to determine atmospheric parameters. Usually, the derivation required a statistically homogenous scatter distribution with a vertical anisotropy (Doviak et al., 1996) or additionally anisotropy in x- and y-direction (Holloway et al., 1997). Additional to the anisotropy of the scattering mechanism, the scatter itself might not be statistically homogeneously distributed in the observation volume. This might be due to localized enhancements, patches or waves. Usually, the sampling time

used for FCA is about 30 s as used in the results presented here. We showed that on these time scales, the distribution of PMSE in the beam volume is not homogenous. The non-homogeneity leads to an increased correlation compared to a statistically homogeneous scattering process and was previously interpreted as aspect sensitivity. Sommer et al. (2016b) compared aspect sensitivity values obtained from multiple beam experiments to values obtained by a spatial correlation analysis and concluded, that the DBS method requires long integration time for aspect sensitivity measurements and that the enhanced correlation values on short time scales are due to localized scattering mechanisms. Here, we can support this hypothesis by showing the non-homogeneity of PMSE on the 30 s time scale in the observation volume.

To study PMSE with different radar systems, the volume reflectivity is commonly used (Hocking, 1985; Li et al., 2010; Smirnova et al., 2011; Latteck and Bremer, 2013). The assumption is, that the scattering mechanism is isotropic and also homogeneous. We have shown above, that on short time scales the assumption of a homogeneous scattering process is not necessary given, resulting in a smaller volume reflectivity factor. This can be solved by calculating a beam filling factor for the volume reflectivity, or, following the approach of Sommer et al. (2016b), to use long integration periods. Latteck and Bremer (2013) used integration times of 5 min, which smoothes the localized signals and is already 10 times longer than the data sets presented here, while even longer integration periods would be more favorable.

In the second part of the discussion, we discuss radar imaging to remove side lobe detections. MST radars like MAARSY are used to study atmospheric parameters such as radial velocities for wind estimations and spectral width for turbulence estimations. Sensitive radar systems have a good side lobe suppression (e.g., MAARSY -17 dB one way, Latteck et al. (2012)). The suppression of MAARSY is better than older systems like ALWIN (Alomar wind radar) (-13 dB one way, Latteck et al. (1999)), but MAARSY still receives significant backscatter from the side lobes. If these side lobe detections are not separated from the main beam detections, the results are compromised. In this paper, we showed that with the help of imaging, side lobe detections of PMSE could be reduced significantly. The cleaned spectrum, only for the main beam, can now be analyzed regarding the spectral parameters. As shown above, the side lobe detections have a major influence on the spectral width and therefore on turbulence estimations. On the other hand, we can use the information from the side lobes with imaging to resolve the the spectral width and Doppler velocity in space as shown in Sec. 2.2.

Although many PMSE with apparent large spectral width could be identified as side lobe contributions, sometimes the spectral width of the remaining PMSE is enhanced, indicating increased turbulence or beam broadening due to increased horizontal winds or other effects (Hocking, 1985). We estimated the turbulence strength from an synthetic narrow beam of 3.6° with imaging as well as the standard narrow beam. Different derived turbulence strengths in PMSE can be identified. The derived turbulence strength ϵ is especially in the lower part of PMSE rather small with $\epsilon \sim 10\,\mathrm{mW\,kg^{-1}}$. This is in the order of expected values of turbulence in the mesopause region. Rapp and Lübken (2004) expected $\epsilon = 5\,\mathrm{mW\,kg^{-1}}$, while Gibson-Wilde et al. (2000) simulated values up to $\epsilon = 150\,\mathrm{mW\,kg^{-1}}$ using a direct numerical simulation. Li et al. (2010) found energy dissipation rates using the European Incoherent Scatter Svalbard Radar at 500 MHz (Bragg wavelength 30 cm) of $\epsilon = 5\,\mathrm{mW\,kg^{-1}} - 200\,\mathrm{mW\,kg^{-1}}$. Our observations agree also well with in-situ measurements. Sounding rocket flights conducted by Lübken et al. (2002) measured values between $\epsilon = 0\,\mathrm{mW\,kg^{-1}}$ and $\epsilon \sim 2400\,\mathrm{mW\,kg^{-1}}$ in the mesosphere. The mean value, where PMSE and turbulence coincided in the flights was $\epsilon = 390\,\mathrm{mW\,kg^{-1}}$ with a rather large standard deviation of $190\,\mathrm{mW\,kg^{-1}}$.

We also found strong turbulent events within PMSE, even after removing side lobe contribution and beam broadening. Strong turbulent events showed $\epsilon > 500\,\mathrm{mW\,kg^{-1}}$, which exceeds the expected theoretical values, but still agrees with the sounding rocket measurements of Lübken et al. (2002). Furthermore, we showed that the corrections made in this paper are affecting the majority of low turbulence cases. For high turbulence values, the synthetic narrow beam and the standard narrow beam values correlate well.

In this calculation, we neglected shear broadening as the range resolution is high and the shear contribution probably small compared to the other effects (Strelnikova and Rapp, 2011). We neglected also wave broadening, which would allow for high frequency gravity waves. Still, the observed spectral width should exceed the contribution of shear and wave broadening and is therefore an indicator for strong turbulence. The analysis presented here should be expanded in future to include shear and beam broadening effects which might have a significant contribution in weak turbulence measurements.

3 Conclusions

In this paper, we showed that PMSE appears sometimes in patches smaller than even 1 km and during other times comparable in size to the observed volume (~ 20 km) using radar imaging. Large patches of PMSE can be observed on some occasions, but also PMSE occur in large patches, but these patches are not homogenous. These inhomogeneities can be explained by an isotropic scattering mechanism that is probably influenced by the background dynamics, creating the patchiness. Long integration periods could be used to smooth out the patchy nature of PMSE for experiments that do not require a high temporal resolution. The patchy structure of PMSE might be misinterpreted as aspect sensitivity, which

should be considered in future investigations of PMSE.

Furthermore, we showed that radar imaging can be used to identify side lobe contributions in spectral width, that occur even in modern radar systems like MAARSY. The method presented here can be used to improve turbulence measurements with MST radars. We found that the correction is significant most of the time in the analyzed data. Events characterized by high spectral width show similar turbulence values before and after the beam broadening corrections.

Acknowledgements. The authors thank the MAARSY team, especially Ralph Latteck for his support during the imaging campaign, Toralf Renkwitz for providing the wide beam phases and also Bjørn Gustavsson from University of Tromsø for his help choosing the imaging configuration. We also thank Gunter Stober for providing the spectral fit algorithm used in the imaging analysis. S. Sommer was supported by ILWAO.

References

Baumgarten, G. and Fritts, D. C.: Quantifying Kelvin-Helmholtz instability dynamics observed in noctilucent clouds: 1. Methods and observations, J. Geophys. Res., 119, 9324–9337, doi:10.1002/2014JD021832, 2014.

Briggs, B. H.: On the analysis of moving patterns in geophysics– I. Correlation analysis, J. Atmos. Terr. Phys., 30, 1777–1788, 1968.

Capon, J.: High-Resolution Frequency-Wavenumber Spectrum Analysis, Proc. IEEE, 57, 1408–1418, 1969.

Chau, J. L. and Woodman, R. F.: Three-dimensional coherent radar imaging at Jicamarca : comparison of different inversion techniques, J. Atmos. Sol. Terr. Phys., 63, 253–261, 2001.

Chen, J.-S., Hoffmann, P., Zecha, M., and Hsieh, C.-H.: Coherent radar imaging of mesosphere summer echoes: Influence of radar beam pattern and tilted structures on atmospheric echo center, Radio Sci., 43, RS1002, doi:10.1029/2006RS003593, 2008.

Chilson, P. B., Yu, T.-Y., Palmer, R. D., and Kirkwood, S.: Aspect sensitivity measurements of polar mesosphere summer echoes using coherent radar imaging, Ann. Geophys., 20, 213–223, 2002.

Czechowsky, P., Reid, I. M., Rüster, R., and Schmidt, G.: VHF Radar Echoes Observed in the Siummer and Winter Polar Mesosphere Over Andøya, Norway, J. Geophys. Res., 94, 5199–5217, 1989.

Doviak, R. J., Lataitis, R. J., and Holloway, C. L.: Cross correlations and cross spectra for spaced antenna wind profilers: 1. Theoretical analysis, Radio Sci., 31, 157–180, 1996.

Gibson-Wilde, D., Werne, J., Fritts, D., and Hill, R.: Direct numerical simulation of VHF radar measurements of turbulence in the mesosphere, Radio Sci., 35, 783–798, doi:10.1029/1999RS002269, 2000.

Hocking, W. K.: Measurement of turbulent energy dissipation rates in the middle atmosphere by radar techniques: A review, Radio Sci., 20, 1403–1422, 1985.

Hocking, W. K., Ruster, R., and Czechowsky, P.: Absolute reflectivities and aspect sensitivities of VHF radiowave scatterers measured with the SOUSY radar, J. Atmos. Terr. Phys., 48, 131–144, 1986.

Holloway, Christopher L., Doviak, R. J., and Cohn, S. A.: Cross correlations of fields scattered by horizontally anisotropic refractive index irregularities, Radio Sci., 32, 1911–1920, doi:10.1029/97RS00715, 1997.

Hoppe, U.-P. and Fritts, D. C.: High-resolution measurements of vertical velocity with the European incoherent scatter VHF radar 1. Motion field characteristics and measurement biases, J. Geophys. Res., 100, 16 813–16 825, 1995.

Hysell, D. L. and Chau, J. L.: Optimal aperture synthesis radar imaging, Radio Sci., 41, 1–12, doi:10.1029/2005RS003383, 2006.

Kelley, M., Ulwick, J., Röttger, J., Inhester, B., Hall, T., and Blix, T.: Intense turbulence in the polar mesosphere: rocket and radar measurements, J. Atmos. Terr. Phys., 52, 875–891, doi:10.1016/0021-9169(90)90022-F, 1990.

Kudeki, E. and Sürücü, F.: Radar interferometric imaging of field-aligned plasma irregularities in the equatorial electrojet, Geophys. Res. Lett, 18(1), 41–44, doi:doi:10.1029/90GL02603, 1991.

Latteck, R. and Bremer, J.: Long-term changes of polar mesosphere summer echoes at 69°N, J. Geophys. Res., 118, 10,441–10,448, doi:10.1002/jgrd.50787, 2013.

Latteck, R., Singer, W., and Bardey, H.: The ALWIN MST Radar: Technical Design and Performance, European Rocket and Balloon Programs and Related Research, Proceedings of the 14th ESA Symposium held 31 May-3 June, 1999 in Potsdam. Edited by B. Schürmann. European Space Agency, ESA-SP., 437, 179–184, 1999.

Latteck, R., Singer, W., Rapp, M., Vandepeer, B., Renkwitz, T., Zecha, M., and Stober, G.: MAARSY: The new MST radar on Andøya-System description and first results, Radio Sci., 47, RS1006, doi:10.1029/2011RS004775, 2012.

Li, Q., Rapp, M., Röttger, J., Latteck, R., Zecha, M., Strelnikova, I., Baumgarten, G., Hervig, M., Hall, C., and Tsutsumi, M.: Microphysical parameters of mesospheric ice clouds derived from calibrated observations of polar mesosphere summer echoes at Bragg wavelengths of 2.8 m and 30 cm, J. Geophys. Res., 115, doi:10.1029/2009JD012271, 2010.

Lübken, F.-J., Rapp, M., and Hoffmann, P.: Neutral air turbulence and temperatures in the vicinity of polar mesosphere summer echoes, J. Geophys. Res., 107, 4273, doi:10.1029/2001JD000915, 2002.

Murphy, D., Hocking, W., and Fritts, D.: An assessment of the effect of gravity waves on the width of radar Doppler spectra, Journal of Atmospheric and Terrestrial Physics, 56, 17–29, doi:http://dx.doi.org/10.1016/0021-9169(94)90172-4, http://www.sciencedirect.com/science/article/pii/0021916994901724, 1994.

Nastrom, G. D. and Eaton, F. D.: Turbulence eddy dissipation rates from radar observations at 5-20 km at White Sands Missile Range, New Mexico, J. Geophys. Res., 102, 19 495–19 505, 1997.

Palmer, R. D., Gopalam, S., Yu, T. Y., and Fukao, S.: Coherent radar imaging using Capon's method, Radio Sci., 33, 1585–1598, 1998.

Rapp, M. and Lübken, F.-J.: Polar mesosphere summer echoes (PMSE): review of observations and current understanding, Atmos. Chem. Phys., 4, 2601–2633, 2004.

Röttger, J., Rietveld, M. T., La Hoz, C., Hall, T., Kelley, M. C., and Swartz, W. E.: Polar mesosphere summer echoes observed with the EISCAT 933-MHz radar and the CUPRI 46.9-MHz radar, their similarity to 224-MHz radar echoes, and their relation to turbulence and electron density profiles, Radio Sci., 25, 671–687, doi:10.1029/RS025i004p00671, 1990.

Sheth, R., Kudeki, E., Lehmacher, G., Sarango, M., Woodman, R., Chau, J., Guo, L., , and Reyes, P.: A high-resolution study of mesospheric fine structure with the Jicamarca MST radar, Ann. Geophys., 24, 1281–1293, 2006.

Smirnova, M., Belova, E., and Kirkwood, S.: Polar mesosphere summer echo strength in relation to solar variability and geomagnetic activity during 1997-2009, Annales Geophysicae, 29, 563–572, doi:10.5194/angeo-29-563-2011, 2011.

Sommer, S., Chau, J. L., and Schult, C.: On high time-range resolution observations of PMSE: statistical characteristics, J. Geophys. Res., accepted, 2016a.

Sommer, S., Stober, G., and Chau, J. L.: On the angular dependence and scattering model of Polar Mesospheric Summer Echoes at VHF, J. Geophys. Res., 121, 278–288, doi:10.1002/2015JD023518, 2016b.

Stober, G., Sommer, S., Rapp, M., and Latteck, R.: Investigation of gravity waves using horizontally resolved radial velocity measurements, Atmos. Meas. Tech., 6, 2893–2905, doi:10.5194/amt-6-2893-2013, 2013.

Strelnikova, I. and Rapp, M.: Majority of PMSE spectral width at UHF and VHF are compatible with a single scattering mechanism, J. Atmos. Sol. Terr. Phys., 73, 2142–2152, 2011.

Waldteufel, P. and Corbin, H.: On the analysis of single Doppler data, J. Appl. Meteorol., 18, 53–542, 1979.

Yu, T.-Y., Palmer, R. D., and Chilson, P. B.: An investigation of scattering mechanisms and dynamics on PMSE using coherent radar imaging, J. Atmos. Sol. Terr. Phys., 63, 1797–1810, 2001.

Zecha, M., Röttger, J., Singer, W., Hoffmann, P., and Keuer, D.: Scattering properties of PMSE irregularities and refinement of velocity estimates, J. Atmos. Sol. Terr. Phys., 63, 201–214, 2001.

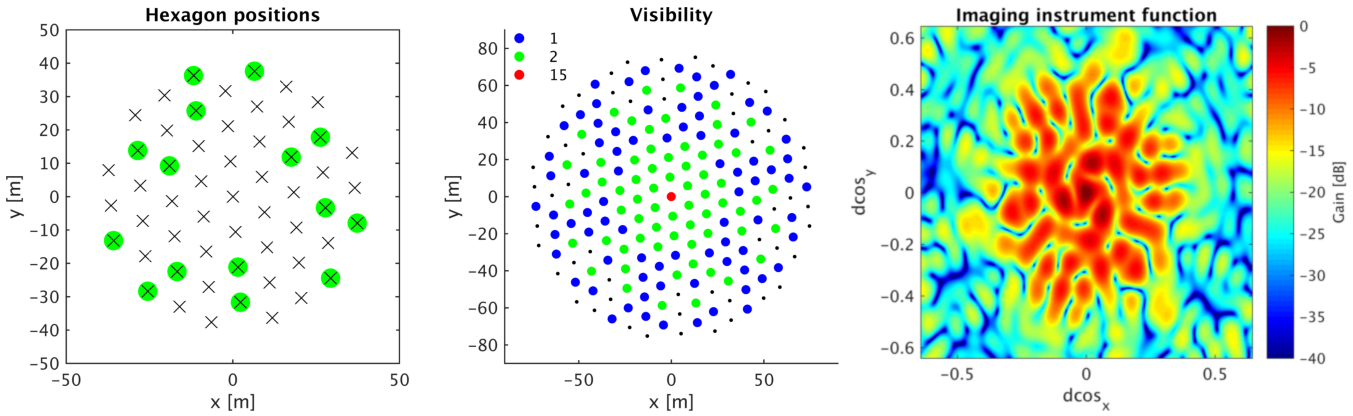

Figure 1. Left: The receiving configuration of the imaging configuration in June 2015 is indicated by green circles. All possible receiving locations are indicated by black crosses. Middle: Visibility function for the imaging configuration. All possible baselines are indicated by black dots and color coded is the number of redundant baselines of the configuration used for imaging. Right: Instrument function of the 15 hexagons indicated in the left panel.

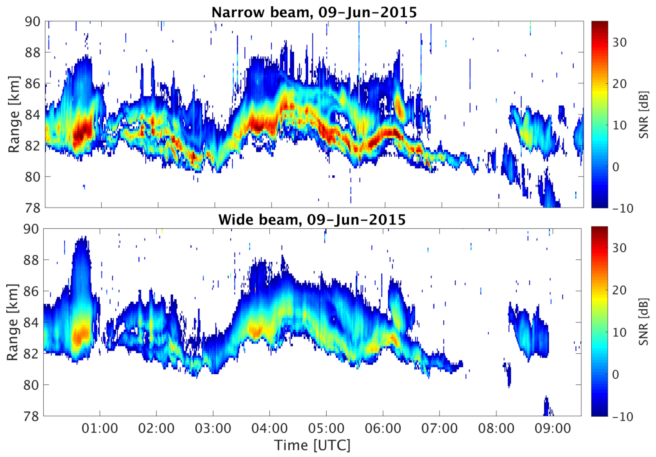

Figure 2. RTI of the SNR from (top) narrow (3.6°) and (bottom) wide (12.6°) beam of the nested beam experiment on 9 June 2015.

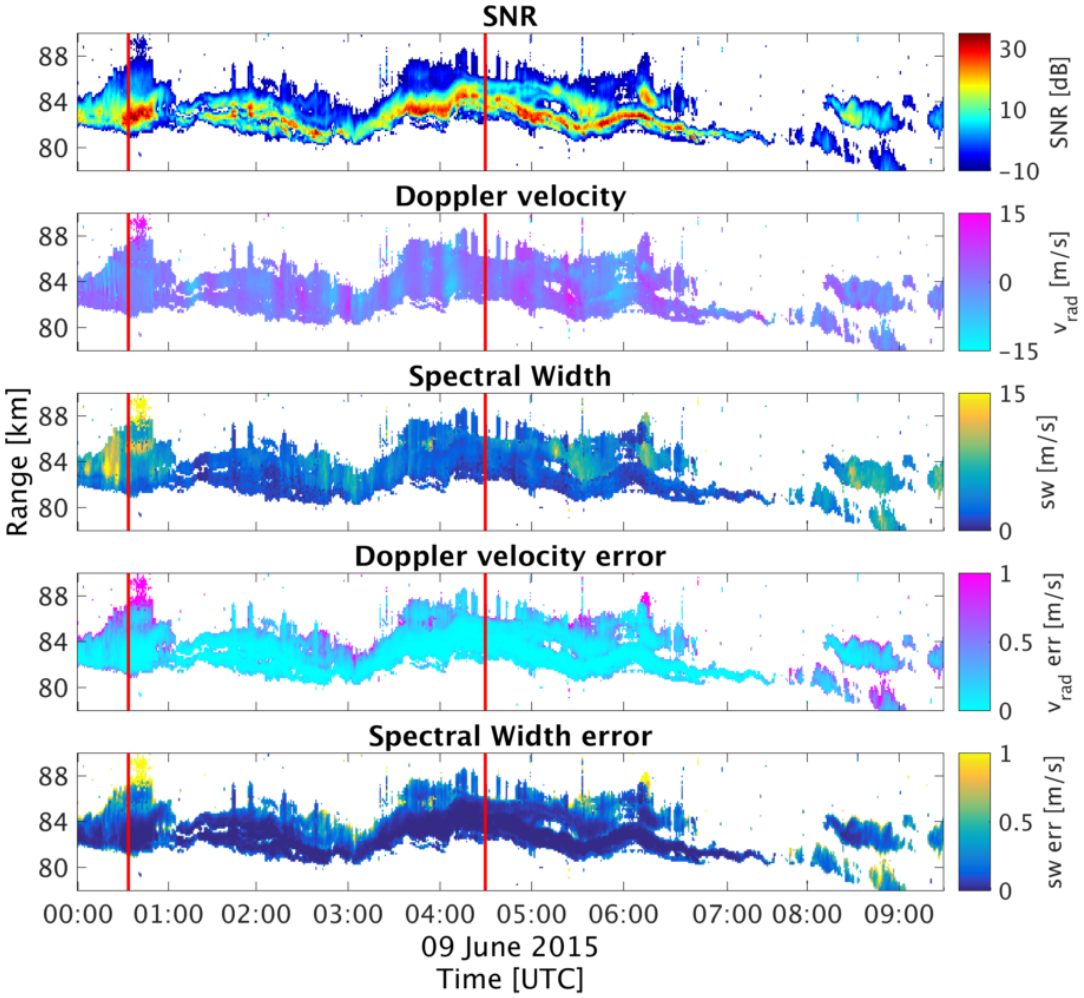

Figure 3. Analyzed parameters of the narrow beam (3.6°). a) SNR: The PMSE was strong during the observation time but got weaker in the last two hours. b): Doppler velocity: The radial velocity varies between $\pm 15 \mathrm{m\,s^{-1}}$. c): The spectral width appears to be increased sometimes at the top of PMSE (00:00-01:00 UTC) or in the whole PMSE (08:00-09:00 UTC). d) Doppler velocity error: Error of the radial velocity estimation from the Gaussian fit. e): Spectral width error: Error of the width estimation from the Gaussian fit.

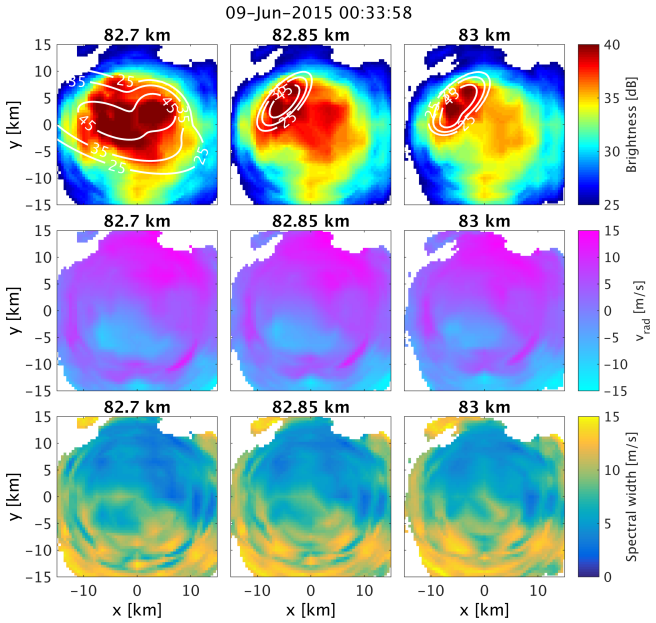

Figure 4. Spectral parameters of PMSE after converting the image to cartesian coordinates and altitude at 9 June 2015 00:33:58 UTC. The columns show three adjunct altitudes around the strongest PMSE altitude of 82.85 km. The brightness distributions are shown in the top row and are color coded. The withe lines indicated the fitted Gaussian ellipsoids. The middle row shows the radial velocities, indicating a horizontal wind and the bottom row shows the imaged spectral width.

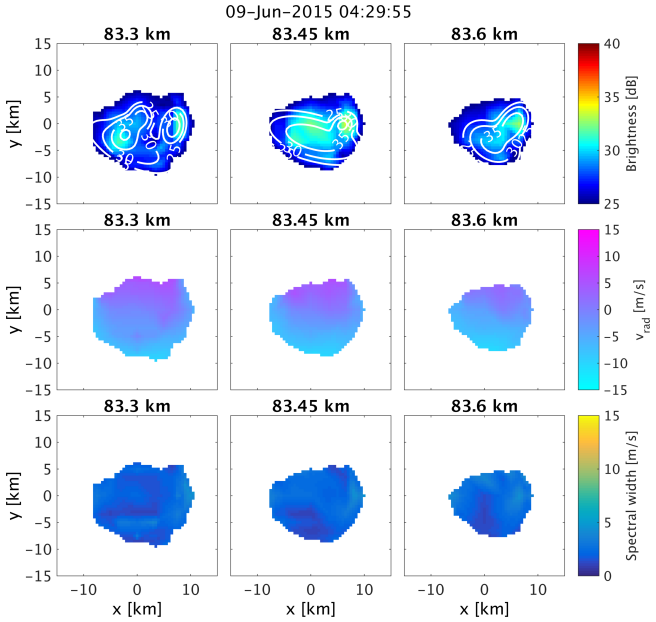

Figure 5. Same as Fig. 4, but for 04:29:55 UTC and around 83.45 km.

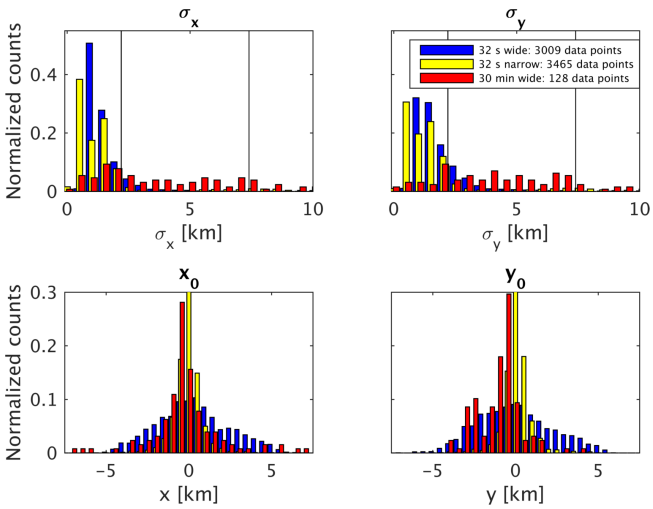

Figure 6. Histograms of the widths in x- and y-direction (top row) and center locations (bottom row). For each figure, 3 histograms are shown. Blue: 32 s narrow beam, yellow: 32 s wide beam, red: 32 min wide beam.

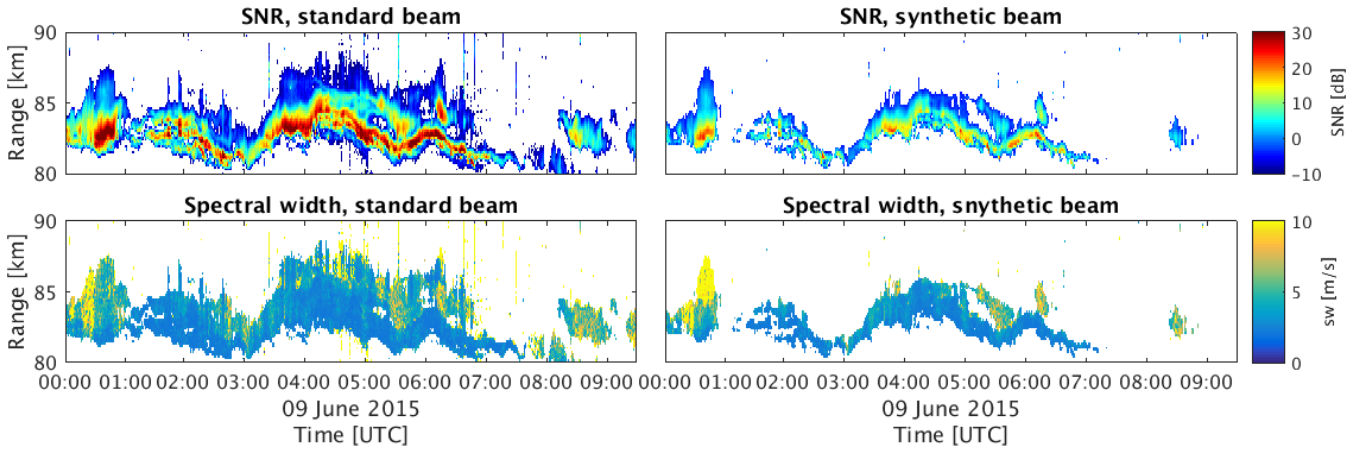

Figure 7. Comparison of spectral parameters obtained from the standard narrow beam, including side lobes (left column), and the synthetic narrow beam (right column). Comparing the SNR (first row), the echoes from the upper edges of PMSE are removed in the main beam while the lower edges are in the same range. Signals with large spectral width (second row) due to side lobe detections are removed from the beam and increased spectral width to turbulence remains.

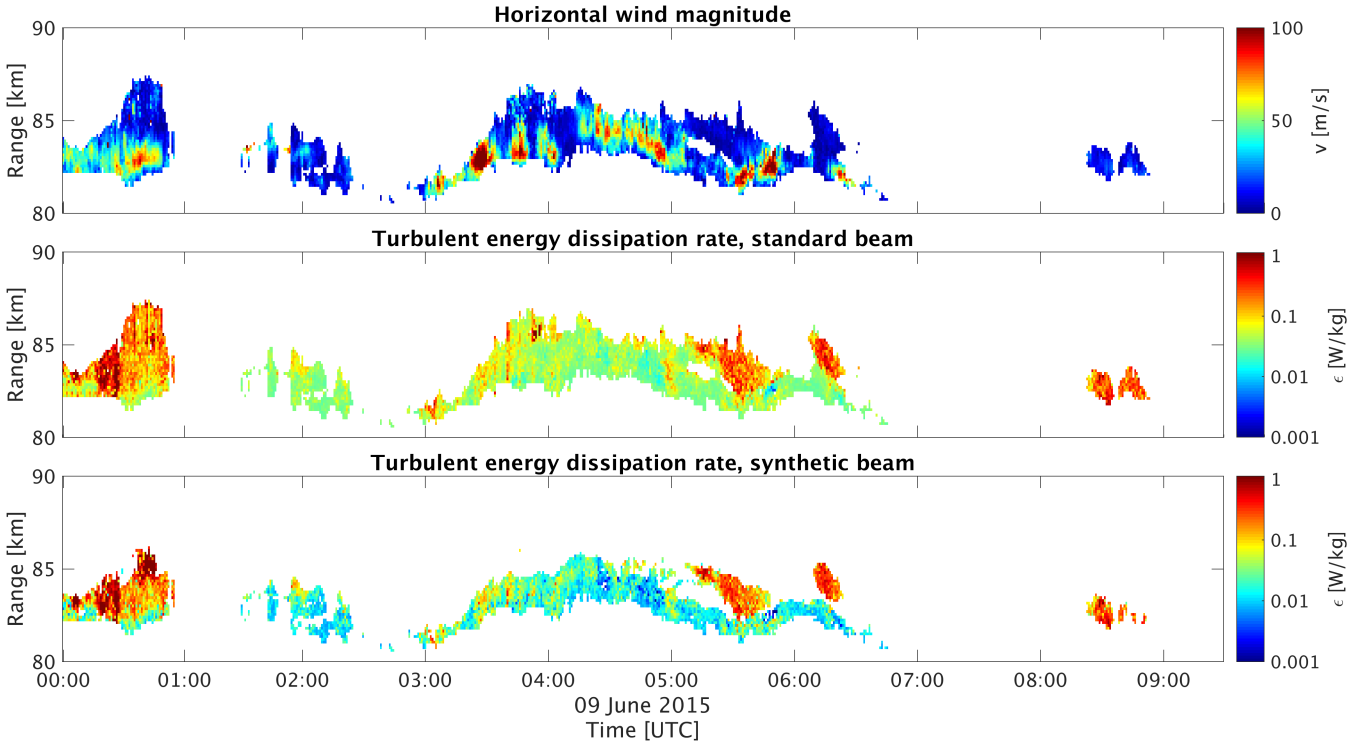

Figure 8. Top: Magnitude of the horizontal wind velocity derived by DBS from Doppler velocity maps. Middle: Derived energy dissipation rate for the standard narrow beam. Bottom: Derived turbulent energy dissipation rate for a synthetic narrow beam.

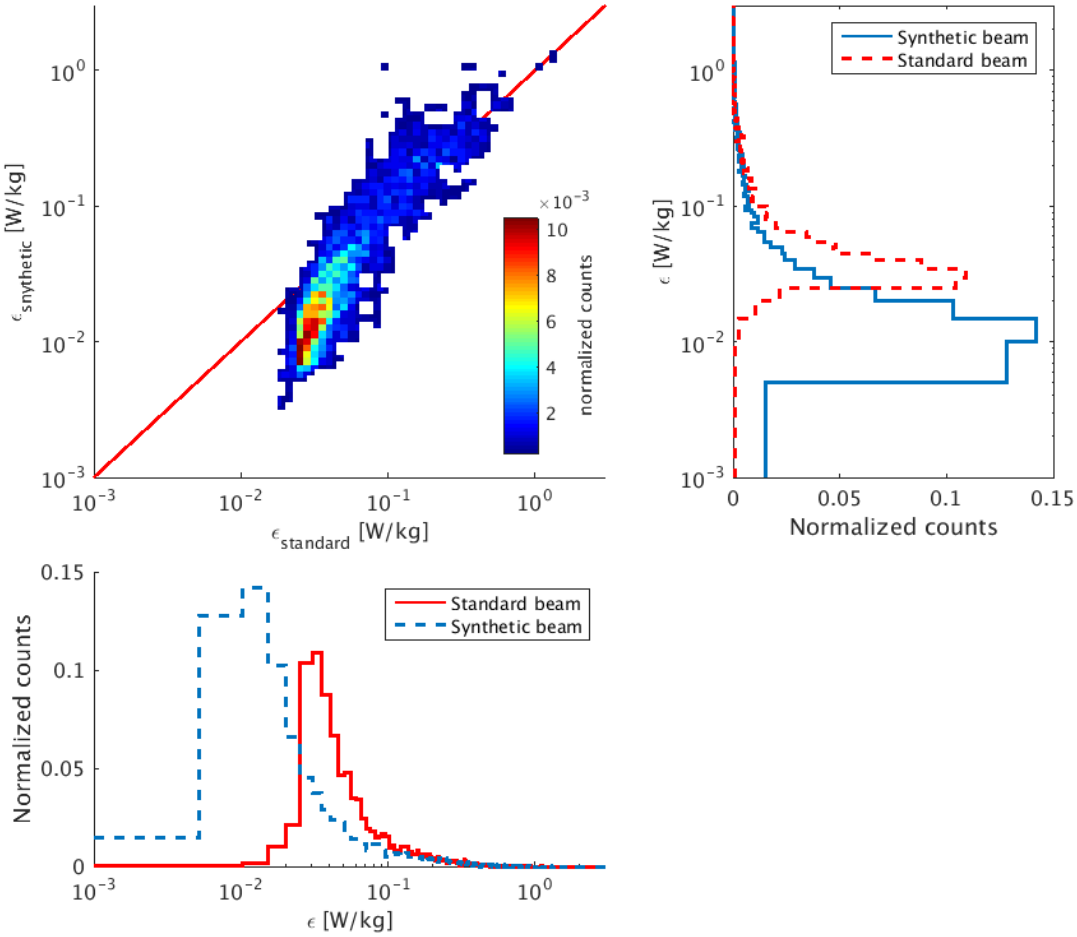

Figure 9. Histogram for the energy dissipation rate for ϵ derived by the narrow beam and the synthetic narrow beam. Top left: 2D correlation in ϵ between the standard narrow beam and the synthetic narrow beam. The red line indicates $x = y$. A deviation can be seen especially for small ϵ. The cumulative histograms along x- and y- direction are shown in the top right and lower panels, respectively. The red line shows the cumulative histogram for the standard narrow beam and the blue line for the synthetic narrow beam.

Acknowledgements

First, I would like to thank my Advisor, Prof. Jorge L. Chau, for supervising my thesis. His advice, explanations and ideas helped my a lot for my thesis. Furthermore, my thanks go to Prof. Franz-Josef Lübken, for funding my research through ILWAO. I would also like to thank Prof. Markus Rapp, Institut für Physik der Atmosphäre, DLR, for raising my interest in atmospheric physics and radar applications.
Dr. Gunter Stober was a great help during my time at IAP. Especially, he provided his truncated Gauss fitting algorithm for the imaging spectral width analysis and also an astronomical library for radar phase calibration. Dr. Toralf Renkwitz provided the phasing of the wide beam experiment. I also thank Dr. Ralph Latteck and Dr. Irina Strelnikova for their advice regarding radar techniques, atmospheric physics, and other radar related topics. I especially thank Dr. Vivien Matthias for her explanations regarding waves in the atmosphere and a whole lot of other stuff.
Furthermore, I like to thank Carsten Schult for his explanations and help regarding, but not limited to, meteors and interferometry. I like also to mention Heiner Asmus, Sven Wilhelm and Helen Schneider for discussions on several topics related (or not...) to this thesis.
Last but not least, I appreciate the help of the technical staff of the radar department at IAP, namely Thomas Barth, Jens Wedrich, Jörg Trautner and Marius Zecha. Without their work, MAARSY would not exist and this thesis would not have been possible.

Curriculum Vitae

Publication list

Peer reviewed publications

- Sommer, S., and J. L. Chau, Patches of polar mesospheric summer echoes characterized from radar imaging observations with MAARSY, *Ann. Geophys.*, *34*, 1231–1241, doi:10.5194/angeo-34-1231-2016, 2016.

- Sommer, S., J. L. Chau, and C. Schult, On high time-range resolution observations of PMSE: statistical characteristics, *J. Geophys. Res.*, *121*, 6713–6722, doi:10.1002/2015JD024531, 2016.

- Sommer, S., G. Stober, and J. L. Chau, On the angular dependence and scattering model of Polar Mesospheric Summer Echoes at VHF, *J. Geophys. Res.*, *121*, 278–288, doi:10.1002/2015JD023518, 2016.

- Sommer, S., G. Stober, and J. L. Chau, Geometric considerations of polar mesospheric summer echoes in tilted beams using coherent radar imaging, *Adv. Radio Sci.*, *12*, 197–203, doi:10.5194/ars-12-197-2014, 2014.

- Sommer, S., G. Stober, C. Schult, M. Zecha, and R. Latteck, Investigation of horizontal structures at mesospheric altitudes using coherent radar imaging, *Adv. Radio Sci.*, *11*, 319–325, doi:10.5194/ars-11-319-2013, 2013.

- Stober, G., S. Sommer, C. Schult, and R. Latteck, Observation of Kelvin-Helmholtz instabilities and short period gravity waves above Andenes in northern norway, *J. Geophys. Res.*, submitted, 2016.

- Stober, G., S. Sommer, M. Rapp, and R. Latteck, Investigation of gravity waves using horizontally resolved radial velocity measurements, *Atmos. Meas. Tech.*, *6*, 2893–2905, doi:10.5194/amt-6-2893-2013, 2013.

Non-peer reviewed publications

- Sommer, S., J. Chau, and G. Stober, Wind and spectral width estimations in PMSE with coherent radar imaging, in *General Assembly and Scientific Symposium (URSI GASS), 2014 XXXIth URSI*, doi:10.1109/URSIGASS.2014.6929775, 2014.

Erklärung über den Eigenanteil an den Manuskripten

Die in dieser kumulativen Dissertation zusammengefassten Veröffentlichungen *Sommer et al.* (2014a, 2016a, 2016b) sowie das bislang unveröffentliche Manuskript *Sommer and Chau* (2016) wurden von Frau Sommer verfasst. Die Co-Autoren haben bei der Ideengebung sowie bei der anschließenden Überarbeitung der Paper mitgewirkt. Die Graphiken hat Frau Sommer selbst erstellt und auch die zugrundeliegenden Daten bis auf wenige Ausnahmen selbst verarbeitet.

In *Sommer et al.* (2014a) hat Frau Sommer die Auswirkungen von PMSE-Messungen mit geschwenkten Strahlen systematisch untersucht. Die Idee für dieses Paper stammt von Frau Sommer, sowie die Datenanalyse, Texte und Graphiken. Die Co-Autoren haben bei der Experiment-Erstellung und -Umsetzung sowie bei der der Diskussion und Überarbeitung des Manuskriptes mitgewirkt.

Das Manuskript *Sommer et al.* (2016a) basiert auf einer Idee von Frau Sommer die Aspektsensitivität von PMSE mittles multiplen Strahlen zu untersuchen und dabei Einflüsse der Messmethode, die bis dahin nicht berücksichtigt wurden, mit zu betrachten. Gunter Stober hat zur Diskussion der Ergebnisse beigetragen. Jorge Chau hat die Korrelations-Analyse zur Untersuchung vorgeschlagen, die von Frau Sommer eigenständig umgesetzt wurde. Die Analysen, Graphiken, Texte und insbesondere die Schlussfolgerung aus den Daten, dass PMSE kleinskalige Strukturen aufweisen und dass diese bei verschiedenen Messmethoden berücksichtigt werden müssen, stammen von Frau Sommer.

In *Sommer et al.* (2016b) wurden PMSE auf sehr kurzen Zeitskalen statistisch untersucht und erfolgreich simuliert. Die Simulation auf statistischer Basis wurde von Jorge Chau vorgeschlagen und von Frau Sommer umgesetzt und erweitert. Die erste Entdeckung der statistischen Eigenschaften erfolgte von Carsten Schult im Rahmen von Meteor-Beobachtungen. Frau Sommer hat außerdem weitere Messungen vorgenommen, die Radardaten ausgewertet und geophysikalisch interpretiert. Damit stammen Datenanalyse, Simulation, Text und Graphiken in dem Paper von Frau Sommer.

In dem eingereichten Manuskript *Sommer and Chau* (2016) wurde die Annahme von kleinen Strukturen, wie in *Sommer et al.* (2016a) beschrieben, mittels bildgebender Verfahren überprüft, sowie Abbildungen der spektralen Breiten von PMSE und Windfeldern präsentiert. Weiterhin wurde eine Methode zur Verbesserung der Turbulenzabschätzung mittels Radar p̈asentiert. Hierbei hat Frau Sommer die Algorithmen f́ur das bildgebende Verfahren implementiert. Die Analysen des Windfelds und der spektralen Breiten aus dem bildgebenden Verfahren stammen ebenfalls von Frau Sommer. Der Co-Author Jorge Chau hat die Spektrumsanalyse sowie Ideen zu dem Paper beigetragen.

Erklärung

Hiermit versichere ich an Eides statt, die vorgelegte Arbeit selbstständig und ohne fremde Hilfe verfasst, keine außer den von mir angegebenen Hilfsmitteln und Quellen dazu verwendet und die den benutzten Werken inhaltlich und wörtlich entnommenen Stellen als solche kenntlich gemacht zu haben.
Die Arbeit wurde bisher weder im Inland noch im Ausland in gleicher oder ähnlicher Form einer anderen Prüfungsbehörde vorgelegt. Weiterhin erkläre ich, dass ich ein Verfahren zur Erlangung des Doktorgrades an keiner anderen wissenschaftlichen Einrichtung beantragt habe.

Kühlungsborn, den 27. Mai 2016

(Svenja Sommer)

,